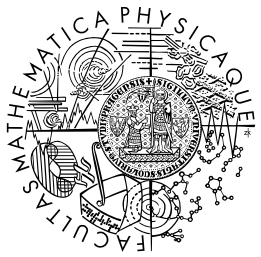

FACULTY
OF MATHEMATICS
AND PHYSICS
Charles University

BACHELOR THESIS

Jaroslav Hořák

Motions of protoplanets in an evolving gaseous disk

Astronomical Institute

Supervisor of the bachelor thesis: doc. Mgr. Miroslav Brož, Ph.D.
Study programme: Fyzika (B0533A110001)
Study branch: Obecná fyzika

Prague 2024

I declare that I carried out this bachelor thesis independently, and only with the cited sources, literature and other professional sources. It has not been used to obtain another or the same degree.

I understand that my work relates to the rights and obligations under the Act No. 121/2000 Sb., the Copyright Act, as amended, in particular the fact that the Charles University has the right to conclude a license agreement on the use of this work as a school work pursuant to Section 60 subsection 1 of the Copyright Act.

In ..... date ....

Author's signature

Dedication.

Title: Motions of protoplanets in an evolving gaseous disk

Author: Jaroslav Hořák

Institute: Astronomical Institute

Supervisor: doc. Mgr. Miroslav Brož, Ph.D., Astronomical Institute

Abstract:

Planets form from protoplanets orbiting young stars, when gaseous disk still exists. This gas gravitationally interacts with protoplanets, alongside mutual perturbations between protoplanets. This phenomenon is known as planetary migration. Our aim is to investigate the role of planetary migration, specifically, in the context of the terrestrial planets (Mercury, Venus, Earth, Mars). This has been studied previously with a stationary prescription for migration and without simulating the evolution of the disk (Brož et al. 2021). Instead, in this work we use formulae for migration torque based on actual profiles of the evolving disk. We used an N-body symplectic integrator to describe motions of protoplanets (Duncan et al. 1998). Evolution of the gas disk was modeled by 1-D hydrodynamics, considering turbulent viscosity and magnetically-driven disk wind (Suzuki et al. 2016). Migration torques were computed according to Paardekooper et al. (2011), from actual profiles of the disk. Moreover, our model included close encounters, collisions of protoplanets (merging), mutual resonances, eccentricity and inclination damping. In some simulations, we also considered the hot-trail effect (Chrenko et al. 2017), acting as eccentricity or inclination 'pumping'. Initially, we assumed a system of 28 protoplanets, with the masses in the range 0.05 to 0.1 Earth mass (i.e., a total 2 Earth masses). Simulations of a viscous disk with wind-driven mass loss were performed. For a high value of viscosity ($\alpha = 8 \cdot 10^{-5}$) and a moderate wind ($C_\mathrm{W} = 1 \cdot 10^{-5}$), dispersal of the disk is too rapid and migration has little influence on protoplanets. The collisional rate is also too low. For a low value of viscosity ($\alpha = 8 \cdot 10^{-6}$) and a weak wind ($C_\mathrm{W} = 1 \cdot 10^{-6}$), a rapid migration of protoplanets occurs, but the convergence zone is too small and high-mass planets end up close to the Sun. Eventually, an intermediate-viscosity model with strong wind shows some features of the terrestrial zone, like low-mass planets (Mercury, Mars) at the boundaries, and more massive planets (Venus, Earth) close to the centre. For this model, we computed a statistics of 25 simulations. There are two types of evolution: without late instabilities that leads to a larger number of low-mass planets, and with late instabilities, which occur after gas dispersal, leading to 4-6 planets. According to our best simulations, the hot-trail effect should excite the eccentricities of planets up to 0.07.

Keywords: protoplanetary disk, planets, migration, hydrodynamics, viscosity, disk wind

Contents

Introduction

Ancient astronomers studied stars and planets by naked eyes, hence their observations and interpretations were limited. Only relatively bright stars and planets (from Mercury up to Saturn) could be studied. Astronomers focused on relative motions of planets with respect to stars, not so on physical characteristics; even though it is in principle possible to measure angular sizes of planets, if they were observed during their setting behind distant mountains. The most important attempts to catalogize stars and explain planets were done by Hipparchus (Gysembergh et al. (2022)) and Ptolemy (see Toomer (1984)).

Today we know that the inner part of the Solar system is occupied by small low-mass planets (Mercury, Venus, Earth and Mars), whereas the outer part by large massive planets (Jupiter, Saturn, Uranus and Neptune). Jupiter and Saturn are considered *gas giants*, consisting of molecular hydrogen and in deeper layers by metallic hydrogen; the deepest part is a rocky core. On the other hand, Uranus and Neptune are *ice giants*, consisting of a rocky core, a mantle from heavier elements (water, ammonia, methane) and a thin hydrogen envelope. The internal structure of some planets was measured in detail, by means of gravitational perturbations, for example by missions Juno (Debras & Chabrier (2019), Durante et al. (2020)), or Cassini (Guillot (1999), Lainey et al. (2017)).

But what are the origins of the Solar system and all the planets? And how all of this formed? Several hypotheses concerning the origins were proposed. Immanuel Kant and then Pierre-Simon Laplace came forward with a hypothesis of formation from collapsing nebula, which flattens due to rotation (Kant (1755), Laplace (1796)). Later, Jeans introduced a model of the stability of a spherical nebula (Jeans (1902)). The modern paradigm is based on much more sophisticated models, proposing formation of filaments in a nebula (André et al. (2014)). In these filaments, many protostars surrounded by protoplanetary disks are formed (Vázquez-Semadeni et al. (2019)). Protoplanetary disks were directly observed by the ALMA system of radio-telescopes (Andrews et al. (2018)) or ESO VLT/SPHERE optical telescope (Avenhaus et al. (2018)), see, e.g., Fig. 1.

Protoplanets form by gradual aggregation of dust, followed by accretion of pebbles, assisted by aerodynamic drag (e.g., Lambrechts & Johansen (2014), Drażkowska et al. (2022)). A final stage of evolution due to mutual collisions and perturbations between protoplanets requires a detailed understanding of a gravitational interaction between protoplanets and gas. This results in migration, or changes of the semimajor axis, as well as damping or forcing of eccentricities and inclinations (Chrenko et al. (2017)). This phenomenon has been studied by means of semi-analytical theories (Tanaka et al. (2002), Paardekooper et al. (2011)), or full 1D, 2D or 3D hydrodynamical simulations (e.g., Benítez-Llambay & Masset (2016)). Migration of protoplanets plays a principal role in the build up of planetary systems (e.g., Brož et al. (2021)).

In this work, we study the origin of the inner Solar system. We compute a global evolution of a protoplanetary disk and of embedded protoplanets. influenced by migration, mutual perturbations and collisions. Our goal is to reconstruct the possible configurations and conditions, which could lead to the observed planets (Mercury, Venus, Earth, Mars).

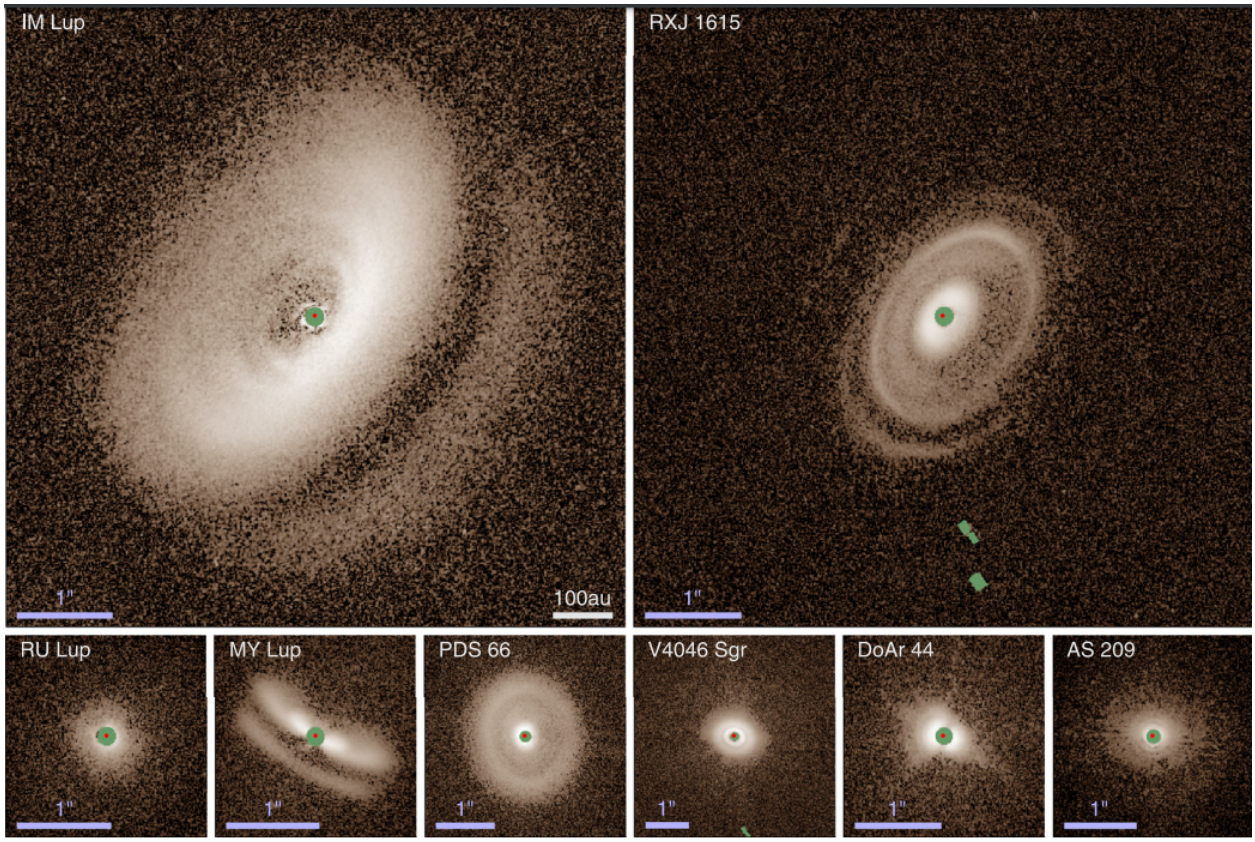

Figure 1: Images of protoplanetary disks in several early stellar systems (IM Lup, RXJ 1615, RU Lup, MY Lup, PDS 66, V4046 Sgr, DoAr 44, AS 209) observed by the ESO SPHERE/VLT telescope. These observations in the near-infrared light show primarily light of the central star reflected or scattered on dust grains. Indirectly, it corresponds to the dust density in different regions, however, except the dark places, where the central star is obscured by large amounts of dust. All images are in the same physical resolution, thus 100 au bar applies to all images. In all images, also the scale representing $1''$ on the sky is plotted. The intensity of light is in logarithmic scale. From Avenhaus et al. (2018).

1. 1-dimensional hydrodynamical models of accretion disks

In this chapter, we derive the equations of our hydrodynamical model, which will be used for modeling evolution of a protoplanetary disk. The model is based on the work of Suzuki et al. (2016), where it is discussed in more detail.

1.1 Derivation from 3-dimensional equations

The model describes the behaviour of gaseous component of the disk that can be modeled like a fluid moving in the gravitational field of the central star. Moreover, we will assume a cylindrical symmetry of the disk and also a symmetry of the vertical disk profile with respect to the mid-plane. Disks commonly contain magnetic fields and these produce a magnetically-driven disk wind, which will be also considered in the model.

In general, inviscid fluid is described by means of the **equation of continuity**

$$\frac{\partial \rho}{\partial t} + \mathbf{v} \cdot \nabla \rho = -\rho \nabla \cdot \mathbf{v}\,, \tag{1.1}$$

where $\rho(t, \mathbf{r})$ is the field of volumetric density of the fluid and $\mathbf{v}(t, \mathbf{r})$ is the velocity field, and the **equation of motion**

$$\frac{\partial \mathbf{v}}{\partial t} + (\mathbf{v} \cdot \nabla)\mathbf{v} = \underbrace{-\frac{1}{\rho}\nabla p}_{\text{pressure gradient}} \quad \underbrace{-\nabla \Phi}_{\text{gravity}} + \underbrace{\frac{1}{\rho}\frac{1}{\mu_0}(\nabla \times \mathbf{B}) \times \mathbf{B}}_{\text{Lorentz force}}\,, \tag{1.2}$$

where the first term on the right-hand side describes the acceleration due to pressure gradients, the second term the acceleration from the gravitational potential $\Phi(t, \mathbf{r})$, and the third term corresponds to the Lorentz force. We neglect the viscous term, $\frac{1}{\rho}\nabla \cdot \tau$, where $\tau = \mu\left[\nabla \mathbf{v} + (\nabla \mathbf{v})^T - \frac{2}{3}(\nabla \cdot \mathbf{v})\mathbf{I}\right]$, because the molecular viscosity μ is typically low and negligible.

The disk has a magnetic field, which is related to the fact that gas is partially ionized. We suppose that the ionized part of gas is coupled to the neutral part of gas. This can be described in the advective limit of the induction equation,

$$\frac{\partial \mathbf{B}}{\partial t} = \nabla \times (\mathbf{v} \times \mathbf{B})\,. \tag{1.3}$$

We neglect the diffusion term, $\eta \nabla^2 \mathbf{B}$, because the corresponding time scale of diffusion is typically long (Stix (2002)).

The angular momentum density $\mathbf{l} \equiv \rho \mathbf{r} \times \mathbf{v}$ is better for description, because it better corresponds to the symmetry of the problem. Moreover, if the cylindrical symmetry is assumed, then only the angular momentum coordinate perpendicular to the plane of the disk is important, because all other coordinates are zero. By combining Eqs. (1.1) and (1.2) and the Maxwell equation $\nabla \cdot \mathbf{B} = 0$, we get

$$\frac{\partial}{\partial t}(\rho r v_\phi) + \frac{1}{r}\frac{\partial}{\partial r}\left[r^2\left(\rho v_r v_\phi - \frac{1}{\mu_0}B_r B_\phi\right)\right] + \frac{\partial}{\partial \phi}\left[\rho v_\phi^2 + \frac{1}{\mu_0}B^2\right] + \frac{\partial}{\partial z}\left[r\left(\rho v_z v_\phi - \frac{1}{\mu_0}B_z B_\phi\right)\right] = 0\,, \tag{1.4}$$

where we still keep the term containing the ϕ-derivative, but this term will eventually disappear after an integration along the ϕ-axis, when reducing the problem to one dimension.

1.2 Viscosity parametrisation

According to Shakura & Sunyaev (1973), turbulence can occur in the disk, and it is a source of effective viscosity. In the ionized regions of the disk, the source of the turbulence is mainly the magneto-rotational instability (MRI; Balbus & Hawley (1991)). For including this phenomenon, we introduce perturbations of the velocity field

$$\mathbf{v}(t, \mathbf{r}) = \langle \mathbf{v}(t, \mathbf{r}) \rangle_{\Delta V(\mathbf{r})} + \delta \mathbf{v}(t, \mathbf{r})\,, \tag{1.5}$$

where $\langle\rangle_{\Delta V(\mathbf{r})}$ means the mean value through some volume ΔV, centered at $\mathbf{r}$; this term for simplicity will be written $\langle \mathbf{v} \rangle$. The second term means perturbations.

The terms in Eq. (1.4) then can be expressed as

$$\rho v_r v_\phi - \frac{1}{\mu_0}B_r B_\phi = \rho \langle v_\phi \rangle \langle v_r \rangle + \rho \langle v_\phi \rangle \delta v_r + \rho \langle v_r \rangle \delta v_\phi + \rho\left(\delta v_r \delta v_\phi - \frac{B_r B_\phi}{\mu_0 \rho}\right) \tag{1.6}$$

and

$$\rho v_z v_\phi - \frac{1}{\mu_0} B_z B_\phi = \rho\langle v_\phi\rangle\langle v_z\rangle + \rho\langle v_\phi\rangle\delta v_z + \rho\langle v_z\rangle\delta v_\phi + \rho\left(\delta v_z \delta v_\phi - \frac{B_z B_\phi}{\mu_0\rho}\right). \tag{1.7}$$

For completeness, we show the equation for the ϕ-term

$$\rho v_\phi^2 - \frac{1}{\mu_0} B^2 = \rho\langle v_\phi\rangle^2 + \rho\langle v_\phi\rangle\delta v_\phi + \rho\delta v_\phi^2 \,. \tag{1.8}$$

Now we integrate Eq. (1.4) along the ϕ-axis and along the z-axis and considering the ϕ-axis symmetry

$$\begin{aligned} r\frac{\partial}{\partial t}\int_W \rho\langle v_\phi\rangle dz + \frac{1}{r}\frac{\partial}{\partial r}\left[r^2\int_W \rho\langle v_r\rangle\langle v_\phi\rangle dz + r^2\int_W \rho\left\langle \delta v_r\delta v_\phi - \frac{B_r B_\phi}{\mu_0\rho}\right\rangle_\phi dz\right] + \\ + \left[\rho\langle v_\phi\rangle\cdot\langle v_z\rangle + \rho\left\langle \delta v_z\delta v_\phi - \frac{B_z B_\phi}{\mu_0\rho}\right\rangle_\phi\right]_W = 0\,, \end{aligned} \tag{1.9}$$

where subscript W means that the integration bounds are edges of the wind region, so integration is taken in the central opaque part of the disk. Fluctuations, which are linear disappear, because of integration and only quadratic fluctuations ie. correlations in fluctuations remain in Eq. (1.9).

We define the surface density

$$\Sigma(t,r) \equiv \int_W \rho(t,r,z)dz \tag{1.10}$$

and the parameters for the fluctuations

$$\overline{\alpha_{r\phi}} \equiv \frac{1}{\Sigma(t,r)(c_\mathrm{s}^2)_\mathrm{mid}}\int_W \rho\left\langle \delta v_r\delta v_\phi - \frac{B_r B_\phi}{\mu_0\rho}\right\rangle_\phi dz\,, \tag{1.11}$$

$$\overline{\alpha_{\phi z}} \equiv \frac{1}{(\rho c_\mathrm{s}^2)_\mathrm{mid}}\left[\rho\left\langle \delta v_z\delta v_\phi - \frac{B_z B_\phi}{\mu_0\rho}\right\rangle_\phi\right]_W, \tag{1.12}$$

where c_s is the sound speed defined for our model as the isothermal sound speed of the ideal gas

$$c_\mathrm{s} = \sqrt{\frac{k_\mathrm{B}T}{\mu m_\mathrm{H}}}\,, \tag{1.13}$$

where μ is the molecular weight of gas particles. These parameters are defined by means of the sound speed, so if we set in our model constant α's that means the fluctuations are considered proportional to $1/c_\mathrm{s}^2$. This is the idea of Shakura & Sunyaev (1973).

Then we approximate v_ϕ by the Keplerian velocity which means that the force due to radial pressure gradient is considered negligible in comparison to the gravitational force and is not essential for our purposes. Hence

$$\overline{v_\phi} \approx v_\mathrm{k} = r\Omega = \sqrt{\frac{GM_*}{r}}\,. \tag{1.14}$$

Finally, by putting definitions (1.10), (1.11), (1.12) and approximation (1.14), we get

$$r^2\Omega\frac{\partial\Sigma}{\partial t} + \frac{1}{r}\frac{\partial}{\partial r}\left[r^3\Omega\Sigma\overline{v_r} + r^2\Sigma\overline{\alpha_{r\phi}}(c_\mathrm{s}^2)_\mathrm{mid}\right] + [\rho v_z]_W r^2\Omega + (\rho c_\mathrm{s}^2)_\mathrm{mid}\overline{\alpha}_{z\phi} = 0\,. \tag{1.15}$$

1.3 Accretion rate and equation for the surface density

The accretion rate $\dot{M}(r)$, defined as inflow of mass on radius r, can be expressed in terms of $\overline{\alpha_{r\phi}}$ and $\overline{\alpha_{\phi z}}$ if we combine Eq. (1.15) with the integrated equation of continuity (expressed in terms of surface density)

$$\frac{\partial}{\partial t}(r\Sigma) + \frac{\partial\dot{M}}{\partial r} + rC_W(\rho c_\mathrm{s}^2)_\mathrm{mid} = 0\,, \tag{1.16}$$

where C_W is another parameter, which we define as

$$C_W \equiv \frac{[\rho v_z]_W}{(\rho c_\mathrm{s}^2)_\mathrm{mid}}\,, \tag{1.17}$$

which will be used for the description of the mass outflow due to the disk wind.

The accretion rate is

$$\dot{M}(r) = 2\pi r \Sigma \overline{v_r} = -\frac{4\pi}{r\Omega}\left[\frac{\partial}{\partial r}(r^2 \Sigma \overline{\alpha_{r\phi}} c_\mathrm{s}^2) + r^2 \overline{\alpha_{\phi z}} (\rho c_\mathrm{s}^2)_\mathrm{mid}\right]. \tag{1.18}$$

Using this expression, Eq. (1.15) can be further simplified by substituting for $\overline{v_r}$, thus the final dynamical equation of the model, which we will use, is

$$\frac{\partial \Sigma}{\partial t} + \frac{1}{r}\frac{\partial}{\partial r}\left\{-\frac{2}{r\Omega}\left[\frac{\partial}{\partial r}(r^2 \Sigma \overline{\alpha_{r\phi}} c_\mathrm{s}^2) + r^2 \overline{\alpha_{\phi z}} (\rho c_\mathrm{s}^2)_\mathrm{mid}\right]\right\} + (\rho v_z)_W = 0\,. \tag{1.19}$$

The behaviour of gas in presence of turbulence and advecting magnetic field can be interpreted as a viscous fluid, where the α-parameters are sources of effective viscosity. Then the disk can be understood as rotating gas in the keplerian differential rotation, with viscous shear between laminae of the fluid in ϕ and z direction and with turbulent viscosity defined as

$$\nu \equiv \frac{\overline{\alpha_{r\phi}} c_\mathrm{s}^2}{r\frac{\mathrm{d}\Omega}{\mathrm{d}r}}\,. \tag{1.20}$$

1.4 Energy balance

In our formalism, the viscosity and associated turbulence depends also on thermodynamical quantities (in particular, α parameters and the sound speed c_s depend on them). Hence our equation is not purely dynamical, and energetic considerations are necessary.

Firstly, the following **mechanical energy equation** holds in our system

$$\frac{\partial}{\partial t}\left(\frac{1}{2}\rho v^2 + \rho\Phi\right) + \nabla\cdot\left[\left(\frac{1}{2}\rho v^2 + \rho\Phi\right)\mathbf{v}\right] = -\mathbf{v}\cdot\nabla\cdot(p\delta_{ij} + \overset{\leftrightarrow}{\sigma}^{(\mathrm{M})})\,, \tag{1.21}$$

where $\overset{\leftrightarrow}{\sigma}^{(\mathrm{M})}$ is the Maxwell stress tensor. In our case of the magnetic anisotropic pressure force applied on gas, it is defined

$$\sigma_{ij}^{(\mathrm{M})} \equiv \frac{B^2}{2\mu_0}\delta_{ij} - \frac{1}{\mu_0}B_i B_j\,. \tag{1.22}$$

The second equation of the energetics is the **first law of thermodynamics**

$$\frac{\partial u}{\partial t} + \nabla\cdot(u\mathbf{v}) = -(p\delta_{ij} + \sigma_{ij}^{(\mathrm{M})})\nabla_i v_j - \nabla\cdot\mathbf{F}\,, \tag{1.23}$$

where u is the density of internal energy. On the right-hand side, we consider losses of the internal energy due to transformation to the mechanical work (through the pressure gradient) and also the energy conversion between magnetic field and matter. Finally, losses due to thermal radiation, represented by the radiative flux $\mathbf{F}$ are considered. Also irradiation from the star can be considered in this term, however, we and Suzuki et al. (2016) use another approach, incorporating this to the gas temperature calculation instead to the flux ???.

The internal energy density can be in an ideal gas system expressed in terms of the pressure as

$$u = \frac{p}{\gamma - 1}\,. \tag{1.24}$$

Lastly, the equation of the **magnetic field energy**

$$\frac{\partial}{\partial t}\left(\frac{B^2}{2\mu_0}\right) + \nabla\cdot\left[-\frac{1}{\mu_0}(\mathbf{v}\times\mathbf{B})\times\mathbf{B}\right] = \nabla_i(\sigma_{ij}^{(\mathrm{M})} v_j)\,, \tag{1.25}$$

where on the right-hand side the term corresponds to the conversion of the magnetic energy to the work and the heat.

By summing all these equations, almost all terms on the right-hand sides vanish because these represent only internal interactions within the system; only the radiation flux term remains. This leads to the final energy equation

$$\frac{\partial}{\partial t}\left(\frac{1}{2}\rho v^2 + \rho\Phi + \frac{p}{\gamma-1} + \frac{B^2}{2\mu_0}\right) + \nabla\cdot\left[\left(\frac{1}{2}\rho v^2 + \rho\Phi + \frac{\gamma p}{\gamma-1}\right)\mathbf{v} + \frac{1}{\mu_0}\mathbf{B}\times(\mathbf{v}\times\mathbf{B}) + \mathbf{F}\right] = 0\,. \tag{1.26}$$

However, this is a general form and for the purposes of our model, some approximations have to be done. Suppose that $r\Omega \gg v_r$, δv_ϕ, v_z, c_s, $B/\sqrt{\mu_0\rho}$ and allow only terms containing these quantities in the first

order to be in the equation. Fluctuations of velocity in other directions are negligible and considered of second order. Interesting fact is that gas pressure is again considered negligible, because it is of the power of two of sound speed. Similarly, pressure was considered negligible in the dynamic equation by approximating $\overline{v_\phi} \approx r\Omega$.

Again, integration over ϕ and z is done and a substitution of the time derivative from Eq. (1.19) and the average radial velocity $\overline{v_r}$ from Eq. (1.18). The final expression for energy balance is thus

$$(\rho v_z)_W \left(E_W + \frac{r^2\Omega^2}{2} \right) + F_{\rm rad} = \frac{3}{2}\Omega\Sigma\overline{\alpha_{r\phi}}c_{\rm s}^2 + r\Omega\overline{\alpha_{\phi z}}(\rho c_{\rm s}^2)_{\rm mid}\,, \tag{1.27}$$

where E_W is the energy per mass in wind region. In our case, the gravitational energy and the kinetic energy of motion in r direction are considered negligible, so $E_W \approx v_z^2/2$.

1.5 Disk wind regimes

We derived the equation representing the energetics of the disk (Eq. (1.27)), but this was not based on fundamental understanding of the processes of energy exchange. Thus, we do not know, what fraction of the energy losses is transformed to the wind and how much is transformed to the radiation. For this purpose, Suzuki et al. (2016) defined various regimes, which differ in energy distribution between the wind and the radiation.

I. No wind The simplest case for discussion is the case of a negligible wind. This practically means that $(\rho v_z)_W$, C_W and E_W are all negligible, and $\overline{\alpha_{\phi z}} \approx 0$, because there is no coupling between the midplane and the wind region. Then Eq. (1.27) becomes very simple, just

$$F_{\rm rad} = \frac{3}{2}\Omega\Sigma\overline{\alpha_{r\phi}}c_{\rm s}^2\,. \tag{1.28}$$

II. Strong wind The limit of a strong wind supposes that only the viscous heat is lost through radiation and all other energy is transformed to the wind energy. Then,

$$F_{\rm rad} = \max\left[-\frac{1}{r}\frac{\partial}{\partial r}(r^2\Sigma\overline{\alpha_{r\phi}}c_{\rm s}^2), 0 \right], \tag{1.29}$$

where the left term in the maximum represents the viscous heat losses, and the zero means that there is negligible gain from the radiation, thus the flux cannot be positive. Moreover,

$$C_{W,e} = \max\left[-\frac{1}{r^3\Omega(\rho c_{\rm s})_{\rm mid}}\frac{\partial}{\partial r}(r^2\Sigma\overline{\alpha_{r\phi}}c_{\rm s}^2) + \frac{2c_{\rm s}}{r\Omega}\overline{\alpha_{\phi z}}, 0 \right], \tag{1.30}$$

where we account for the case of a wind, not an infall of matter, thus the wind parameter $C_{W,e}$ is considered positive.

III. Weak wind In this regime, the ratio between radiative losses and energy losses due to the wind is set by the parameter $\epsilon_{\rm rad}$. Thus,

$$F_{\rm rad} = \epsilon_{\rm rad}\left[\frac{3}{2}\Omega\Sigma\overline{\alpha_{r\phi}}c_{\rm s}^2 + r\Omega\overline{\alpha_{\phi z}}(\rho c_{\rm s}^2)_{\rm mid} \right] \tag{1.31}$$

and

$$C_{W,\rm e} = (1-\epsilon_{\rm rad})\left[\frac{3\sqrt{2\pi}c_{\rm s}^2}{r^2\Omega^2}\overline{\alpha_{r\phi}} + \frac{2c_{\rm s}}{r\Omega}\overline{\alpha_{\phi z}} \right] = (1-\epsilon_{\rm rad})\left[3\sqrt{\pi/2}h^2\overline{\alpha_{r\phi}} + \sqrt{2}h\overline{\alpha_{\phi z}} \right], \tag{1.32}$$

where $\Omega\Sigma = \sqrt{2\pi}(\rho c_{\rm s}^2)_{\rm mid}$, and $h = H/r = \sqrt{2}c_{\rm s}/(r\Omega)$.

Final expression for C_W and gas density profiles Suzuki et al. (2016) also used local shearing-box simulations to find the wind parameter C_W. This led to values in the range between 10^{-5} and 10^{-4}. For C_W parameter, a minimum was used

$$C_W = \min(C_{W,0}, C_{W,\rm e}) \tag{1.33}$$

where $C_{W,0}$ is the local shearing-box result and $C_{W,\rm e}$ is an estimate based on expressions in paragraphs II and III.

Suzuki et al. (2016) performed simulations of different wind regimes (see Figs. 1.1 and 1.2). The two different values of $\overline{\alpha_{r\phi}}$ represent disks either with active MRI turbulence, or disks with suppressed turbulence, as expected in the dead zone (Mestel (1968)).

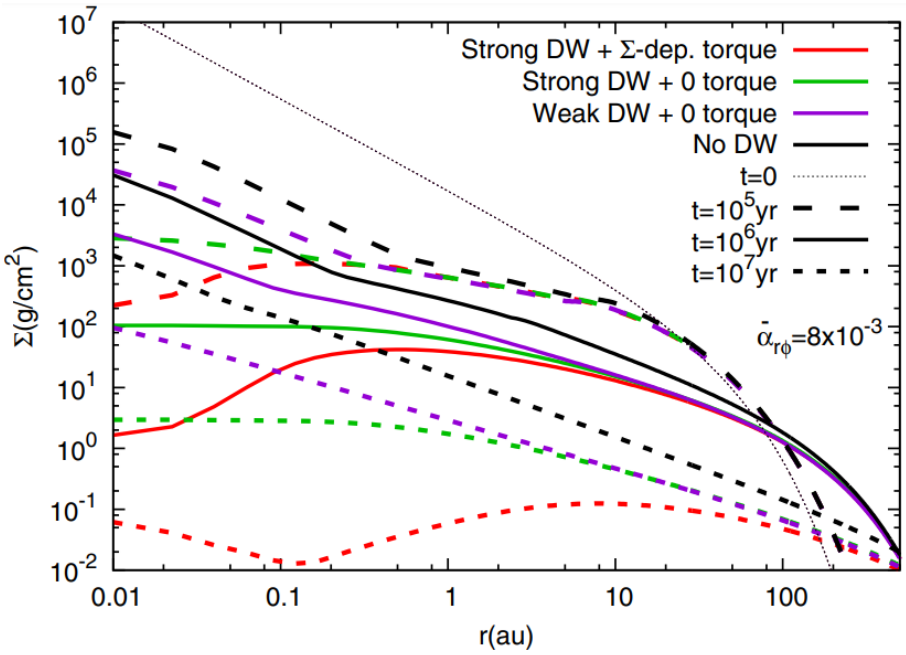

Figure 1.1: Surface density profiles for an MRI-active disk, with $\overline{\alpha_{r\phi}} = 8 \cdot 10^{-3}$. Different profiles for different modes are plotted in the graph and also their evolution (profiles at various times). The *no DW* means the regime of no wind (see paragraph I), The *strong DW* means the strong wind regime (see paragraph II) with $C_{W,0} = 2 \cdot 10^{-5}$ and with $\overline{\alpha_{\phi z}}$ either zero or Σ-dependent ($\overline{\alpha_{\phi z}} = 10^{-5} \cdot (\Sigma/\Sigma_{\rm int})^{-0.66}$, where $\Sigma_{\rm int}$ is the initial surface density). The *weak DW* means the weak wind regime (see paragraph III) with $C_{W,0} = 2 \cdot 10^{-5}$, $\overline{\alpha_{\phi z}} = 0$ and $\epsilon_{\rm rad} = 0.9$. *Figure from Suzuki et al. (2016).*

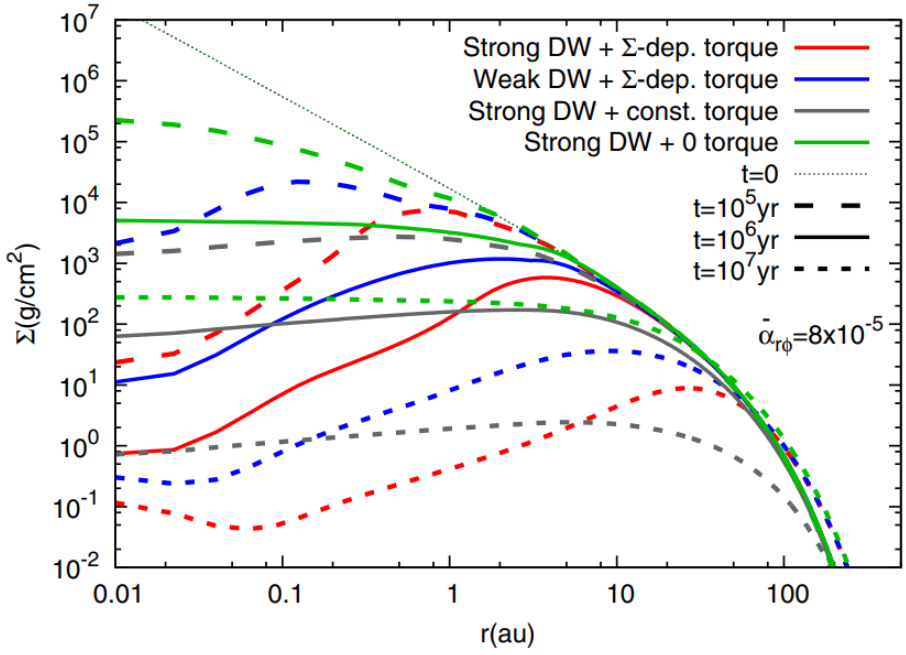

Figure 1.2: Same as Fig. 1.1, for an MRI-inactive disk, with $\overline{\alpha_{r\phi}} = 8 \cdot 10^{-5}$. For the *strong DW*, $C_{W,0} = 10^{-5}$ and $\overline{\alpha_{\phi z}}$ either zero, constant ($\overline{\alpha_{\phi z}} = 10^{-4}$), or Σ-dependent. For the *weak DW*, $C_{W,0} = 10^{-5}$ and $\overline{\alpha_{\phi z}}$ Σ-dependent. *Figure from Suzuki et al. (2016).*

2. Semi-analytical models of planetary migration

Motions of protoplanets in gaseous disks and the coupling between protoplanets and gas is not trivial. Even though full hydrodynamic simulations could provide complete comprehension of the phenomenon (see, e.g., Fig. 2.1), it is often computationally expensive. Consequently, semi-analytical approaches and approximations are often employed and verified by comparing them to the full hydrodynamic simulations. Using all these approaches, several components of the torque exerted on a protoplanet were identified: the Lindbald torque, the corotation torque, or the thermal torque. These contributions will be discussed in the following chapter.

2.1 Linear theory

2.1.1 Lindblad torque and corotation torque

Tanaka et al. (2002) attempted to solve the problem of mutual interactions of protoplanets and a disk by considering that the gravitational potential of a planetary-sized body causes relatively small density, pressure and velocity-field perturbations in the disk. The smallness of these perturbations allowed for a linearization of the Navier-Stokes equations. The potential and the perturbations were expanded onto the Fourier basis in the φ-coordinate and a Hermite basis in the z-coordinate. Then, the transformed and linearized equation was solved numerically.

The results showed that a perturbing body induces formation of spiral arms in the disk. These spiral arms carry away the angular momentum because of advective transport. The angular momentum flux through some radius is calculated as

$$F_{\mathrm{A}}(r) = \int_0^{2\pi} \mathrm{d}\theta \int_{-\infty}^{\infty} r^2 \rho_0 v_\varphi v_r \mathrm{d}z \,, \tag{2.1}$$

where ρ_0 is unperturbed density of gas, v_r represents the radial coordinate of the velocity field and v_φ the angular coordinate of the velocity filed.

The flux converges for $-\infty$ or $+\infty$ and so the angular momentum per time unit, which the gas is loosing and the planet is gaining through the spiral arms, is

$$\Gamma_{\mathrm{L}} = F_{\mathrm{A}}(r \to +\infty) - F_{\mathrm{A}}(r \to -\infty) \,, \tag{2.2}$$

which is the so-called Lindblad torque.

The flux is non-continuous at the corotation, i.e., at the radius where the planet is orbiting (assuming zero orbital eccentricity), due to deposition of the angular momentum from the planet to the co-rotation region. This can be calculated as

$$\Gamma_{\mathrm{C}} = -[F_{\mathrm{A}}(r \to +0) - F_{\mathrm{A}}(r \to -0)] \,, \tag{2.3}$$

which is the so-called linear corotation torque.

Tanaka et al. (2002) did this calculation for isothermal disks, however, for our purposes, we need an expression, which is more general. Paardekooper & Papaloizou (2008) and Paardekooper et al. (2010) derived an expression for the Lindblad and linear corotation torques for thin disks, considering only 2D calculations based on the surface density perturbations. They used a similar approach to the problem as Tanaka. Moreover, they performed 2D hydrodynamic simulations and compared them to the linear theory. The final result from Paardekooper et al. (2010) for the **Linblad torque** is

$$\gamma\Gamma_{\mathrm{L}}/\Gamma_0 = (-2.5 + 0.1\alpha - 1.7\beta)\left(\frac{0.4}{b/h}\right)^{0.71} \,, \tag{2.4}$$

where γ is the adiabatic constant, b, the softening parameter; which describes the smoothing of the gravity potential in the 2D simulation due to integration along the z-axis and modifies the potential $\Phi_{\mathrm{p}} = GM_*/\sqrt{|\mathbf{r} - \mathbf{r}_{\mathrm{p}}|^2 + b^2 r_{\mathrm{p}}^2}$.. The slope coefficients of the surface density and the temperature, α and β respectively, are defined as

$$\alpha \equiv -\frac{d\log\Sigma}{d\log r} \,, \tag{2.5}$$

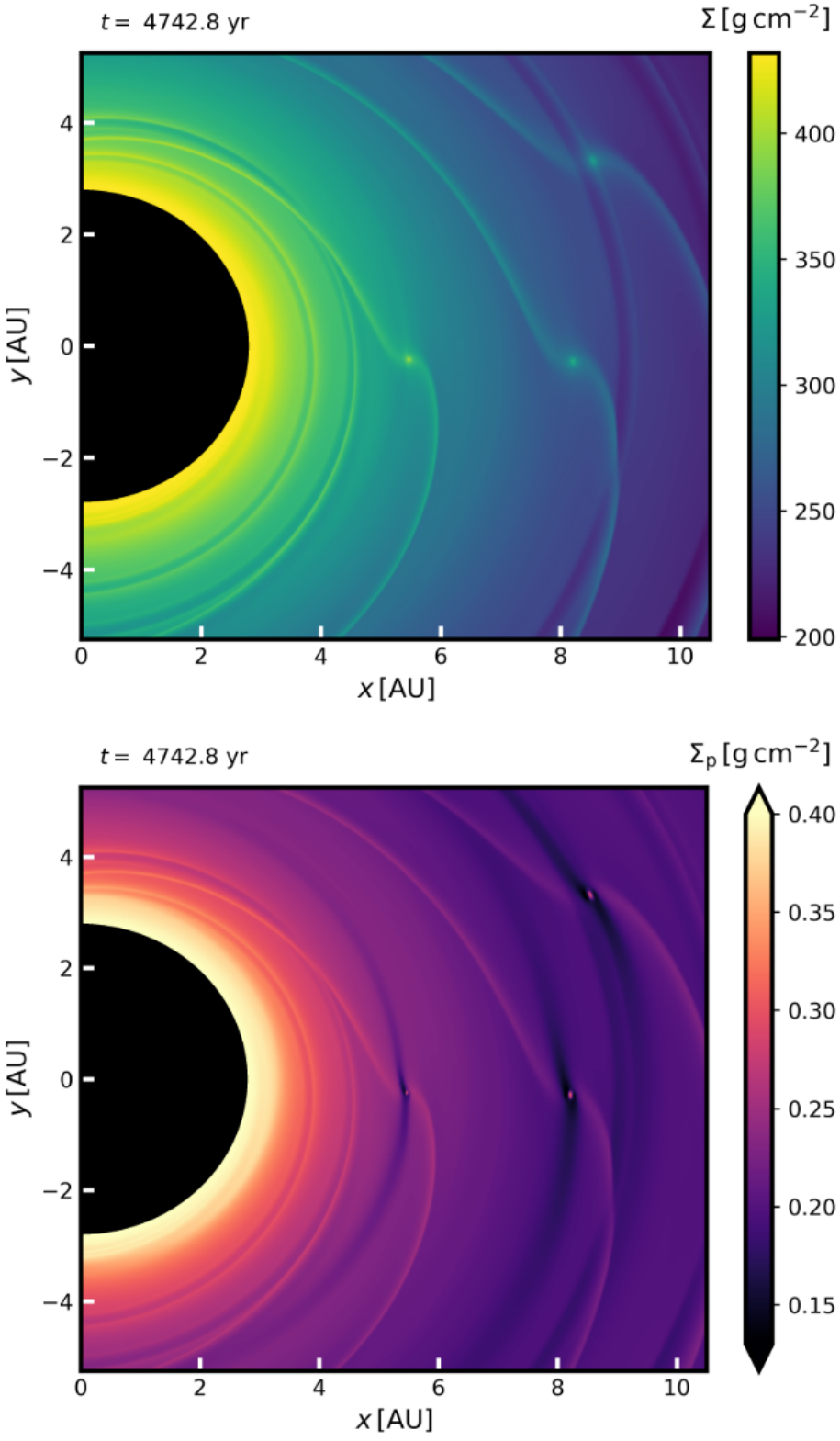

Figure 2.1: Full hydrodynamic simulation of a protoplanetary disk with embedded protoplanets by Chrenko et al. (2017). This figure shows the gas surface density (*top*) and the pebble surface density (*bottom*). Spiral arms which are causing the Lindblad torque can be seen clearly. The corotation zone can be seen barely for the two innermost protoplanets (because the respective perturbations are relatively small). The third protoplanet creates a partial gap in the gas disk, which means that this one is massive enough to accrete some gas. All the protoplanets create a gap in the pebble disk, though. *Figure from Chrenko et al. (2017).*

$$\beta \equiv -\frac{d\log T}{d\log r}\,. \tag{2.6}$$

The scaling of the torque is defined as

$$\Gamma_0 \equiv (q/h)^2 \Sigma_{\rm p} r_{\rm p}^4 \Omega_{\rm p}^2\,, \tag{2.7}$$

where $\Sigma_{\rm p}$ is the surface density at the planet's radius, $r_{\rm p}$, the planet's orbital radius, $\Omega_{\rm p}$, the gas angular velocity at the planet's radius, ,$h := H/r$, the aspect ratio, where H is the vertical scale height of the disk, $q := M_{\rm p}/M_*$, where $M_{\rm p}$ is the mass of the planet, M_*, the mass of the star.

Paardekooper et al. (2010) also calculated the **linear corotation torque** as

$$\gamma\Gamma_{\rm c,lin}/\Gamma_0 = 0.7\left(\frac{3}{2}-\alpha\right)\left(\frac{0.4}{b/h}\right)^{1.26} + 0.7\frac{2}{\gamma}\xi\left(\frac{0.4}{b/h}\right)^{1.26} + 2.2\xi\left(\frac{0.4}{b/h}\right)^{0.71}\,, \tag{2.8}$$

where the first term is the so called **barotropic torque** and it is the only non-zero component of the corotation torque in the case of barotropic gas ie., where the pressure is dependent only on the density of gas. The second term and the third term together are the so called **entropic torque**, which depends on $\xi := 3/2 + (1-2/\gamma)\alpha - 2\beta/\gamma$, i.e., the slope coefficient of the $p\Sigma^{-\gamma}$ profile, defined analogically to α and β. The entropic torque is the only linear corotation torque in the case of adiabatic disc.

2.1.2 Eccentricity damping

Tanaka & Ward (2004) subsequently studied the case of the planets with non-zero eccentricity or inclination. The non-zero eccentricity or inclination induce the radial or vertical waves, which tend to damp the eccentricity and inclination to zero. They again used the expansion onto the Fourier basis. The respective prescriptions were

$$\frac{1}{e}\left\langle\frac{{\rm d}e}{{\rm d}t}\right\rangle = \frac{A_r^{\rm s}/2 + A_\theta^{\rm s}}{t_{\rm wave}} = -\frac{0.780}{t_{\rm wave}} \tag{2.9}$$

and

$$\frac{1}{i}\left\langle\frac{{\rm d}i}{{\rm d}t}\right\rangle = \frac{A_z^{\rm c}/2}{t_{\rm wave}} = -\frac{0.544}{t_{\rm wave}}\,, \tag{2.10}$$

where $A^{\rm s}$ and $A^{\rm c}$ are respectively sine and cosine dimensionless amplitude coefficients of the force exerted on the planet due to the waves. The lower indices r, θ, z indicate the coordinates of the force. $\langle\rangle$ denotes average through one orbital period. $t_{\rm wave}$ is the characteristic time of damping,

$$t_{\rm wave} \equiv q^{-1}\left(\frac{\Sigma_{\rm p}a^2}{M_*}\right)^{-1}\left(\frac{c}{a\Omega_{\rm p}}\right)^4\Omega_{\rm p}^{-1}\,, \tag{2.11}$$

where c denotes the isothermic sound speed and a, the half-axis of the planet.

2.2 Nonlinear theory

2.2.1 Horseshoe drag

Ward (1991) studied the problem from a completely different perspective. A planet on circular orbit at radius r_p and a test particle orbiting at similar radius r were considered The question is how the presence of the planet as a perturber changes the test particle's orbit in the non-inertial frame of reference corotating with the planet. Not surprisingly, if the test particle orbits close enough to the planet, it does turn, when approaches the planet. The particle turns from an outer/inner orbit with respect to the planet to the corresponding inner/outer orbit (of the radius $2r_p - r$), respectively. Hence the particle is moving on an orbit, which looks like a horseshoe, and so it is called a **horseshoe orbit**. The condition for range of the radii, in which it occurs, is

$$|r_{\rm p} - r| \le w = \left|\frac{GM_{\rm p}}{2AB}\right|\,, \tag{2.12}$$

where $A := (r/2)d\Omega/dr$ and $B := (2r)^{-1}d(r^2\Omega)$ are the Oort constants; which are known from the galactic mechanics Oort (1940).

When the particle does turn, it exchanges its angular momentum with the planet. The angular momentum gain of the planet is

$$\Delta L = \delta m[r^2\Omega(r) - (2r_{\rm p}-r)^2\Omega(2r_{\rm p}-r)] = GM\delta m[r^{1/2} - (2r_{\rm p}-r)^{1/2}]\,, \tag{2.13}$$

where δm denotes the mass of the test particle, $\Omega(r)$, the angular velocity profile, which is considered keplerian.

Now, let us consider gas orbiting at the keplerian velocity. In the horseshoe region certain mass of gas $\Sigma(r)r\Omega(r)\mathrm{d}t\mathrm{d}r$ turns from the outer orbit to the inner orbit and also the corresponding mass of gas $\Sigma(2r_\mathrm{p}-r)\cdot(2r_\mathrm{p}-r)\cdot\Omega(2r_\mathrm{p}-r)\mathrm{d}t\mathrm{d}r$ turns on the same horseshoe orbit on the opposite side of the planet from the corresponding inner orbit to the outer orbit. Because generally exchanges of the momentum between the planet and gas are not equal on both sides according to Eq. (2.13), a torque is exerted on the planet. If the gas density radial profile is considered locally as power-law and α is defined as in Eq. (2.5) then

$$\Gamma_\mathrm{hs} = \frac{3}{4}\left(\frac{3}{2}-\alpha\right)\Sigma_\mathrm{p} w^4 \Omega_\mathrm{p}^2 \,. \tag{2.14}$$

2.2.2 Barotropic and entropic horseshoe drag

Paardekooper et al. (2010) studied the problem in a systematic way, focusing not only on the barotropic torque but also on the entropic gradient and non-conservation of the vorticity along streamlines.

Generally, the torque due to the horseshoe drag is calculated as

$$\Gamma_\mathrm{c,hs} = \int\int_R \Sigma\frac{\partial\Phi_\mathrm{p}}{\partial\varphi}r\mathrm{d}\varphi\mathrm{d}r = \left[\int \Sigma(j-j_\mathrm{p})(\Omega-\Omega_\mathrm{p})r\mathrm{d}r\right]_{\Gamma_1}^{\Gamma_2}, \tag{2.15}$$

where R means the integral over the horseshoe region, Φ_p, the gravitational potential of the planet and $j := rv_\varphi$. Paardekooper assumed symmetric horseshoe turns. Hence, a first order expansion of the quantities with respect to the planet's orbital radius leads to

$$\Gamma_\mathrm{c,hs} \approx -\frac{3}{2}r_\mathrm{p}^4\Sigma_\mathrm{p}\Omega_\mathrm{p}^2\int x^2\frac{\Sigma-\Sigma_0}{\Sigma_0}\mathrm{d}x \,, \tag{2.16}$$

where $x := (r-r_\mathrm{p})/r_\mathrm{p}$ is relative coordinate. Σ_0 is the original profile without the perturbation due to the planet, whereas Σ is the actual density profile modified by the presence of the corotation zone.

Entropy gradient Let us consider the situation of pressure equilibrium and adiabatic situation when the quantity $s \equiv p\Sigma^{-\gamma}$ is conserved along streamlines. The perturbed density can be then expressed as

$$\Sigma = \begin{cases} \Sigma_0\left(1-2\frac{\xi}{\gamma}x\right) & \text{if } 0<x<x_\mathrm{s}\,, \\ \Sigma_0 & \text{otherwise}\,, \end{cases} \tag{2.17}$$

where $x_\mathrm{s} := w/r_\mathrm{p}$ denotes the relative width of horseshoe region and $\xi := 3/2+(1-2/\gamma)\alpha-2\beta/\gamma$ is a slope coefficient of s, defined analogical to α and β, see Eq. (2.5).

Specific vorticity gradient The specific vorticity along a streamline satisfies the relation

$$\frac{\mathrm{D}}{\mathrm{D}t}\left(\frac{\omega}{\Sigma}\right) = -\frac{\nabla\Sigma\times\nabla p}{\Sigma^3} = -\frac{\nabla s\times\nabla p}{\gamma\Sigma^2 s}\,, \tag{2.18}$$

where $\frac{\mathrm{D}}{\mathrm{D}t}$ is the material derivative, representing a derivative of quantities along a streamline.

If we consider the barotropic case where $p(\Sigma)$ then the derivative is equal to 0 and the vorticity is constant along a streamline. Then perturbation of the vorticity field can be expressed simply as $\frac{\omega_0}{\Sigma_0}\left(1-2\frac{\mathrm{d}\log\omega/\Sigma}{\mathrm{d}\log r}x\right)$ if $0<x<x_\mathrm{s}$. More generally, considering also the non-barotropic case, a term corresponding to a change of the specific vorticity along a streamline has to be added,

$$\frac{\omega}{\Sigma} = \begin{cases} \frac{\omega_0}{\Sigma_0}\left(1-2\frac{\mathrm{d}\log\omega/\Sigma}{\mathrm{d}\log r}x\right)+\Delta, & \text{if } 0<x<x_\mathrm{s}\,, \\ \frac{\omega_0}{\Sigma_0} & \text{otherwise}\,. \end{cases} \tag{2.19}$$

Non-conservation of specific vorticity along the streamline Paardekooper calculated the term Δ. He considered the velocity along a streamline to be $v = \overline{v}r_\mathrm{p}\Omega_\mathrm{p}x_\mathrm{s}$, where $\overline{v}$ is a constant determined from simulations ($\overline{v}=1.0$ was determined to be in a good agreement). The respective expression is

$$\Delta(x) = \frac{2\xi}{\overline{v}\gamma}\frac{\Omega_\mathrm{p}}{\Sigma_\mathrm{p}}\left(\frac{q}{d}-\frac{3}{8}x_\mathrm{s}^2\right)\delta(x-x_\mathrm{s}) \tag{2.20}$$

where $d \equiv \sqrt{|\mathbf{r}_\mathrm{turn}-\mathbf{r}_\mathrm{p}|^2+b^2}$, $\mathbf{r}_\mathrm{turn}$ is the turning point for the horseshoe orbit, which is the largest and goes from the edges of the horseshoe region. Using numerical simulation, he then determined the horseshoe width as

$$x_\mathrm{s} = \frac{1.1}{\gamma^{1/4}}\left(\frac{0.4}{b/h}\right)\sqrt{\frac{q}{h}} \tag{2.21}$$

and $d = \sqrt{\frac{13\gamma}{4}}b$.

Finally, the entropy and vorticity perturbations are put together,

$$\frac{\Sigma - \Sigma_0}{\Sigma_0} = -2\frac{\xi}{\gamma}x + 2\left(\alpha - \frac{3}{2}\right)x - \frac{\Sigma_0}{\omega_0}\Delta\,, \tag{2.22}$$

inserted in Eq. (2.16) and integrated. Putting the result together with Eqs. (2.21), (2.20), leads to the horseshoe drag

$$\gamma\Gamma_{\rm c,hs}/\Gamma_0 = 1.1\frac{0.4}{b/h}\left(\frac{3}{2} - \alpha\right) + \frac{\xi}{\gamma}\frac{0.4}{b/h}\left(10.1\sqrt{\frac{0.4}{b/h}} - 2.2\right)\,. \tag{2.23}$$

2.2.3 Saturation

Saturation due to the viscosity If a viscous timescale $\tau_{\rm visc}$ is much longer than a libration timescale $\tau_{\rm lib}$ (i.e., a time it takes to complete a horseshoe orbit), then gas is in the same state, when it returns on the opposite side of the planet, as on the start of the libration orbit. After the turn, gas is no longer in equilibrium with the surrounding disk. Consequently, the calculations done in Sec.2.2.2 are no longer valid. It can be shown that after planet perturbs the gas and creates its horseshoe region, the torque will decrease to zero (on the timescale of $\tau_{\rm lib}$). This process is called a saturation of the horseshoe drag. So if $\tau_{\rm visc} \gg \tau_{\rm lib}$ and if the migration of the planet is slow $(\dot{a}/a)x_s \ll \tau_{\rm lib}$ then horseshoe drag can be considered as saturated all the time, except during short intervals of times, e.g., after collisions of planets when a new horseshoe region develops.

On the contrary, if the viscous timescale is much shorter than the libration timescale perturbations occur only in the region close to the planet and the rest of the horseshoe region has the same densities and the same temperatures as the overall profiles of the disk. In this case, a saturation does not occur and so Eq. (2.23) remains valid.

The most complicated is the case of $\tau_{\rm visc} \approx \tau_{\rm lib}$, when the torque remains partially unsaturated, i.e., the torque does not decrease to zero but to some $\Gamma^{'}_{\rm c,hs}$ non-zero value. In order to find it, Paardekooper firstly studied an isothermal case. He used a simple saturation model based on Masset (2001). He defined a saturation parameter

$$p_\nu = \frac{2}{3}\sqrt{\frac{r_{\rm p}^2\Omega_{\rm p}x_{\rm s}^3}{2\pi\nu_{\rm p}}} \tag{2.24}$$

and a saturation function

$$F(p) = \frac{8I_{4/3}(p)}{3pI_{1/3}(p) + \frac{9}{2}p^2I_{4/3}(p)}. \tag{2.25}$$

The p_ν parameter decribes the saturation due to the viscosity. Since an isothermal disk is also barotropic, only the barotropic term of the horseshoe drag is modified as

$$\Gamma^{'}_{\rm c,hs,baro} = F(p_\nu)\Gamma_{\rm c,hs,baro}\,. \tag{2.26}$$

Saturation due to the thermal diffusion Paardekooper then studied a general case, non-isothermal and generally non-barotropic, when also the entropic terms are involved. He realized that the entropic terms have a saturation dependent on the thermal diffusivity χ, as defined by the thermal diffusion equation,

$$\frac{\partial T}{\partial t} = -\nabla\cdot(\chi\nabla T)\,. \tag{2.27}$$

Paardekooper expressed the saturated entropic torque as

$$\Gamma^{'}_{\rm c,hs,ent} = F(p_\nu)F(p_\chi)\Gamma_{\rm c,hs,ent}\,, \tag{2.28}$$

where the saturation parameter p_χ, which was in good agreement with simulations,

$$p_\chi = \sqrt{\frac{r_{\rm p}^2\Omega_{\rm p}x_{\rm s}^3}{2\pi\chi_{\rm p}}}\,. \tag{2.29}$$

A saturation of the barotropic term is the same as in the isothermal case, i.e., as in Eq. (2.26).

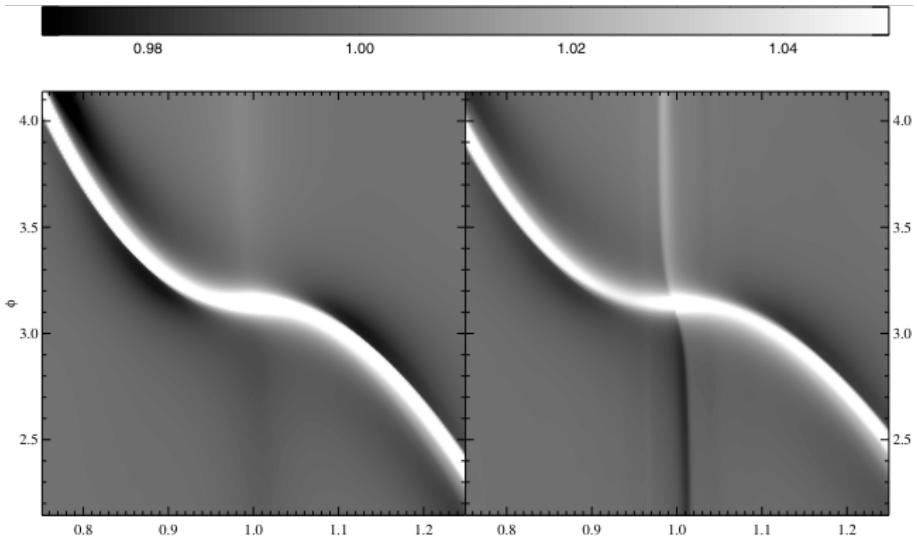

Figure 2.2: A density field (more precisely, $\rho r^{1/2}$) around a planet embedded in a gas disk. *Left*: Locally isothermal state equation of gas. *Right*: Adiabatic state equation. Spiral arms, clearly visible in this figure, are the principal cause of the Lidblad torque. In both panels, a corotation zone is also visible. In the adiabatic case, regions of perturbed density around the separatrix are more prominent though. This is caused by a transport of gas from different heliocentric distances, because of the turn. *Figure from Paardekooper & Papaloizou (2008).*

2.3 Thermal diffusivity influence on the torque

Importantly, a non-zero thermal diffusivity χ changes the expressions for all torques (Lindblad, linear corotational and horseshoe drag). These changes can be incorporated by replacing the adiabatic γ on the left-hand sides of original Eqs. (2.4), (2.8) and (2.23) by some effective $\gamma_{\rm eff}$, dependent on the thermal diffusivity.

The Lindblad torque does not strongly depend on the viscosity, but it depends strongly on the thermal diffusivity χ. Eq. (2.4) is derived supposing only small thermal diffusivity, so almost an adiabatic case. In the case of high thermal diffusivity or an isothermal case, the sound speed is different and so is the dispersion relation for waves in gas. The Lindblad torque scales with the second power of the waves' phase speed. Because of the dispersion relation in the form

$$\omega^2 = c_{\rm s}^2 k^2 \frac{1 - {\rm i}\chi k^2/\omega}{1 - {\rm i}\gamma\chi k^2/\omega}\,, \tag{2.30}$$

where $c_{\rm s}$ is the adiabatic sound speed, the Lindblad torque scales with the factor

$$\frac{v_{\rm p}^2}{c_{\rm s}^2} = \frac{2Q}{\gamma Q + \frac{1}{2}\sqrt{2\sqrt{(\gamma^2Q^2-1)^2 + (4Q-2\gamma Q)^2} + 2\gamma^2Q^2 - 2}}\,, \tag{2.31}$$

where $Q := 2\chi_{\rm p}\Omega_{\rm p}/(3hc_{\rm s}^2) = 2\chi_{\rm p}/(3\Omega_{\rm p}r_{\rm p}^2h^3)$. The effective gamma is then defined

$$\gamma_{\rm eff} := \gamma\frac{v_{\rm p}^2}{c_{\rm s}^2}\,, \tag{2.32}$$

where γ is the adiabatic constant of the gas.

The corotation torque is also induced by waves and thus the same argument holds as for the Lindblad torque.

The horseshoe drag is dependent on the width of horseshoe region instead, as seen in Eq. (2.21). This width scales with the speed sound as $c_{\rm s}^{-1/2}$ (Paardekooper & Papaloizou (2009)), so the scaling is the same as for the linear torques.

2.4 Paardekooper's formula for the Type-I migration

The linear theory holds for small perturbations, typical for a large viscosity or a large diffusivity, which smooth-out perturbations. In the opposite case, the corotation torque is described by the horseshoe drag

model. An expression, which correctly describes the transition between the two regimes, must be used.

Paardekooper et al. (2011) used full hydrodynamical simulations to determine expressions describing the transition. For the barotropic torque, he defined $K(p_\nu)$ and $G(p_\nu)$, functions of the saturation parameter p_ν, as

$$\Gamma_{\mathrm{C,baro}} = [1 - K(p_\nu)]\Gamma'_{\mathrm{C,lin,baro}} + G(p_\nu)\Gamma'_{\mathrm{C,hs,baro}} \tag{2.33}$$

and he estimated them as

$$K(p) = \begin{cases} \frac{16}{25}\left(\frac{45\pi}{28}\right)^{3/4} p^{3/2} & \text{if } p < \sqrt{\frac{28}{45\pi}}\,, \\ 1 - \frac{9}{25}\left(\frac{28}{45\pi}\right)^{4/3} p^{-8/3} & \text{if } p \geq \sqrt{\frac{28}{45\pi}}\,, \end{cases} \tag{2.34}$$

and

$$G(p) = \begin{cases} \frac{16}{25}\left(\frac{45\pi}{8}\right)^{3/4} p^{3/2} & \text{if } p < \sqrt{\frac{8}{45\pi}}\,, \\ 1 - \frac{9}{25}\left(\frac{8}{45\pi}\right)^{4/3} p^{-8/3} & \text{if } p \geq \sqrt{\frac{8}{45\pi}}\,. \end{cases} \tag{2.35}$$

For the entropic torque, he did not use another pair of functions, instead he found that a substitution

$$\Gamma_{\mathrm{C,ent}} = \sqrt{[1 - K(p_\nu)][1 - K(p_\chi)]}\,\Gamma'_{\mathrm{C,lin,ent}} + \sqrt{G(p_\nu)G(p_\chi)}\,\Gamma'_{\mathrm{C,hs,ent}} \tag{2.36}$$

led to a good agreement with simulations.

Finally, the total torque is the sum of all the torque terms

$$\Gamma = \Gamma_{\mathrm{L}} + \Gamma_{\mathrm{C,ent}} + \Gamma_{\mathrm{C,baro}}\,. \tag{2.37}$$

2.5 Eccentricity reductions

Cresswell & Nelson (2008) performed full 3D hydrodynamical simulations of gas in the gravitational field of a star and one planet in order to study the dependence of torque on the eccentricity and inclination. Considering one planet of $10\,M_{\mathrm{Earth}}$ mass and various initial eccentricities and inclinations (in the range of 0.05 to 0.3 and 0.5° to 8°), the reduction of the standard Lindblad torque is

$$\Delta_{\mathrm{L}} = \left\{ P_e + \frac{P_e}{|P_e|}\left[0.07(i/h) + 0.085(i/h)^4 - 0.08(e/h)(i/h)^2\right] \right\}^{-1}\,, \tag{2.38}$$

and

$$P_e = \frac{1 + [e/(2.25h)]^{1.2} + [e/(2.84h)]^6}{1 - [e/(2.02h)]^4}\,, \tag{2.39}$$

where h denotes the aspect ratio.

The corotation torque was studied by Fendyke & Nelson (2014), who used 2D hydrodynamical simulations of disks with various aspect ratios. Planets of 5 and $10\,M_{\mathrm{Earth}}$ were studied, with the initial eccentricities in the range $0 \leq e \leq 0.3$. It turned out that an exponential reduction of the corotation torques is in a good agreement with the simulations. The reduction, including also the inclination dependence, introduced by Coleman & Nelson (2014), is

$$\Delta_{\mathrm{C}} = \exp\left(-e/e_{\mathrm{f}}\right)[1 - \tanh\left(i/h\right)]\,, \tag{2.40}$$

where $e_{\mathrm{f}} := 0.5h + 0.01$.

Therefore, the torque after applying the reductions is

$$\Gamma = \Gamma_{\mathrm{L}}\Delta_{\mathrm{L}} + \Gamma_{\mathrm{C}}\Delta_{\mathrm{C}}\,. \tag{2.41}$$

2.6 Thermal torque

Lega et al. (2014) performed full 3D hydrodynamic simulations of a planet in a gas disk with thermal diffusion. She discovered that the effects related to thermal diffusion force a planet to migrate inwards. This is because regions of cold and dense gas in the vicinity of a planet pushing it inwards.

Subsequently, Benítez-Llambay et al. (2015) performed 3D simulations with of a disk with a hot planet. He demonstrated that the heating by a planet creates hot low-density lobes and in turn leads to a reversal of the torque.

These effects also influence eccentricities and inclinations, as demonstrated by Chrenko et al. (2017). The influence on the eccentricity is called the **hot-trail effect**.

Masset (2017) then developed a theoretical framework for all these thermal torques and using a linear theory, he derived expressions for the total thermal force.

In Cornejo et al. (2023), the expressions for the thermal force are also given, for the case when $ea \ll \lambda$ and $ia \ll \lambda$, where

$$\lambda = \sqrt{\frac{\chi}{(3/2)\Omega_{\rm p}\gamma}} \tag{2.42}$$

denotes the characteristic thermal length-scale.

The force components are expressed as

$$\begin{aligned} F_x &= eF_0(f_x^{\rm c}\cos\Omega_{\rm p}t + f_x^{\rm s}\sin\Omega_{\rm p}t)\,, \\ F_y &= eF_0(f_y^{\rm c}\cos\Omega_{\rm p}t + f_y^{\rm s}\sin\Omega_{\rm p}t)\,, \\ F_z &= eF_0(f_z^{\rm c}\cos\Omega_{\rm p}t + f_z^{\rm s}\sin\Omega_{\rm p}t)\,, \end{aligned} \tag{2.43}$$

where f-coefficients are determined from the linear theory as

$$\begin{aligned} f_x^{\rm c} &= -0.507;\ f_x^{\rm s} = +1.440\,, \\ f_y^{\rm c} &= +0.737;\ f_y^{\rm s} = +0.212\,, \\ f_z^{\rm c} &= +1.160;\ f_z^{\rm s} = +0.646\,. \end{aligned} \tag{2.44}$$

F_0 is the magnitude of the force, which is a sum of the cold component and the heating component, where the cold component accounts for torque only due to thermal diffusion, without heating from a planet. Hence,

$$F_0 = F_0^{\rm cold} + F_0^{\rm heating}\,. \tag{2.45}$$

The cold component is computed as

$$F_0^{\rm cold} = -\frac{\gamma^{\frac{3}{2}}(\gamma-1)GM_{\rm p}aL_{\rm c}\left(\frac{3}{2}\Omega_{\rm p}\right)^{\frac{1}{2}}}{2\pi c_{\rm s}^2\chi^{\frac{3}{2}}}\,, \tag{2.46}$$

where

$$L_{\rm c} = \frac{4\pi GM_{\rm p}\chi\rho_0}{\gamma}\,, \tag{2.47}$$

where ρ_0 is the mid-plane gas density at the location of the planet and let's recall that χ is the thermal diffusivity, γ, the adiabatic constant, a, the samimajor axis and $c_{\rm s}$, the adiabatic speed sound.

Finally, the heating component is

$$F_0^{\rm heating} = \frac{\gamma^{\frac{3}{2}}(\gamma-1)GM_{\rm p}aL\left(\frac{3}{2}\Omega_{\rm p}\right)^{\frac{1}{2}}}{2\pi c_{\rm s}^2\chi^{\frac{3}{2}}}\,, \tag{2.48}$$

where L denotes the luminosity of the planet. When $L = L_{\rm c}$, a reversal of the torque occurs, thus $L_{\rm c}$ is called the **critical luminosity**.

3. Implementation and validation

In this work we want to present a global model of a protoplanetary system's evolution. For this purpose, the global 1D hydrodynamic model of a gas disk, introduced by Suzuki et al. (2016) and presented in Chap. 1, has been combined with the symplectic N-body integrator for protoplanets Duncan et al. (1998). It was necessary to implement a computation of the torque, based on actual profiles of the disk, using the semi-analytical theory of migration developed by Paardekooper et al. (2011), described in Chap. 2. In the following chapter, we will present how this was done, by describing our program, developed in FORTRAN 90.

3.1 Structure of the program

3.1.1 Main cycle

The main part of the program is a cycle, coordinating the hydrodynamic simulation with the N-body simulation. (the `do while` cycle in the code). Generally, N-body simulations require much smaller time steps than hydrodynamics, because N-body have to discretise sufficiently even one orbital period of the innermost possible planet, where orbital period could be of order of days. For sufficient discretization at least 10 points per orbit are necessary (for the inner boundary of simulation set at 0.1au, it corresponds to the step length of approximately 1 day). Hydrodynamic simulation requires time scales allowing to simulate properly waves and flows in gas, which can reach the order of the soundspeed. This time step then depends on the size of a cell, but is generally orders of magnitude greater than the N-body step. Thus, the N-body cycle (the subroutine `symba_step_p1`) is performed in each iteration of the main cycle and in each step a check of the conditions for performation of the hydro's time step is done (the subroutine `kick_disk`).

Even before the main cycle, an initialization of the program has to be run. `MigrationMapInput()` allocates the 2D arrays of the migration maps and loads input parameters related to the maps. Migration maps serve as a storage of values of the Lindblad and corotation torques, for a certain range of planet's masses and semimajor axes. `OgiharaInit()` allocates fields used by the hydrodynamical simulation (the temperature, the surface density array, etc.), loads input parameters related to the disk and calls `BoundaryConditions()` and `Radiative()` subroutines (see Sec. 3.1.2). Because it is often useful to start the hydro and wait some time, until disk relaxes and developes a bit, the following subroutine `PrerunOfHydro(t_prerun)` starts hydro' and lets it run for `t_prerun`.

```
      ...
      call MigrationMapInput()
      call OgiharaInit()
      call PrerunOfHydro(t_prerun)

      do while ((t.le.tstop).and.(nbod.gt.1))

         call kick_disk(t,nbod,mass,xh,yh,zh,vxh,vyh,vzh,dthalf)

         i1st=0 ! to calculate barycentric velocities each time

         call symba7_step_pl(i1st,t,nbod,nbodm,mass,j2rp2,j4rp4,
     &        xh,yh,zh,vxh,vyh,vzh,dt,lclose,rpl,isenc,
     &        mergelst,mergecnt,iecnt,eoff,rhill,mtiny)

         call kick_disk(t,nbod,mass,xh,yh,zh,vxh,vyh,vzh,dthalf)

         t = t + dt

         ...
       enddo
       ...
       call MigrationMapsFinish()
       call OgiharaFinish()
```

Subroutine `kick_disk` The subroutine `kick_disk` is called twice, the first step uses input parameters before their actualization by SyMBA and the second uses already actualized parameters; in principle similar idea to the trapezoidal rule in numerical integration.

The first part of the `kick_disk` subroutine is the check for the hydro step. If time condition is fulfilled than `OgiharaCycle()` is called and hydro step is performed. After that `MigrationMaps()` is called, which

calculates migration maps (Gamma_L, Gamma_C) from the new updated temperature and density profiles of the disk.

The next part contains cycle through all the planets. For each planet contains the calculation of the torque and actualization of the acceleration and the velocity. In this cycle also inclination and eccentricity damping and hottrail (according to the selected regime of the hottrail in intput files) is calculated and applied on the planet.

Torques (migration maps) are calculated on discrete grid, so bi-linear interpolation for actual planet's position and mass has to be done. Coefficients of it are stored in the arrays (Gamma_L_a00, Gamma_L_a10, Gamma_L_a01, Gamma_L_a11, Gamma_C_a00, Gamma_C_a10, Gamma_C_a01, Gamma_C_a11) and potentially reused.

```
use, intrinsic :: ieee_arithmetic, only: IEEE_Value, IEEE_QUIET_NAN
use const
use parameters
use dependent, only: GridSpacing, Nrad, Rmin, Rmax
use fields
use ogihara_cycle_mod
use MMigrationMaps
use MInterpolation2D

subroutine kick disk(t, nbod, mass, xh, yh, zh, vxh, vyh, vzh, dt)
...
double precision, parameter :: MIN = 1.d-50 , MAX = 1.d50

! CHECK FOR HYDRO'

if (t.ge.time/yr) then
  call OgiharaCycle()
  call MigrationMaps()
  ...
end if

! LOOP OVER BODIES

! j .. bodies
! k .. radius-index
! l .. mass-index

do j = 2,nbod

  gm = mass(1)+mass(j)
  call orbel_xv2aei(xh(j),yh(j),zh(j),vxh(j),vyh(j),vzh(j),gm,ialpha,a,e,cos2i)

  ! SI units ...

  a = a*au
  r = sqrt(xh(j)*xh(j)+yh(j)*yh(j)+zh(j)*zh(j))*au
  m = (mass(j)*au**3/yr**2)/G

  l = int(M_p_size*(sqrt(m)-sqrt(M_p_1))/(sqrt(M_p_2)-sqrt(M_p_1)) + 1.0d0)
  if ((m.lt.M_p(l)).and.(l > 1)) l = l-1

  if (GridSpacing(1:1).eq.'S') then
    k = int(Nrad*(sqrt(r)-sqrt(Rmin))/(sqrt(Rmax)-sqrt(Rmin)) + 1.0d0)  ! square-root
    if ((r.lt.Rmed(k)).and.(k > 1)) k = k-1
  else
    k = int(Nrad*(r-Rmin)/(Rmax-Rmin) + 0.5d0) + 1  ! linear
  endif

  if (k < 1) cycle
  if (k > Nrad-1) cycle
  if (l < 1) cycle
  if (l > M_p_size-1) cycle

  ! do not compute what has been computed...
  if (Gamma_indicator(k, l).eq.0) then
    Gamma_indicator(k, l) = 1

    call BilinearInterpolation(Rmed(k), Rmed(k+1), M_p(l), M_p(l+1), &
      Gamma_L(k,l), Gamma_L(k,l+1), Gamma_L(k+1,l), Gamma_L(k+1,l+1), &
      Gamma_L_a00(k,l), Gamma_L_a10(k,l), Gamma_L_a01(k,l), Gamma_L_a11(k,l))

    call BilinearInterpolation(Rmed(k), Rmed(k+1), M_p(l), M_p(l+1), &
      Gamma_C(k,l), Gamma_C(k,l+1), Gamma_C(k+1,l), Gamma_C(k+1,l+1), &
      Gamma_C_a00(k,l), Gamma_C_a10(k,l), Gamma_C_a01(k,l), Gamma_C_a11(k,l))
```

```
65    end if
66
67    Gamma_L_value = InterpolatedValues(Gamma_L_a00(k,l), Gamma_L_a10(k,l), &
68      Gamma_L_a01(k,l), Gamma_L_a11(k,l), r, m)
69
70    Gamma_C_value = InterpolatedValues(Gamma_C_a00(k,l), Gamma_C_a10(k,l), &
71      Gamma_C_a01(k,l), Gamma_C_a11(k,l), r, m)
72
73    h = height(k)+(height(k+1)-height(k))/(Rmed(k+1)-Rmed(k))*(r-Rmed(k))
74    inc = acos(cos2i)/2d0
75    e_f = 0.5d0*h + 0.01d0
76    tmp = 1.0d0-(e/(2.02d0*h))**4
77    if (tmp.ne.0.0d0) then
78      ! Cresswel & Nelson (2008), Izidoro et al. (2017)
79      P_e = (1.0d0 + (e/(2.25d0*h))**1.2d0 + (e/(2.84d0*h))**6)/tmp)
80      Delta_L = 1.0d0/(P_e + P_e/abs(P_e)*(0.07d0*(inc/h) + 0.085d0*(inc/h)**4 - &
81        0.08d0*(e/h)*(inc/h)**2))
82    else
83      Delta_L = 0.0d0
84    endif
85
86    ! Coleman & Nelson (2014), Izidoro et al. (2017)
87    Delta_C = exp(-e/e_f)*(1.0d0 - tanh(inc/h))
88
89    Gamma_ = Gamma_L_value*Delta_L + Gamma_C_value*Delta_C
90
91    ! Tanaka & Ward (2004)
92    c_s = sqrt(k_B*Temp(k)/(molar_mass*m_u))
93    Omega_p = sqrt(G*M_s/r**3)
94
95    t_wave = ((m/M_s)**(-1) * (Sigma(k)*a**2/M_s)**(-1) * (c_s/(a*Omega_p))**4 * Omega_p**(-1)
        )
96
97    te = t_wave/0.780d0
98    ti = t_wave/0.544d0
99
100   ! au, yr, au**3/yr**2 units ...
101   a = a/au
102   r = r/au
103   te = te/yr
104   ti = ti/yr
105   Gamma_ = Gamma_/(M_s*au**2*yr**(-2))
106   Omega_p = Omega_p*yr
107   m = m/M_s
108
109   ! ACCELERATION FROM TORQUE
110
111   dadt = 2*Gamma_/(m*r)/Omega_p
112
113   v2 = vxh(j)*vxh(j)+vyh(j)*vyh(j)+vzh(j)*vzh(j)
114   if (v2.ne.0.0d0) then
115     K = 0.5d0*dadt*gm/(a*a*v2)
116   else
117     K = MAX
118   endif
119
120   axh = K*vxh(j)
121   ayh = K*vyh(j)
122   azh = K*vzh(j)
123   vxh(j) = vxh(j) + axh*dt
124   vyh(j) = vyh(j) + ayh*dt
125   vzh(j) = vzh(j) + azh*dt
126
127   ! definitions of various hot-trail regimes
128   select case (hottrail)
129    case (0)
130      continue
131    case (1)
132      if (e > hottrail_e) then
133        te = te/(1.0d0-hottrail_e/e+MIN)
134      else
135        te = MAX
136      endif
137      if (inc > hottrail_i) then
138        ti = ti/(1.0d0-hottrail_i/inc+MIN)
139      else
```

```
140         ti = MAX
141       endif
142       ...
143     end select
144
145     ! ECCENTRICITY DAMPING OR FORCING
146
147     rv = xh(j)*vxh(j)+yh(j)*vyh(j)+zh(j)*vzh(j)
148     r2 = r*r
149     K = -2.d0*rv/(r2*te)
150
151     ! updating velocity and acceleration of the planet
152     ...
153
154     ! INCLINATION DAMPING OR FORCING
155
156     kx = 0.d0
157     ky = 0.d0
158     kz = 1.d0
159     kv = vzh(j)
160     K = -2.d0*kv/ti
161
162     ! updating velocity and acceleration of the planet
163     ...
164   enddo
165   return
166   end subroutine
```

3.1.2 Hydrodynamical part

Spatial discretiazation The spatial range is determined by the following input parameters: `Rmin` – the inner boundary, `Rmax` – the outer boundary. This range is divided in `Nrad` cells and the resulting 1D spatial grid is stored in the following arrays: `Rinf` – the inner boundary of each cell, `Rsup` – the outer boundary of each cell, and `Rmed` – the center of each cell. The exact shape of grid depends on the type of spatial discretization, which can be arithmetic, logarithmic or square-root.

The arithmetic means that the spatial range is divided into cells of equal size, independently of the distance from the star, thus

$$R_{\mathrm{inf}}(\hat{r}) = R_{\mathrm{min}} + (R_{\mathrm{max}} - R_{\mathrm{min}})(\hat{r} - 1)/N_{\mathrm{rad}}\,, \tag{3.1}$$

where $R_{\mathrm{inf}}(\hat{r})$ is the lower boundary of $\hat{r}$-th cell ($\hat{r}$ is index of the array), R_{max}, R_{min} are the boundaries of simulated range and N_{rad} is the number of cells into which this range is divided.

The logarithmic discretiztion uses cells which size is proportional to the distance from the star, thus

$$R_{\mathrm{inf}}(\hat{r}) = \exp[\log R_{\mathrm{min}} + (\log R_{\mathrm{max}} - \log R_{\mathrm{min}})(\hat{r} - 1)/N_{\mathrm{rad}}]\,. \tag{3.2}$$

The square-root discretization is a 'compromise' between the two

$$R_{\mathrm{inf}}(\hat{r}) = \left[\sqrt{R_{\mathrm{min}}} + \left(\sqrt{R_{\mathrm{max}}} - \sqrt{R_{\mathrm{min}}}\right)(\hat{r} - 1)/N_{\mathrm{rad}}\right]^2\,. \tag{3.3}$$

Temporal discretization The hydro-dynamical step is controlled by adaptive time scale. This is because for properly simulating the fluid the fastest possible motion and waves propagating in gas must be computed correctly. In a subsonic fluid, it is often the speed of sound, which limits the speed of interaction in gas and the maximal speed of waves. Hence, the time step has to be less than the minimum of cell's size divided by the local sound speed. This is called the **Courant criterion**; it is impemented in the function `courant(dt_)`, which returns the length of the time step. Thus, we use the time step which is calculated as

$$\mathrm{d}t = \min(\mathrm{CFL}\,\mathrm{d}R(\hat{r})/c_{\mathrm{s}}(\hat{r}))\,, \tag{3.4}$$

where min means the minimum over all the cells, $\mathrm{d}R(\hat{r})$, the width of the $\hat{r}$-th cell and $c_{\mathrm{s}}(\hat{r})$, the sound speed in the $\hat{r}$-th cell. CFL represents the Courant number, typically a number of the order of 0.1, depending on the particular equation which is being solved. It is determined by the maximal signal speed in the problem, relative to the sound speed of the medium.

Additionally, we use the upper limit `DT` (maximal step), so if the time step from the Courant criterion is greater than the maximal step then hydro step is performed once each `DT`. This ensures some regularity in the hydrodynamical part of simulation and allows for the output of hydro's arrays at certrain multiples of

DT (the variable Ninterm then determines after how many DTs output files are printed). Also the total time span of the simulation is specified as Ntot, the number of DT segments to be done.

Eventually, we use the minimal size of the step dtmin, which prevents stopping of the simulation due to too small steps. This is case of extreme unrelaxed initial conditions and is chosen reasonably small in order to ensure fulfilment of the Courant criterion in the rest of the simulation (it is only used in order to manage these extreme cases).

Arrays for profiles of the disk Our hydrodynamical simulation operates on 1D arrays, which contain all important quantities' profiles of the disk. Each array is of size Nrad and its cells correspond to the spatial grid. Specifically, Sigma contains the surface density Σ, Temp, the temperature T, cs, the adiabatic sound speed c_s, kappa_R, the Rosseland opacity κ_R, F_rad, the radiative outflow flux F_rad (see Chap. 1 Sec. 1.5), C_w, the wind parameter C_W, alpha_phiz and alpha_rphi, the viscous parameters $\alpha_{\phi z}$ and $\alpha_{r\phi}$, and vrad, the radial velocity v_r.

These fields and the grid are allocated in soubroutines allocate_fields() and grid(), which are called from OgiharaInit().

Initial conditions Arrays are initialized in the soubroutine initial_conditions(), which is also called from OgiharaInit(). Initially, the surface density profile is set as a power law with an exponential cut-off,

$$\Sigma = \Sigma_0 [R_\mathrm{med}/\mathrm{au}]^{-\alpha_0} \exp\left(-R_\mathrm{med}/R_\mathrm{cut}\right), \tag{3.5}$$

where α_0 is the slope of the power law (often set similarly as in the minimum mass solar nebula profile). R_cut limits the extent of the disk and causes that density decreases steeply at distances greater than R_cut; in the simulation, it is specified by input parameter Rcut.

The temperature is set initially as -0.5 power of the distance,

$$T = (280\,\mathrm{K})[R_\mathrm{med}/\mathrm{au}]^{-0.5} \tag{3.6}$$

and subsequently in the subroutine OgiharaInit(), it is relaxed by the subroutine Radiative() to an equilibrium profile.

The radial velocity vrad is set to zero.

Boundary conditions To constrain gas on the inner and outer boundaries, we use the following boundary conditions.

Inner conditions – For the surface density, we set density in the innermost cell equal to the second innermost cell,

$$\Sigma(1) = \Sigma(2)\,. \tag{3.7}$$

The temperature on the boundary is set as a power law, relatively to the second innermost cell,

$$T(1) = T(2)\left[\frac{R_\mathrm{med}(1)}{R_\mathrm{med}(2)}\right]^{-0.5}. \tag{3.8}$$

Outer conditions – The surface density is set as a power law (-1.5, corresponding to the minimum mass solar nebula profile), relatively to the second innermost cell,

$$\Sigma(N_\mathrm{rad}) = \Sigma(N_\mathrm{rad}-1)\left[\frac{R_\mathrm{med}(N_\mathrm{rad})}{R_\mathrm{med}(N_\mathrm{rad}-1)}\right]^{-1.5}. \tag{3.9}$$

The temperature is again set as a power law but with a fixed coefficient,

$$T(N_{rad}) = (280\ \mathrm{K})[R_\mathrm{med}(N_\mathrm{rad})/\mathrm{au}]^{-0.5}\,. \tag{3.10}$$

Numerical methods Eq. 1.19 is solved numerically using either the FTCS scheme or the BTCS scheme, as is specified in the input file.

Let's have equation of form

$$\frac{\partial u}{\partial t} = f(\frac{\partial^2 u}{\partial r^2}, \frac{\partial u}{\partial r}, u, r, t)\,, \tag{3.11}$$

for the function $u(t, r)$. On a discrete spatial and temporal grid (let's denote $\hat{t}$ and $\hat{r}$ indices of grid) it can be solved numerically by:

1. *FTCS scheme* – $u(\hat{t}+1,\hat{r})$ is expressed in terms of $u(\hat{t},\hat{r}-1)$, $u(\hat{t},\hat{r})$ and $u(\hat{t},\hat{r}+1)$ as

$$u(\hat{t}+1,\hat{r}) = u(\hat{t},\hat{r}) + R(u(\hat{t},\hat{r}-1), u(\hat{t},\hat{r}), u(\hat{t},\hat{r}+1))\Delta t\,, \tag{3.12}$$

where $R(u(\hat{t},\hat{r}-1), u(\hat{t},\hat{r}), u(\hat{t},\hat{r}+1)))$ represents the right-hand side of the equation, where the first derivative is replaced by a difference,

$$\frac{\partial u}{\partial r}(\hat{t},\hat{r}) = \frac{u(\hat{t},\hat{r}+1) - u(\hat{t},\hat{r}-1)}{2\Delta r} \tag{3.13}$$

and the second derivative by

$$\frac{\partial^2 u}{\partial r^2}(\hat{t},\hat{r}) = \frac{u(\hat{t},\hat{r}+1) - 2u(\hat{t},\hat{r}) + u(\hat{t},\hat{r}-1)}{(\Delta r)^2}\,. \tag{3.14}$$

2. *BTCS scheme* - $u(\hat{t}+1,\hat{r})$ is expressed in terms of $u(\hat{t},\hat{r})$, $u(\hat{t}+1,\hat{r}-1)$ and $u(\hat{t}+1,\hat{r}-1)$. Thus

$$u(\hat{t}+1,\hat{r}) = u(\hat{t},\hat{r}) + R(u(\hat{t}+1,\hat{r}-1), u(\hat{t}+1,\hat{r}), u(\hat{t}+1,\hat{r}+1))\Delta t \tag{3.15}$$

and the derivatives are instead of in $\hat{t}$ expressed in $\hat{t}+1$. Then Eq. (3.15) describes $u(\hat{t}+1,\hat{r}-1)$, $u(\hat{t}+1,\hat{r})$ and $u(\hat{t}+1,\hat{r}+1)$ in terms of $u(\hat{t},\hat{r})$. This seems insufficient but the Eq. (3.15) represents a system of equations, not an isolated equation. These equations can be written concisely in matrix formalism as

$$\begin{pmatrix} b(0,\hat{t}) & c(0,\hat{t}) & & & & & & \\ a(1,\hat{t}) & b(1,\hat{t}) & c(1,\hat{t}) & & & & & \\ & a(2,\hat{t}) & b(2,\hat{t}) & c(2,\hat{t}) & & & & \\ & & \cdot & \cdot & \cdot & & & \\ & & & \cdot & \cdot & \cdot & & \\ & & & & a(n-1,\hat{t}) & b(n-1,\hat{t}) & c(n-1,\hat{t}) & \\ & & & & & a(n,\hat{t}) & b(n,\hat{t}) \end{pmatrix} \begin{pmatrix} u(0,\hat{t}) \\ \cdot \\ \cdot \\ \cdot \\ \cdot \\ \cdot \\ u(n,\hat{t}) \end{pmatrix} = \begin{pmatrix} u(0,\hat{t}-1) \\ \cdot \\ \cdot \\ \cdot \\ \cdot \\ \cdot \\ u(n,\hat{t}-1) \end{pmatrix}, \tag{3.16}$$

where a,b and c are functions depending on particular equation, which is being solved. This system is then solved by a matrix-solving algorithm.

`OgiharaCycle()` subroutine This subroutine repeatedly calls all the hydrodynamical subroutines until all hydro-steps together reach `DT`, then it returns to the `kick_disk()`.

The subroutine pointer `step_ptr(dt_)` points to a numerical scheme, either FTCS or BTCS. The suboroutine `radiative()` contains a gradient descent algorithm for solving the energetics, Eq. (1.27), and updating the temperature profile.

```
subroutine OgiharaCycle()
  ...
  use MMigrationMaps
  ...

  tout = time+DT
  ! inner cycle
  do while (time.lt.tout)
    dt_ = courant(dt_)
    dt_ = min(dt_,tout-time)
    time = time+dt_
    call step_ptr(dt_)
    call check()
    call boundary_conditions()
    call radiative()
    call boundary_conditions()
  enddo

  ...
end subroutine OgiharaCycle
```

3.1.3 Migration maps

Migration maps are 2D arrays, storing values of relevant torques dependent on the radial distance and the mass (of a planet). We use two arrays; one of them stores the Lindblad torque and the other one the corotation torque. Migration maps are actualized once per `DT` period, when torques are calculated according to the Paardekooper's formulae, see Chap. 2 Sec. 2.4.

Two modules were implemented to update the migration maps: `MMigrationMaps` and `MPaardekooper`. The first one contains a cycle, which goes through these 2D arrays and calls the function `Paardekooper` sequentially for all radial distances and masses. Moreover, it calculates α and β profiles, based on the actual profile of the disk. The power law coefficients α and β are calculated as a linear fit of logarithm of profiles, which is done within some 'window', i.e., set of cells centered on the cell, for which α and β are being calculated (cf. the subroutine `ExponentialFit(Rmed, Sigma, alpha)`). A larger window means more softening of the profile, whereas a small window can be toe sensitive to artefacts (e.g. wavy profile).

```
module MMigrationMaps
  double precision, dimension(:), allocatable :: M_p
  double precision, dimension(:,:), allocatable :: Gamma_ , Gamma_L, Gamma_C, Gamma_L_a00,
    Gamma_L_a10, Gamma_L_a01, Gamma_L_a11, Gamma_C_a00, Gamma_C_a01, Gamma_C_a10,
    Gamma_C_a11, Gamma_indicator
  integer :: no
  double precision, dimension(:), allocatable :: alpha, beta, height
  integer :: M_p_size, r_size
  double precision :: M_p_1, M_p_2
  integer :: Nmig, Nmass

  contains

  subroutine MigrationMaps()
    use const
    use parameters
    use dependent
    use fields
    use grid_mod
    use MExponentialFit
    ...

    call ExponentialFit(Rmed, Sigma, alpha)
    call ExponentialFit(Rmed, Temp, beta)

    do i = 1, Nmig
      c_s = sqrt(k_B*Temp(i)/(molar_mass*m_u))
      Omega_p = sqrt(G*M_s/Rmed(i)**3)
      height(i) = c_s/(Rmed(i)*Omega_p)
    end do

    do j = 1, size(M_p)
      do i = 1, Nmig
        Gamma_(i,j) = Paardekooper(Sigma(i), alpha(i), T(i), beta(i), nu(i), kappa(i),
    GravConst*M_p, r(i), GravConst*M_star, adiabatic_gamma, molar_mass, Gamma_L(i,j),
    Gamma_C(i,j))
      end do
    end do

  end subroutine MigrationMaps

end module MMigrationMaps
```

Module `MPaardekooper` It is responsible for a calculation of torques. It contains the function `Paardekooper`, with `Gamma_L` and `Gamma_C` beign the output parameters. Moreover, it contains `F(p)`, `K(p)` and `G(p)` functions, which are called from within the function `Paardekooper`. They are used to Eqs. (2.25), (2.34) and (2.35).

```
module MPaardekooper
  use const, GravConst => G
  use parameters

  contains

  ! Paardekooper et al. (2011)
  function F(p)
    double precision :: F
    double precision, intent(in) :: p
    double precision :: ri_4_3, ri_1_3, rk, rip, rkp

    call bessik(p, 4.0d0/3.0d0, ri_4_3, rk, rip, rkp)
    call bessik(p, 1.0d0/3.0d0, ri_1_3, rk, rip, rkp)

    F = 8.0d0/(3.0d0*p*ri_1_3/ri_4_3+9.0d0/2.0d0*p**2)
  end function F
```

```
18
19    ! Paardekooper et al. (2011)
20    function G(p)
21      double precision :: G
22      double precision, intent(in) :: p
23
24      if (p>=sqrt(8.0d0/(45.0d0*PI))) then
25        G = 1.0d0-9.0d0/25.0d0*(8.0d0/(PI*45.0d0))**(4.0d0/3.0d0)*p**(-8.0d0/3.0d0)
26      else if (p>=0.0d0) then
27        G = 16.0d0/25.0d0*(45.0d0*PI/8.0d0)**(3.0d0/4.0d0)*p**(3.0d0/2.0d0)
28      else
29        print *, "WARNING: p in function G(p) is negative."
30        G = 0.0d0
31      end if
32    end function G
33
34    ! Paardekooper et al. (2011)
35    function K(p)
36      double precision::K
37      double precision, intent(in)::p
38      if (p>=sqrt(28.0d0/(45.0d0*PI))) then
39        K = 1.0d0-9.0d0/25.0d0*(28.0d0/(PI*45.0d0))**(4.0d0/3.0d0)*p**(-8.0d0/3.0d0)
40      else if (p>=0.0d0) then
41        K = 16.0d0/25.0d0*(45.0d0*PI/28.0d0)**(3.0d0/4.0d0)*p**(3.0d0/2.0d0)
42      else
43        print *, "WARNING: p in function K(p) is negative."
44        K = 0.0d0
45      end if
46    end function K
47
48    ! Paardekooper et al. (2011)
49    function Paardekooper(Sigma, alpha, T, beta, nu, kappa, GM_p, r_p, GM_s, adiabatic_gamma,
        mu, Gamma_L, Gamma_C)
50      double precision :: Paardekooper
51      double precision, intent(in) :: Sigma, alpha, T, beta, nu, kappa, GM_p, r_p, GM_s,
        adiabatic_gamma, mu
52      double precision :: Gamma_L, Gamma_C_baro, Gamma_C_ent
53      double precision :: c_s, Omega_p, h, Q, adiabatic_gamma_eff, q_small, chi
54      double precision :: C_b_over_h, x_s, k_small, p_v, p_chi, ksi, Gamma_0
55      double precision :: Gamma_C_lin_ent, Gamma_hs_ent, Gamma_C_lin_baro
56      double precision :: Gamma_hs_baro, pomocna, Gamma_C, Gamma_, L, tau, rho
57
58      c_s = sqrt(k_B*T/(mu*m_u))
59      Omega_p = sqrt(GM_s/r_p**3)
60      h = c_s/(r_p*Omega_p)
61      chi= 16.0d0*adiabatic_gamma*(adiabatic_gamma-1.0d0)*sigma_SB*T**4/(3.0d0*kappa*Sigma**2*
        Omega_p**2)
62      Q = 2.0d0*chi*Omega_p/(3.0d0*h*c_s**2)
63      adiabatic_gamma_eff = 2.0d0*Q*adiabatic_gamma/(Q*adiabatic_gamma + 1.0d0/2.0d0*sqrt(2.0
        d0*sqrt((adiabatic_gamma**2*Q**2+1.0d0)**2 - 16.0d0*Q**2*(adiabatic_gamma-1d0)) + 2.0d0*
        adiabatic_gamma**2*Q**2-2.0d0))
64      q_small = GM_p/GM_s
65      C_b_over_h = 1.1d0*adiabatic_gamma_eff**(-1.0d0/4.0d0)*(0.4d0/b_over_h)**(1.0d0/4.0d0)
66      x_s = C_b_over_h*sqrt(q_small/h)
67      k_small= r_p**2*Omega_p/(2d0*PI*nu)
68      p_v = 2d0/3d0*sqrt(k_small*x_s**3)
69      p_chi = sqrt(r_p**2*Omega_p*x_s**3/(2d0*PI*chi))
70      ksi = beta -(adiabatic_gamma-1.0d0)*alpha
71
72      Gamma_0 = (q_small/h)**2 * Sigma * r_p**4 * Omega_p**2
73      Gamma_C_lin_ent = (2.2d0-1.4d0/adiabatic_gamma_eff)*ksi/adiabatic_gamma_eff*Gamma_0 ! Eq
        . (7)
74      Gamma_hs_ent = 7.9d0*ksi/adiabatic_gamma_eff**2*Gamma_0 ! Eq. (5)
75      Gamma_C_lin_baro = 0.7d0*(3.0d0/2.0d0-alpha)/adiabatic_gamma_eff*Gamma_0 ! Eq. (6)
76      Gamma_hs_baro = 1.1d0*(3.0d0/2.0d0-alpha)/adiabatic_gamma_eff*Gamma_0 ! Eq. (4)
77      Gamma_C_ent = Gamma_hs_ent*F(p_v)*F(p_chi)*sqrt(G(p_v)*G(p_chi)) + Gamma_c_lin_ent*sqrt
        ((1.0d0-K(p_v))*(1.0d0-K(p_chi)))
78      Gamma_C_baro = Gamma_hs_baro*F(p_v)*G(p_v) + (1.0d0-K(p_v))*Gamma_C_lin_baro
79      Gamma_C = Gamma_C_baro + Gamma_C_ent
80      Gamma_L = (-2.5d0 - 1.7d0*beta + 0.1d0*alpha)/adiabatic_gamma_eff*Gamma_0
81      Gamma_ = Gamma_L + Gamma_C
82      Paardekooper = Gamma_
83    end function Paardekooper
84
85  end module MPaardekooper
```

3.2 Validation

Implemented models, especially the modules `MPaardekooper` and `MMigrationalMaps`, had to be validated. This was done by comparing various quantities calculated by the module `MPaardekooper` to those calculated by Paardekooper et al. (2011) and comparing their figures with ours. Moreover, `MMigrationalMaps` was validated against the migration maps of Bitsch et al. (2013).

3.2.1 Validation of `Paardekooper` function

Validation of function $F(p)$ The function $F(p)$, Eq. (2.25), was tested because it is non-trivial and contains a calculation of the Bessel functions. It was compared to manually sampled points from Paardekooper et al. (2011), Fig. (3.1). Our calculation is in excellent agreement ($\ll 1\,\%$) with the Paardekooper's.

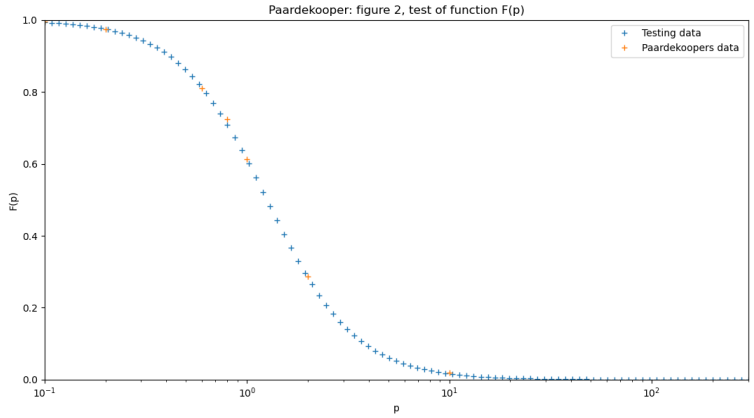

Figure 3.1: $F(p)$ function. The orange points are from Paardekooper et al. (2011) Fig. 2, the blue points are calculated by `F(p)` function of our program.

Paardekooper's fig. 3 In that figure, Paardekooper's Eq. (32) seems to be plotted according to its caption. However, if formulas for $\Gamma_{\mathrm{c,hs,baro}}$ and $\Gamma_{\mathrm{c,lin,baro}}$ are inserted into Paardekooper's Eq. (32) and compared with Paardekooper's Fig. 3 we can see that the factor $(1.5-\alpha)/\gamma$ would have to be equal approximately 2, but this is impossible for $\alpha = 0.5$, $\beta = 1.0$ as claimed by Paardekooper; to get that curve $\gamma < 1$ would be required. For this reason, it's difficult to determine, which parameters or which equation Paardekooper really plotted in his figure. In Fig. 3.2, one can see our curve, calculated with Paardekooper's parameters, compared with the Paardekooper's. The position of the maximum of our curve is order of 10s % to the right in comparison with the Paardekooper's maximum. We conclude that Paardekooper probably made an error in his parameters, plotted something different than Eq. (32) or simply did not declare all necessary parameters.

Paardekooper's fig. 5 This validation validates mainly $G(p)$ and $K(p)$ functions, Eqs. (2.35) and (2.34), and the expressions for torques, Eqs. (2.33), (2.36), (2.26) and (2.28). It is based on a calculation of the corotation torque dependence on p_ν, based on the assumption that $\chi_{\mathrm{p}} = \nu_{\mathrm{p}}$, with the same parameters as did Paardekooper and comparison with the dashed curve in his Fig. 5. As can be seen in Fig. (3.3) the both curves are equal within $\ll 1\,\%$, thus this validation can be considered as successful.

Paardekooper's fig. 6 This is another test for $K(p)$, $G(p)$ functions and the torque expressions. A little bit different regime was chosen, now ν_{p} and χ_{p} are independent and the torque dependency on ν_{p} is calculated for different constant values of χ_{p}. This is then compared to Paardekooper's fig. 6, see our Fig. 3.4. There is a small error but it is only of the order of percents.

Paardekooper's fig. 8 In this test, the expression for γ_{eff}, Eq. (2.32) together with Eq. (2.31), was tested. Now χ is varied and γ_{eff} dependence is calculated. It was done for $h = 0.025$, 0.05 and 0.1 as did Paardekooper, and then compared with his fig. 8, see our Fig. 3.5. Paardekooper's result are in accordance with our results within the order of percents JH:.....lepsi obrazek.

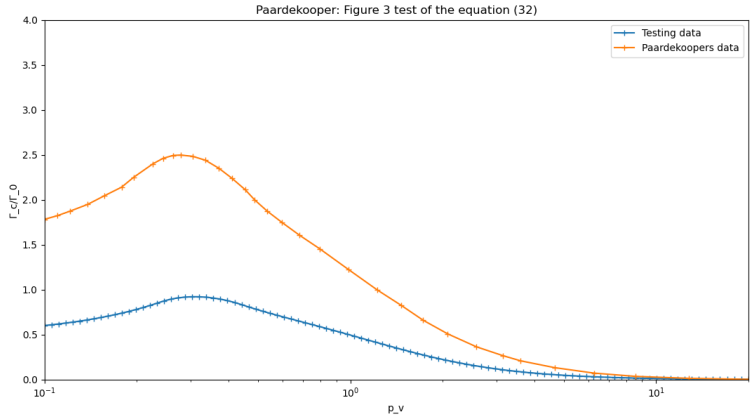

Figure 3.2: Comparison of fig. 3 from Paardekooper et al. (2011) (*orange*) with our calculation of the corotation torque $\Gamma_{\mathrm{C,baro}}/\Gamma_0$ (*blue*), Eq. (2.33). In this test, we assumed $\gamma = 1.4$ and γ_{eff} was not used at all. Other parameters were $\alpha = 0.5$, $\beta = 1.0$, $h = 0.05$, $M_{\mathrm{p}}/M_{\mathrm{s}} = 1.26 \cdot 10^{-5}$ and $b/h = 0.4$.

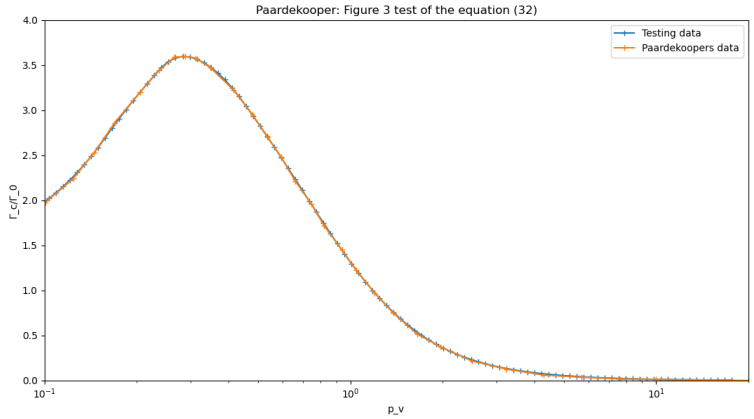

Figure 3.3: Comparison of fig. 5 from Paardekooper et al. (2011) (*orange*) with our calculation of $\Gamma_{\mathrm{C}}/\Gamma_0$ (*blue*), where $\Gamma_{\mathrm{C}} = \Gamma_{\mathrm{C,baro}} + \Gamma_{\mathrm{C,ent}}$, Eqs. (2.33), (2.36). In this test, we assumed $\nu_{\mathrm{p}} = \chi_{\mathrm{p}}$ and $\alpha = 0.5$, $\beta = 1.0$, $h = 0.05$, $\gamma_{\mathrm{eff}} \approx \gamma = 1.4$, $M_{\mathrm{p}}/M_{\mathrm{s}} = 1.26 \cdot 10^{-5}$ and $b/h = 0.4$.

Validation of γ_{eff} in the limit Eq. (2.32) together with Eq. (2.31) is a monotonous function with the limits $\gamma_{\mathrm{eff}} \to \gamma$ for $Q \to +0$ and $\gamma_{\mathrm{eff}} \to 1$ for $Q \to +\infty$. On a computer, because of limited precision of the respective data types, the calculation is not sufficiently precise for $Q < 10^{-7}$, when γ_{eff} instead of being equal to γ, goes to 2. Thus, we had to test if Q can really be lower than 10^{-7}. We performed one simulation, printing the values of Q and γ_{eff}. If Q was of the order 10^{-7} this did not led to an important error in γ_{eff}; it was only slightly above γ. If Q is of the order 10^{-8}, γ_{eff} was indeed computed erroneously as 2. We decided to introduce an `if` condition for a possible error.

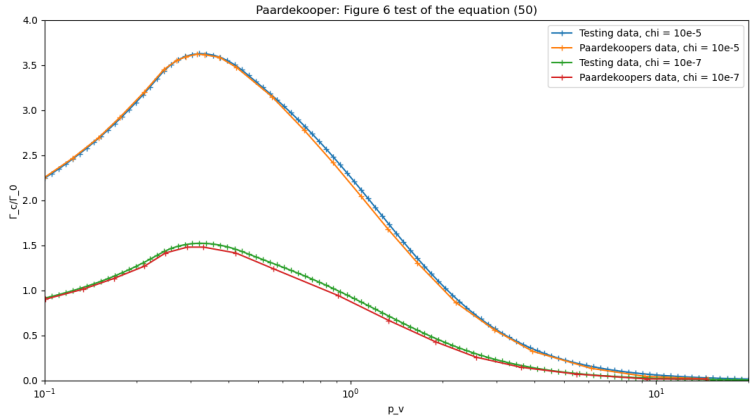

Figure 3.4: Comparison of fig. 6 from Paardekooper et al. (2011) with our calculation of Γ_C/Γ_0. The parameter ν_p was varied and test was done for two different values of χ_p ($10^{-7}\,au^2\,yr^{-1}$ and $10^{-5}\,au^2\,yr^{-1}$).

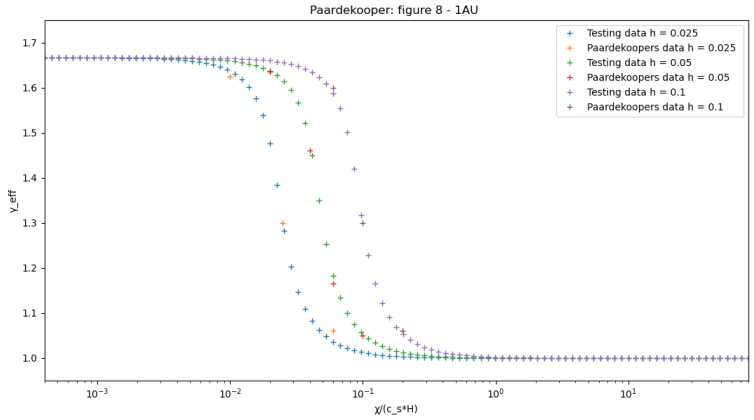

Figure 3.5: Comparision of fig. 8 from Paardekooper et al. (2011) with our calculation of γ_{eff} dependency on $\chi/(c_s H)$. The parameters were $h = 0.025$, 0.05 and 0.1 (three different curves), and $\gamma = 5/3$.

3.2.2 Validation of migration maps

Our migration maps were compared with those calculated with Bertram Bitsch's program (Bitsch et al. (2013)). The test was done for the disk profiles from Bitsch et al. (2015), for the high-metallicity case. In Fig. 3.5, the comparison of both sets of maps for several times of disk evolution can be seen. Parameters were: the metallicity $\mu_{\mathrm{R}} = 0.01$, the α-viscosity $\alpha = 5.4 \cdot 10^{-3}$ and the opacity prescription was from Bell & Lin (1994).

When the precise prescription for $F(p)$ was used (Eq. (2.25)), there was a small error between both sets of maps. The error was of the order of percents for more massive planets than $\approx 0.5 M_{\mathrm{E}}$ and under the percent for masses less than that. This error disappeared ($\ll 1\,\%$) when approximate formula for $F(p)$, which was used by Bitsch, was used by us as well,

$$F(p) \approx \frac{1}{1 + (p/1.3)^2}\,. \tag{3.17}$$

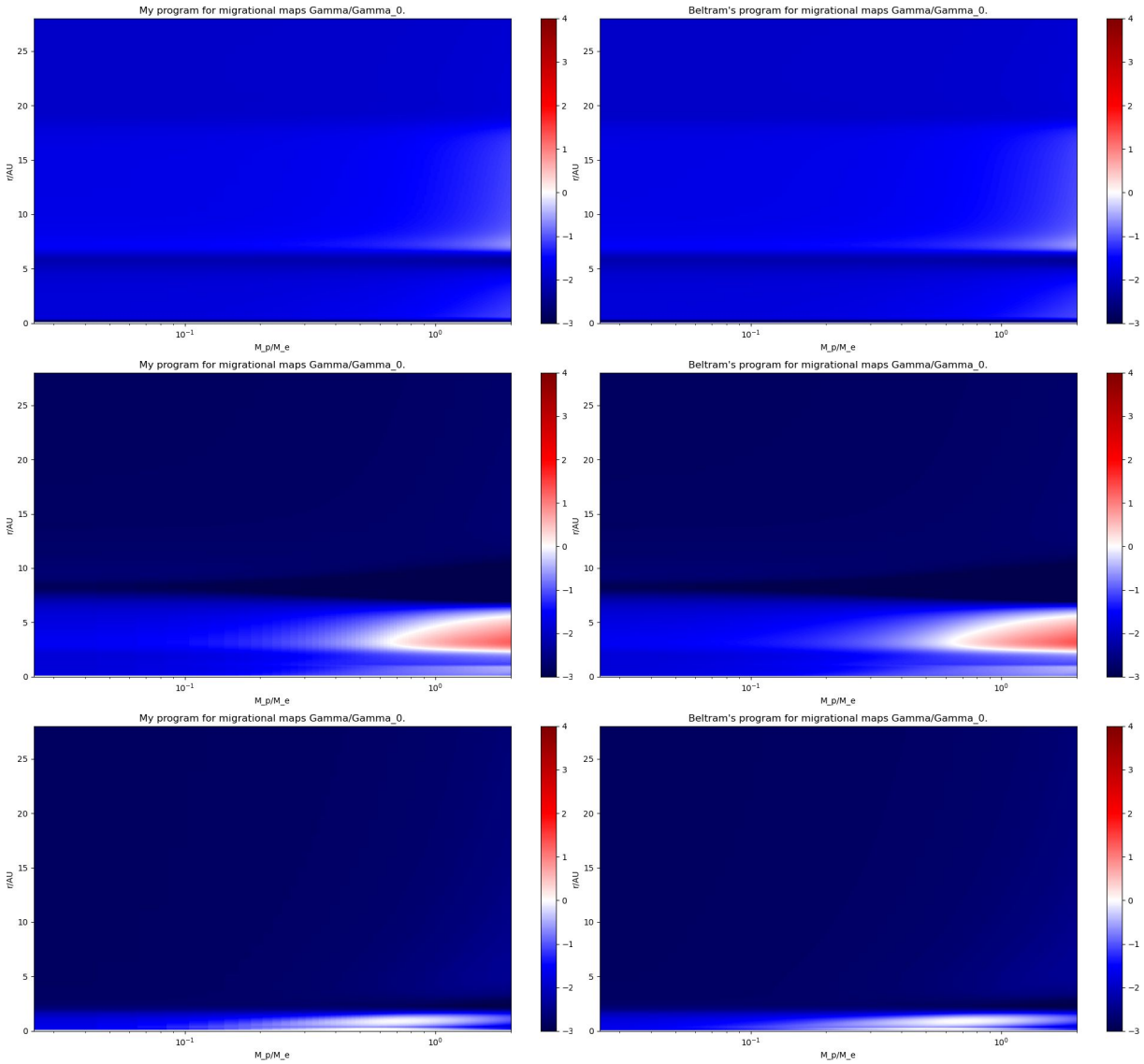

Figure 3.5: Normalized migration maps, Γ/Γ_0, for the disk profile from Bitsch et al. (2015), calculated by our program (*left*) and Bitsch's program (*right*). The corresponding times of the disk state are (from top to bottom) $t_{\mathrm{disk}} = 0.0$, 1.1 and 10.0 Myr

4. Parameter survey

In this chapter, we focus on a reconstruction of early Solar system's architecture. The question of early evolution of planetary systems has been extensively studied before and several approaches to explain different aspects were employed. For example, Izidoro et al. (2017) studied super-Earths formation from migrating protoplanets, Raymond & Izidoro (2017) a transport of water to the terrestrial zone by planetesimals, or Woo et al. (2024) the Solar system formation from a thin ring of planetesimals. For a detailed discussion of the topic see the recent review by Raymond (2024).

In particular, Brož et al. (2021) studied a system of Mercury- to Mars-size protoplanets pushed together by convergent migration. They described the migration torque by a *fixed* prescription. This led to a successful formation of Solar-system analogues. The model described in Chap. 3 is an extension of that work, since it can be applied to planetary systems embedded in an *evolving* disk.

In this work, we will start from some initial set of protoplanets and we will attempt to determine the range of disk parameters which lead to a formation of a system similar to the Solar system in terms of planets' masses, numbers and also their orbital characteristics. Such a system could be later on tested statistically with various initial conditions for protoplanets in order to search for the best Solar system analogues.

4.1 Initial conditions and other parameters

The most important parameters of the model, which could be varied, are: the set of initial protoplanets (its distribution and extent), the initial conditions and other parameters of the disk. For the moment, we will use a fixed set of Mercury- to Mars-size protoplanets; possible dependence on it is not studied here. Nevertheless, we will examine the role of other parameters.

The hydrodynamical model introduced by Suzuki et al. (2016) and described in Chap. 1 has several free parameters like $\overline{\alpha_{r\phi}}$, $\overline{\alpha_{\phi z}}$ and C_W, or even the initial density profile, which determines the total amount of gas in the disk. These parameters determine the overall evolution of the disk (the surface density profile, temperature profile) and its lifetime and thus determine the migration rates. This has a major impact on planetary systems' formation.

We essumed a star of one Solar mass and a set of 28 protoplanets of Mercury to Mars' mass (in total $2\,M_\mathrm{E}$ – approximately current mass of the inner Solar system). The mass with increasing number j of a protoplanet (i.e., the greater distance from the star) is

$$m(j+1) = 1.026\,m(j)\,. \tag{4.1}$$

We distributed them from 0.4 to 1.8 au, where neighbouring protoplanets are separated by a fixed multiple of the mutual Hill sphere's radius,

$$\frac{a(j+1)-a(j)}{[a(j+1)+a(j)]/2} = 9.75\left(\frac{m(j+1)+m(j)}{3M_\mathrm{s}}\right)^{1/3}, \tag{4.2}$$

where M_s is the mass of the central star (in our case, one Solar mass).

Eccentricities were set to be equal 0.01 and inclinations 0.5°. The longitude of the ascending node, the argument of perihelion and the mean anomaly were for each planet chosen randomly.

The planets were inserted in the disk at 0.3 Myr in order to avoid problems with non-equilibrium initial state of the disk (0.3 Myr is enough time for the 'hydro' to relax).

For the disk, we set a fixed initial profile according to Eq. (3.5), with the surface density $\Sigma_0 = 1700\,\mathrm{g\,cm^{-2}}$ at 1 au, the power-law exponent of -1.5 and the exponential cutoff at 30 au. This is inspired by the Minimal Mass Solar Nebula (Hayashi (1981)).

The spatial discretzation had to be tested in order to find a suitable number of radial cells for which migration maps converge. We found that $N_\mathrm{rad} = 1024$ is sufficient. Other parameters of the 'hydro' and technical details of the discretization are summed up in Tab. 4.1.

Two types of models, weak-wind and strong-wind were tested, where each of them assumed different radiative energy and wind prescriptions (Eqs. (1.31), (1.32) and (1.29), (1.30), respectively). These models and concrete values of parameters $\overline{\alpha_{r\phi}}$, $\overline{\alpha_{\phi z}}$ and C_W were examined and varied in order to find the best combination.

Table 4.1: Parameters of the MRI-inactive, weak-wind model with a Σ-dependent torque (Suzuki et al. (2016)). Σ_0 is the initial surface density of gas at 1 au, α_Σ and R_{cut} describe the dependence of the initial surface density on the distance from the star (Eq. (3.5)), $\overline{\alpha_{r\phi}}$, the turbulent viscosity, $\overline{\alpha_{\phi z}}$, the wind-related alpha, C_{W}, the intensity of the disk wind. The radiative equation describes what type of equation was considered. The opacity describes which opacity prescription was used. The discretization was determined by N_{rad}, the number of cells, r_{min} and r_{max}, the distance of the inner and outer boundary, DT, the default (long) time step, $\mathrm{d}t_{\mathrm{min}}$, the minimum time step, CFL, the Courant number,.

Our parameters of the hydrodynamical model	
parameter	value
Σ_0	$17000\,\mathrm{kgm}^{-2}$
α_Σ	-1.5
R_{cut}	30 au
$\overline{\alpha_{r\phi}}$	**varied**
$\overline{\alpha_{\phi z}}$	**varied**
C_W	**varied**
radiative equation	**varied** according to regime (strong vs. weak wind)
opacity	Zhu et al. (2012)
N_{rad}	1024
r_{min}	0.05 au
r_{max}	100 au
grid spacing	square-root
DT	1000 yr
$\mathrm{d}t_{\mathrm{min}}$	1 yr
CFL	1
solving method	BTCS

4.2 MRI inactive weak wind high viscosity model ($\overline{\alpha_{r\phi}} = 8 \cdot 10^{-5}$, $\overline{\alpha_{\phi z}} = 10^{-5}(\Sigma/\Sigma_0)^{-0.66}$, $C_{\mathrm{W}} = 10^{-5}$)

We started with the MRI inactive weak wind model from Suzuki et al. (2016) with the same parameters, namely: $\overline{\alpha_{r\phi}} = 8 \cdot 10^{-5}$, $\overline{\alpha_{\phi z}} = 1 \cdot 10^{-5}(\Sigma/\Sigma_0)^{-0.66}$ and $C_{\mathrm{W}} = 1 \cdot 10^{-5}$.

The evolution of disk profiles is plotted in Fig. 4.1 and the corresponding migration maps in Fig. 4.2. An inverted profile of the gas surface density (increasing Σ with r) occurs in this model and leads to a negative α-slope (α in the terrestrial zone is between -0.5 and 1 at 0.3 Myr and between -1 and -0.5 after 3 Myr). The inversion mainly affects the barotropic corotation torque, which is very dependent on α and independent of β. Hence, the corotation torque is stronger (positive), and 'overpowers' the negative Lindblad torque and leads to a formation of a convergent zone. Between 0.3 and 1 Myr, the gas density maximum (i.e., the inversion) occurs around 1 au and later shifts with time to greater radii (after 3 Myr, it is at more than 2 au).

The temperature profile is monotonous and β is between 0.3 and 0.8. After 3 Myr, it is almost a power law and β is a constant around 0.5. The Lindblad torque and entropic corotation torque are more sensitive to β than to α and they both decrease with increasing β.

The nontrivial shape of the convergent zone (e.g., two separated zones at 0.3 Myr) is mainly caused by opacity transitions. At 0.3 Myr, two transitions can be seen, one around 0.42 au due to graphite grains corrosion and another around 0.11 au due to other grains evaporation. At 1 Myr, the graphite corrosion region is shifted more inwards, to around 0.25 au, and the grains evaporation region is shifted so inwards that it is out of the simulation range. At later times, opacity transitions are no longer apparent.

According to the evolution of the system, the maximal migration rate was of the order of $0.1\,\mathrm{au\,Myr}^{-1}$. This is not sufficient because migration ceased with time. According to the migration maps, in the terrestrial zone after 10 Myr, the migration rates in the absolute value are lower than $10^{-3}\,\mathrm{au\,Myr}^{-1}$. At that time, the gas surface density is less than $20\,\mathrm{kg\,m}^{-2}$. The inner part of the disk is almost dispersed and, according to the migration rates of planets (Fig. 4.3), no significant migration is apparent after 3 Myr.

The system ended up with a high number of low-mass planets (14 planets with the maximal mass of $0.24\,M_{\mathrm{E}}$) and no high-mass planets like Venus or Earth were present. The rate of collisions was too low and the system was difficult to destabilize (possibly due to mutual resonances). Overall, the migration was not efficient enough to concentrate the protoplanets.

One of the possible solutions could be to prolong the lifetime of the disk to make the migration more

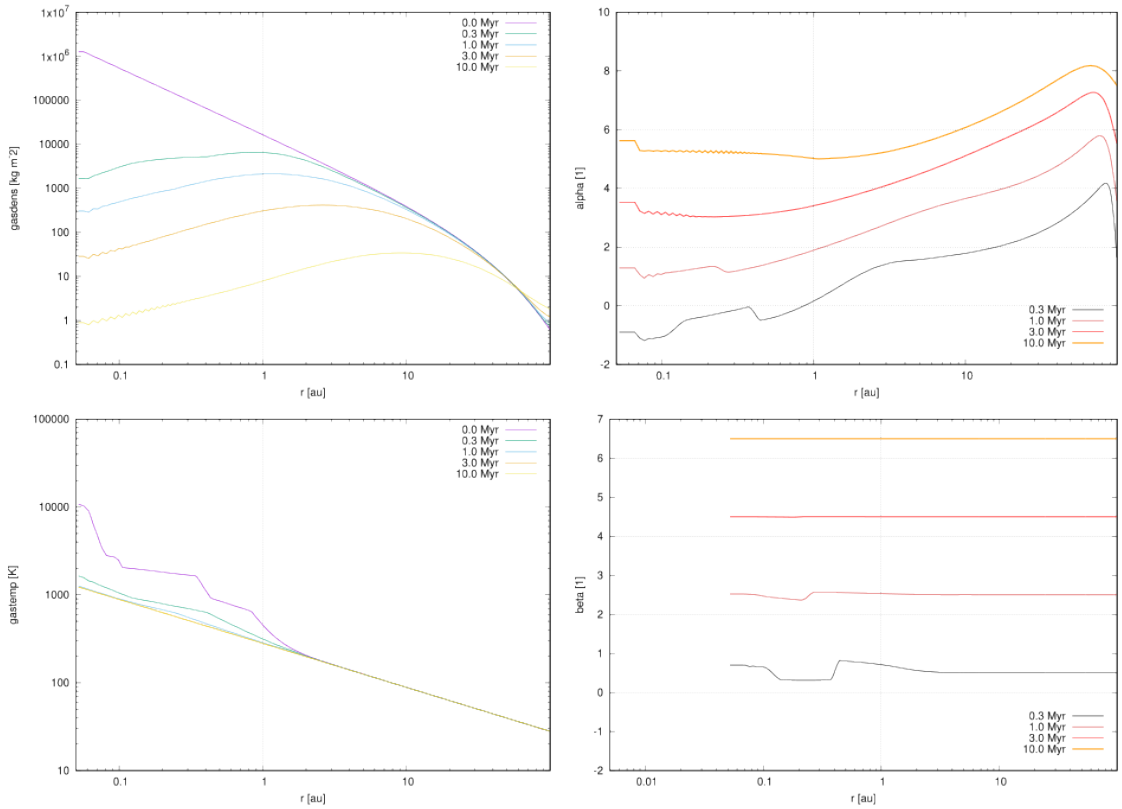

Figure 4.1: The gas surface density (*top, left*) and temperature (*bottom, left*) profiles of the MRI inactive weak wind high viscosity disk at several different times: 0.0, 0.3, 1.0, 3.0, 10.0 Myr. The right panel contains α (*top, right*) and β (*bottom, right*) slope coefficients (Eq. (2.5) and (2.6)); for clarity each time has different position of the zero (0.3, 1.0, 3.0, 10.0 Myr - 0, 2, 4, 6).

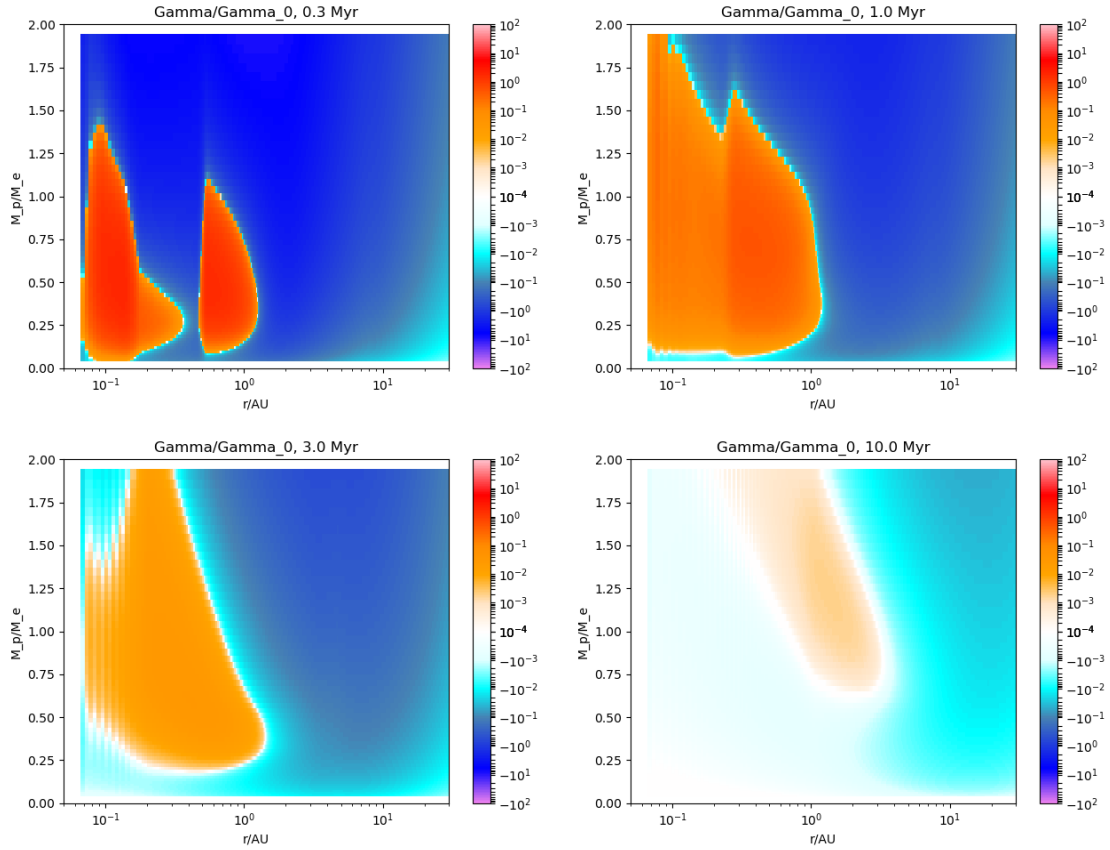

Figure 4.2: Migration maps for the MRI inactive weak wind high viscosity model for various times – 0.3 (*top, left*), 1.0 (*top, right*), 3.0 (*bottom, left*) and 10.0 Myr (*bottom, right*). The colour scale corresponds to the migration rate in units au Myr^{-1}, i.e., the change of the semi-major axis per unit of time. Red is migration outwards whereas blue is migration inwards. The x-axis corresponds to the radial distance from the star and the y-axis to the planet mass. Together, these plots describe the migration at various stages of the disk evolution.

significant (see Sec. 4.4). However, the role of non-zero eccentricity (due to the hot-trail effect; Chrenko et al. (2017)) is even more pressing question, which was examined in detail (see Sec. 4.3).

Detailed description of Fig. 4.3 *We list all major events with corresponding time marks. Protoplanets are numbered by their original number and when they collide, a new protoplanet has the number of the more massive one.*

- at 0.56 Myr, the first collision, between the protoplanets number 11 and 12;
- at 0.77 Myr, a collision between 17 and 18;
- at 0.77 Myr, an interesting three-planet interaction between 10, 12 and 13, followed by a collision;
- at 1.00 Myr, a collision between 15 and 16, without any significant eccentricity changes of other planets;
- at 1.47 Myr, a strong resonance between planets 25 and 26, followed by an eccentricity increase of other planets;
- at 1.60 Myr, protoplanets 25 and 26 repeatedly exchange their positions;
- between around 1.5 to 2.1 Myr, chaotic motion of all outer planets (16 to 28);
- between approx. 1.57 and 2.14 Myr, an inward drift of protoplanet 24 from 1.26 to 0.81 au;
- also other protoplanets (28 to 16) drift;
- at 1.90 Myr, a collision of protoplanets 25 and 26;
- from 2.00 to 2.04 Myr, protoplanets 20 and 22 have similar semimajor axes (i.e., a possible coorbital), followed by a collision due to an interaction of the coorbital with another planet;
- at 2.05 Myr, protoplanet 14 is pushed closer to 12, followed by a collision;
- at 2.06 Myr, an three-planet interaction between 18, 21 and 22, followed by a collision;
- all the inner protoplanets 1, 4, 6, 8, 9 and 12 exhibit higher eccentricities, but not a chaotic motion;
- at 2.17 Myr, protoplanets 1 and 4 exchange positions, followed by a collision with a possible involvement of protoplanet 6, jump inwards from 0.490 to 0.478 au (in one output step);
- eccentricities and inclinations rise for all planets, $e \sim 0.06$, $i \sim 1.5°$;
- after 2.4 Myr, eccentricities are damped to less than 0.01;
- between 2.19 and 3.88 Myr, protoplanets are not in chaotic motion;
- outer planets, inward migration, moderate migration rate $-0.069\,\mathrm{Myr}^{-1}$, inner planets, small migration rate $-0.0028\,\mathrm{Myr}^{-1}$;
- at 3.88 Myr, an interaction between protoplanets 18 and 22, orbits were exchanged, the eccentricity of protoplanet 22 rises, interaction with other protoplanets, their eccentricities also rise;
- at 4.04 Myr, protoplanets 16 and 24 exchange orbits, 24 close to 19, followed by a collision;
- at 4.18 Myr, protoplanets 8 and 9 have eccentricities high enough to undergo close encounters, start interacting and exchanging orbits, their semimajor axis separation within 0.005 au, eccentricities up to 0.10, inclinations up to 3°, i.e., the highest values during the whole simulation, damping is weak in rarefied disk;
- between 5 and 6 Myr, small migration rates up to $-0.0050\,\mathrm{Myr}^{-1}$;
- between 10 and 11 Myr, very small migration rates up to $-0.0005\,\mathrm{Myr}^{-1}$, would be significant only on the time scale of 100 Myr, but dissipation is fast;
- a dispersal of the disk, then no significant migration;
- an evolution without any disk, no collisions between 5 and 100 Myr, at 100 Myr, still 14 planets, with eccentricities too low to interact, likely a result of eccentricity damping to zero before dispersal of the disk.

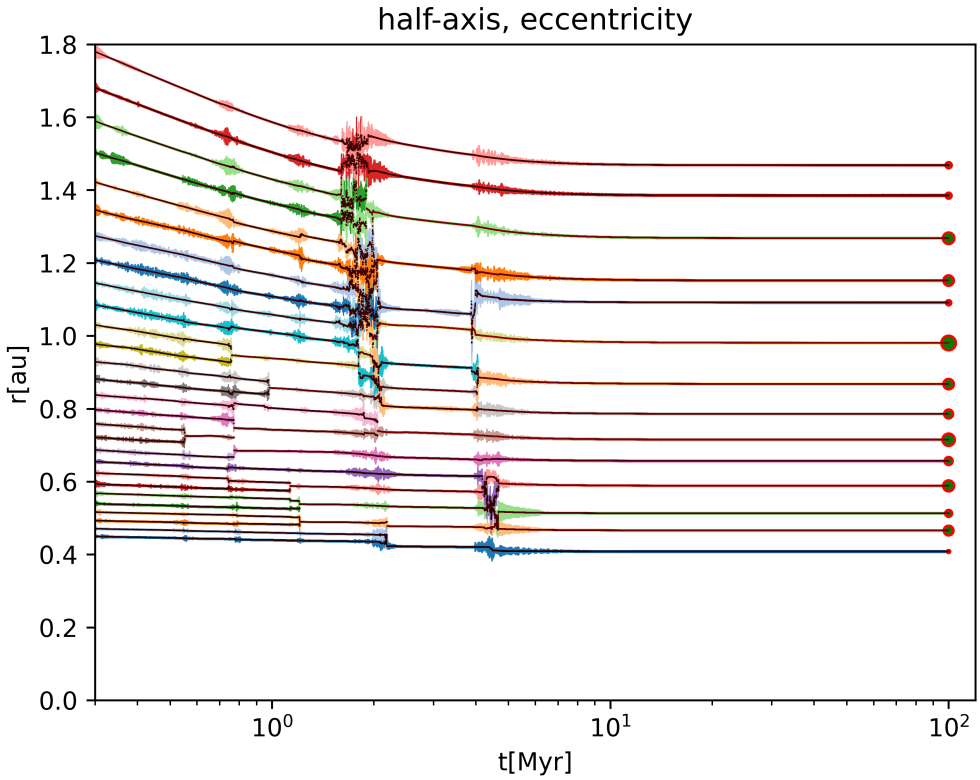

Figure 4.3: Evolution of the system in the MRI inactive weak wind high viscosity model. Orbital evolution of proto-planets is plotted, with colored solid lines representing the semimajor axis dependence on the time. The range between the pericentre and apocentre is represented by vertical bars of different colors, used for an easy recognition of individual planets. The color of the line (black to yellow) is related to the planets' mass. The radius of circles on the right-hand side is proportional to the final masses. This system has 14 planets of masses between 0.05 and 0.24 M_E. A more detailed description of the simulation is bellow.

4.3 MRI inactive weak wind high viscosity model with damping to 0.02

For a less stable and more interacting system than in Sec. 4.2, more eccentric orbits of protoplanets could be helpful. We thus calculated again the previous simulation, with an eccentricity damping to 0.02 instead of to zero.

The evolution of the system is shown in Fig. 4.4. The system is destabilized very early (at 0.4 Myr) in comparison with the previous simulation (first local instability at 0.5 Myr global even after 1 Myr). The main difference, however, is a late instability, which occurred at around 30 Myr. We (and You) have to be aware that from only one run, we cannot be sure if it is systematic for all cases with relaxed damping or only a random event. Prior to the instability, the most massive planet is of 0.29 M_{E}, which is of the same order as 0.24 M_{E} in the previous simulation. Also the number and masses without the late instability do not differ substantially between the two simulations. The difference in final state is mainly caused by the late instability. Evidently, the resulting eccentricities of planets are higher because they are no longer after dispersal damped.

Another difference is that a global early instability now occurs almost at the beginning of the simulation and not after 2 Myr. This happens probably because the protoplanets perturb each other and higher eccentricities also help to break resonant chains (Pierens & Raymond (2016)).

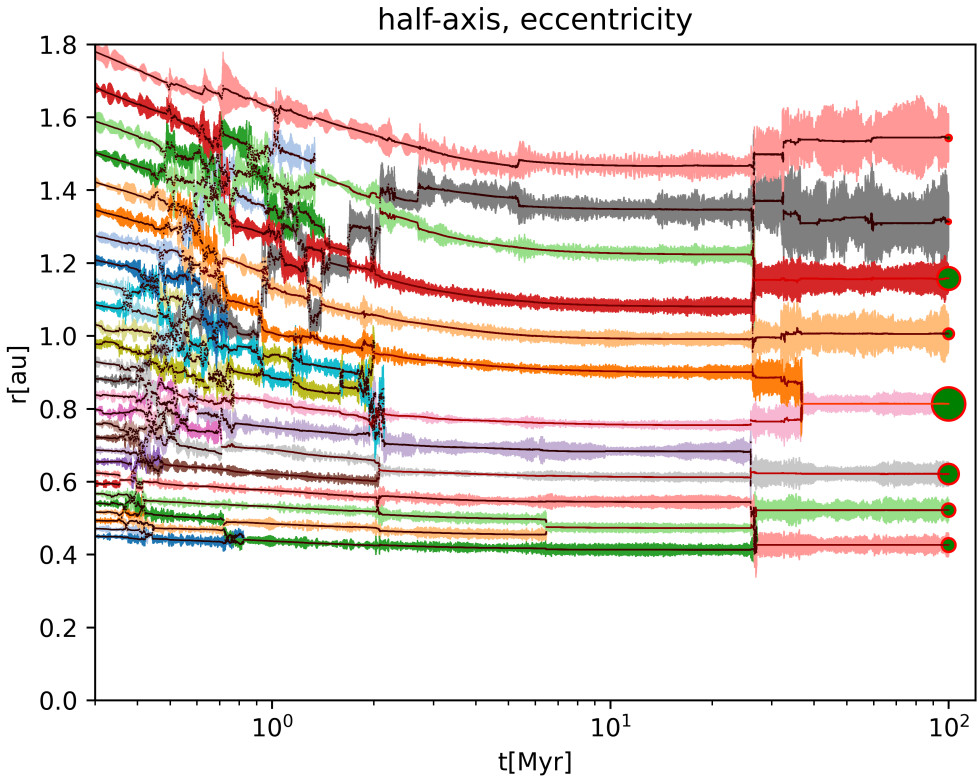

Figure 4.4: MRI inactive weak wind high viscosity model with damping to 0.02. This system has 8 planets of masses between 0.10 and 0.54 $\mathrm{M_E}$. Description of the figure is the same as in Fig. 4.3.

4.4 MRI inactive weak wind low viscosity model ($8 \cdot 10^{-6}$, $10^{-6} f(\Sigma)$, 10^{-6})

To prolong the lifetime of the disk and increase the time span of planetary migration, the parameters for the viscosity and wind were scaled down by one order of magnitude: $\overline{\alpha_{r\phi}} = 8 \cdot 10^{-6}$, $\overline{\alpha_{\phi z}} = 1 \cdot 10^{-6} (\Sigma/\Sigma_0)^{-0.66}$ and $C_{\mathrm{W}} = 1 \cdot 10^{-6}$. Otherwise, the initial conditions were the same as in the previous model.

As a result, the dispersal time of the disk is one order of magnitude longer, nevertheless, the gas surface density profile remains similar to that in the previous model (only with scaled time).

Unfortunately, the planets migrated inwards too rapidly (see Fig. 4.6). For example, the first planet ended at approximately 0.05 au. At this radius, our simulation is no longer relevant, because the time step of Symba is comparable to the orbital period

Convergence zones exist only for planets with masses less than $0.25\,M_{\mathrm{E}}$ (see 4.5, because the migration rate is modified by the lower value of viscosity. The horseshoe drag is more saturated, according to Eq. (2.25), thus the migration is also by one order of magnitude scaled down in masses. Because of a long lifetime of the disk, migration affects planets for much longer time and even after 30 Myr, planets were still slowly migrating.

At around 2 Myr, two planets stopped migrating approximately at 0.15 au, because of their higher eccentricity, around 0.04. A large convergent zone occurs at around 0.15 au for this eccentricity, because of reversal of the Lindblad torque (which then pushes planets outwards, see Eq. (2.38)).

This low-viscosity model did not result in a final state similar to the Solar system. This was mostly due to high migration rate and the absence of a convergent zone for high-mass planets, which would prevent a migration too close to the star. To rescue this kind of model, protoplanets would have to be more massive or more numerous (much more than $2\,M_{\mathrm{E}}$ alltogether). Then some matter could be lost because some protoplanets would fall into the Sun and some protoplanets could remain in the terrestrial zone. However, we shall investigate scenarios without such an extreme loss of matter. Consequently, the next model shall be a compromise in viscosity.

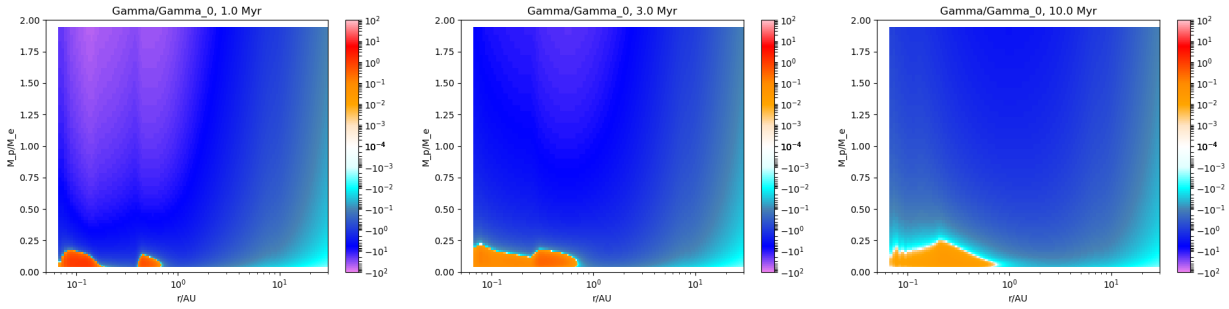

Figure 4.5: Migration maps for the MRI inactive weak wind low viscosity model ($\overline{\alpha_{r\phi}} = 8 \cdot 10^{-6}$, $\overline{\alpha_{\phi z}} = 1 \cdot 10^{-6} (\Sigma/\Sigma_0)^{-0.66}$ and $C_{\mathrm{W}} = 1 \cdot 10^{-6}$). Migration maps are for times (from left to right): 1.0 , 3.0 and 10.0 Myr.

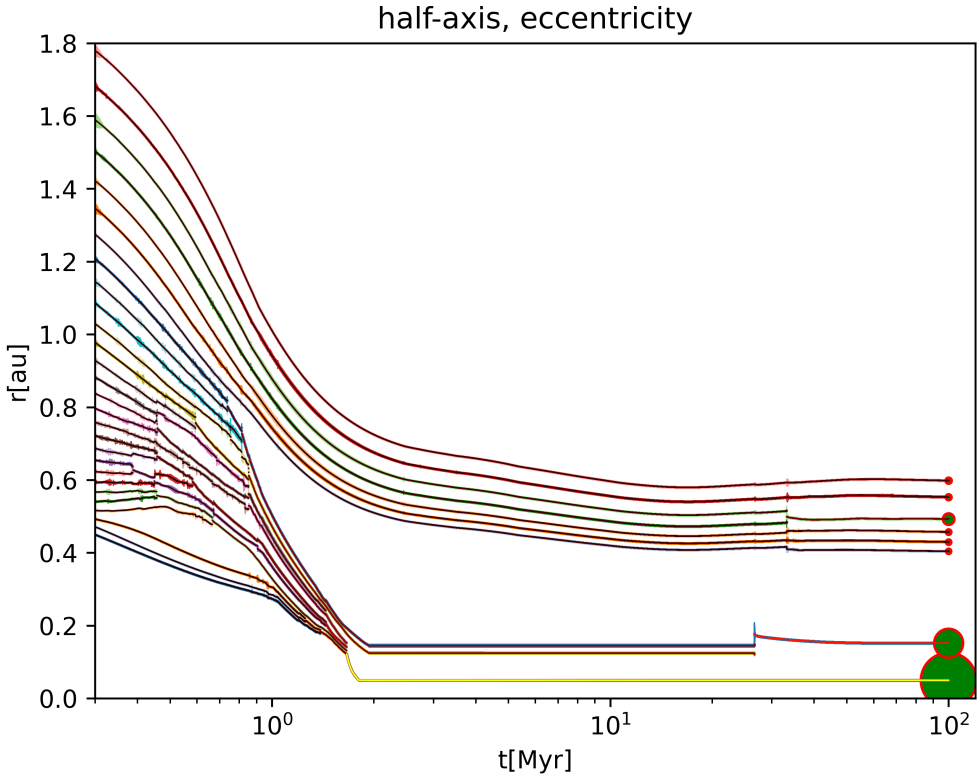

Figure 4.6: MRI inactive weak wind low viscosity model. This system ended with 8 planets. Six outer are located between 0.4 and 0.6 au, having masses between 0.09 and 0.19 M_{E}. Two inner planets migrated towards the inner edge of the disk (boundary condition). They have the masses 0.90 and 0.47 M_{E}. Description of the figure is the same as in Fig. 4.3.

4.5 MRI inactive weak wind intermediate viscosity model ($2.4 \cdot 10^{-5}$, $3 \cdot 10^{-6} f(\Sigma)$, $3 \cdot 10^{-6}$)

The viscosity was lowered by a half order of magnitude compared to the high-viscosity model (Sec. 4.2), consequently, $\overline{\alpha_{r\phi}} = 2.4 \cdot 10^{-5}$, $\overline{\alpha_{\phi z}} = 3 \cdot 10^{-6}(\Sigma/\Sigma_0)^{-0.66}$ and $C_{\mathrm{W}} = 3 \cdot 10^{-6}$.

The surface density profile was again very similar to the low- and high-viscosity models, but with the respective time scale in between. The convergence zone (Fig. 4.8 is larger than in the low-viscosity model and smaller than in the high-viscosity model and it does exist for planets of less than $0.5\,M_{\mathrm{E}}$ (or $0.75\,M_{\mathrm{E}}$ in later stages).

The result is more similar to the terrestrial zone than all the previous models (see Fig. 4.7). Low-mass planets (around $0.1\,M_{\mathrm{E}}$) are located on the edges and more massive (around $0.4\,M_{\mathrm{E}}$) in the middle. After 20 Myr, however, the system was stabilized and ended with a relatively high number of planets (9) of insufficient mass compared to the Solar system. Also the eccentricities and inclinations were very low (less than 0.01 and 0.00001°, respectively), which was expected because of the damping to zero. We decided to compute this simulation again, but with a different eccentricity damping.

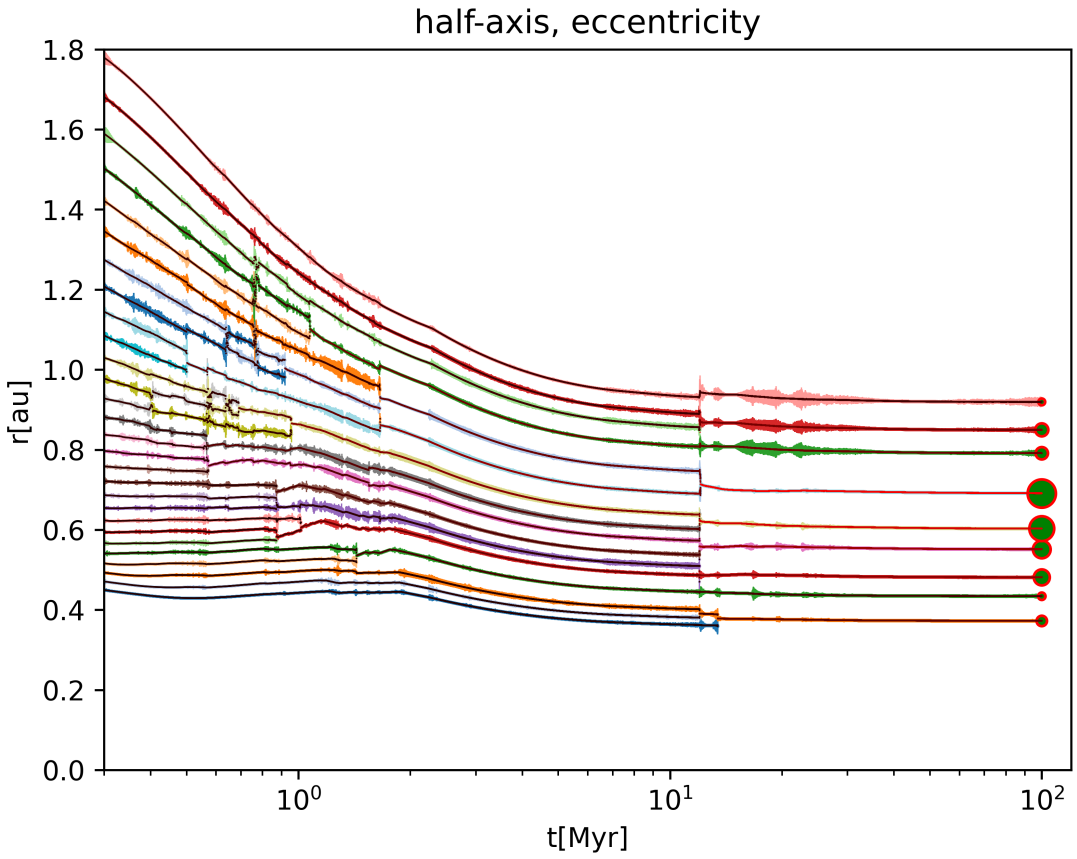

Figure 4.7: MRI inactive weak wind intermediate viscosity model. This system has 9 planets with masses: 0.15, 0.11, 0.24, 0.26, 0.37, 0.42, 0.18, 0.19, 0.10 M_{E}.

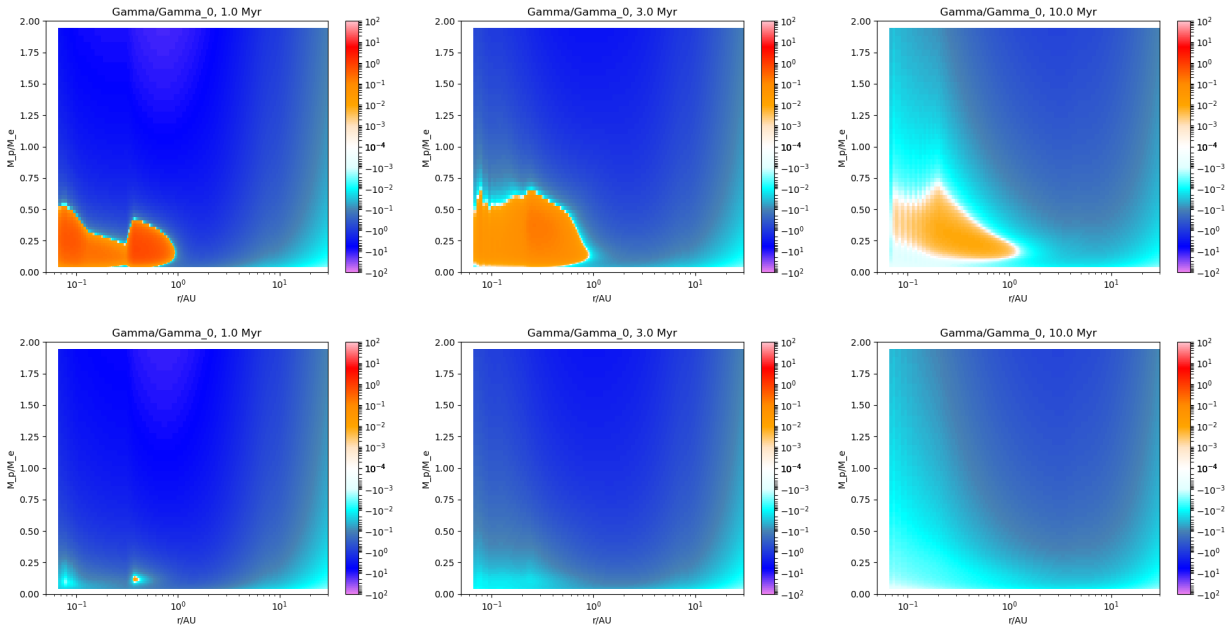

Figure 4.8: Migration maps for the MRI inactive weak wind intermediate viscosity model – for the two different values of the eccentricity: 0.00 (*top*) and 0.02 (*bottom*). The maps are for the times (from the left to the right): 1.0, 3.0 and 10.0 Myr.

4.6 MRI inactive weak wind intermediate viscosity model with damping to 0.02

The next model is the same as in the previous section (weak wind with intermediate viscosity, $\overline{\alpha_{r\phi}} = 2.4{\cdot}10^{-5}$, $\overline{\alpha_{\phi z}} = 3 \cdot 10^{-6}(\Sigma/\Sigma_0)^{-0.66}$ and $C_{\mathrm{W}} = 3 \cdot 10^{-6}$), but now with damping only to 0.02, in order to see, how an increased eccentricity influences the overall migration and formation of planets.

The resulting system is composed of 5 planets with the most massive ($0.83\,M_{\mathrm{E}}$) on the inner edge and the least massive on the outer edge ($0.1\,M_{\mathrm{E}}$) (see Fig. 4.9). A destabilization of the original system and collisions among protoplanets were more rapid, at around 5 Myr, only 6 protoplanets remained (compared to 16 planets at in the simulation with damping to zero). The distribution of masses is completely different than in the previous simulation and the most massive planets are located on the inner edge. This is because of early formation of massive planets, when the disk is still dense and absence of a convergent zone (Fig. 4.8), so they rapidly migrate inwards.

In order to study the behaviour of these intermediate viscosity models, a statistics of more runs would be required. Before we proceed to the statistics, however, we shall primarily investigate strong wind model.

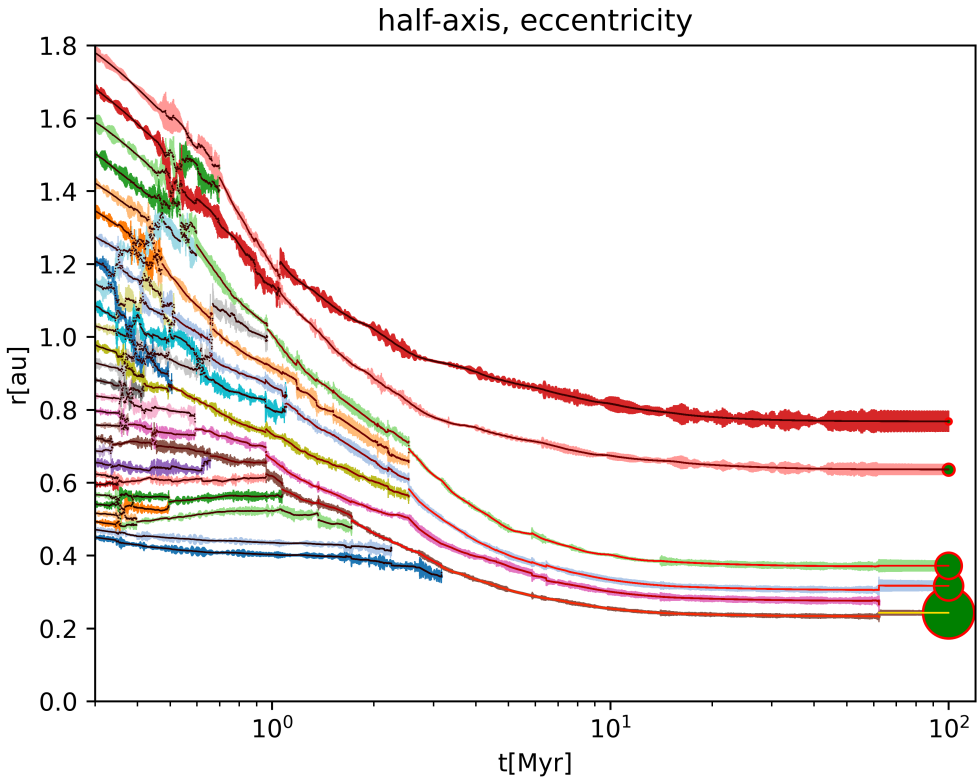

Figure 4.9: MRI inactive weak wind intermediate viscosity model with damping to 0.02. This system has 5 planets of the masses: 0.83, 0.47, 0.43, 0.19, $0.10\,M_{\mathrm{E}}$.

4.7 MRI inactive strong wind low viscosity model ($8{\cdot}10^{-6}$, $10^{-6}f(\Sigma)$, 10^{-6})

Our strong-wind model is driven by Eqs. (1.29) and (1.30) for the radiation losses and the disk wind. We started originally with the same parameters as in Suzuki et al. (2016), i.e., $\overline{\alpha_{r\phi}} = 8 \cdot 10^{-6}$, $\overline{\alpha_{\phi z}} = 1 \cdot 10^{-6}(\Sigma/\Sigma_0)^{-0.66}$ and $C_{\mathrm{W}} = 1 \cdot 10^{-6}$. However, this led to a disk with too short dispersal time and insignificant migration (similarly as in the weak wind high viscosity model in Sec. 4.2). Hence, we decided to investigate the low viscosity case with parameters $\overline{\alpha_{r\phi}} = 8{\cdot}10^{-6}$, $\overline{\alpha_{\phi z}} = 1{\cdot}10^{-6}(\Sigma/\Sigma_0)^{-0.66}$ and $C_{\mathrm{W}} = 1{\cdot}10^{-6}$.

The evolution of disk profiles is plotted in Fig. 4.10 and migration maps in Fig. 4.11. The inverted density profile is even more pronounced and steeper than in the weak wind model, because more matter is carried away by the wind and inner parts of the disk disperse more rapidly. At 30 Myr, the densities reach around $10\,\mathrm{kg\,m^{-2}}$ under 2 au, the migration rate is between -10^{-3} and $-10^{-2}\,\mathrm{au\,Myr^{-1}}$ for planets of Earth or Venus' mass and for less massive it is negligible (less than 10^{-3} in absolute value). At 100 Myr, the disk in the terrestrial zone has the density under $1\,\mathrm{kg\,m^{-2}}$ and the migration rate is completely negligible. Only beyond 5 au, the densities are between 1 and $10\,\mathrm{kg\,m^{-2}}$ and a slow migration could probably persist. As was excepted, it is a long-living disk with a dispersal time around 100 Myr. However, already after 10 Myr no significant migration of planets was apparent in the simulation. The convergent zone reaches higher masses than in the weak-wind simulation with the same parameters ($0.5\,\mathrm{M_E}$ compared to $0.25\,\mathrm{M_E}$).

The resulting system (see Fig. 4.12) is composed of 8 planets with masses from 0.10 to $0.39\,M_{\mathrm{E}}$). An intersting feature is a gap between the 4th and 5th planet (more than 0.2 au compared to 0.05 to 0.1 au between most of the planets). This is caused by a high-mass planet, which appeared around 2.5 Myr, migrated inwards and pushed all the inner bodies inwards, whereas the outer planets continued migrating outwards. This is because of the convergent zone, which does not reach to more than $0.5M_{\mathrm{E}}$ and becomes narrow for higher masses. Although the system is not an Solar system analogue, the migration rates seem to be appropriate. In the next section, we will investigate a model with higher values of the parameters and thus a disk with shorter lifetime (intermediate viscosity).

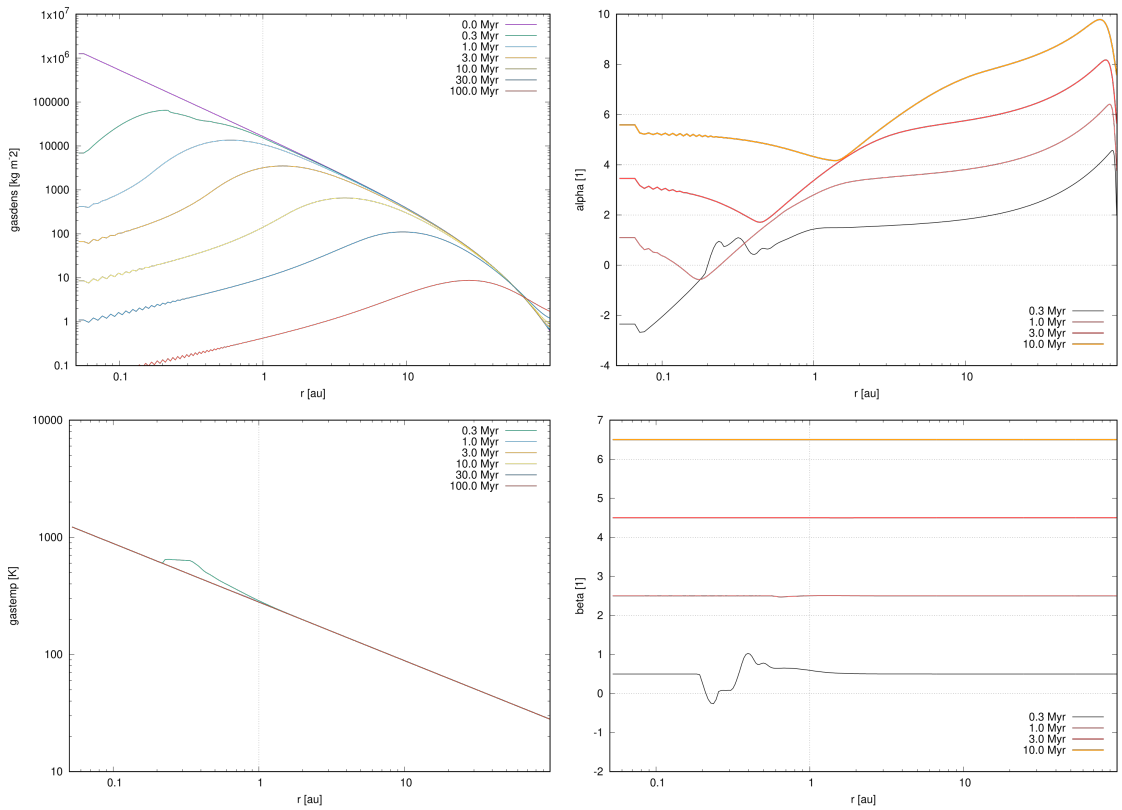

Figure 4.10: Same as Fig. 4.1.

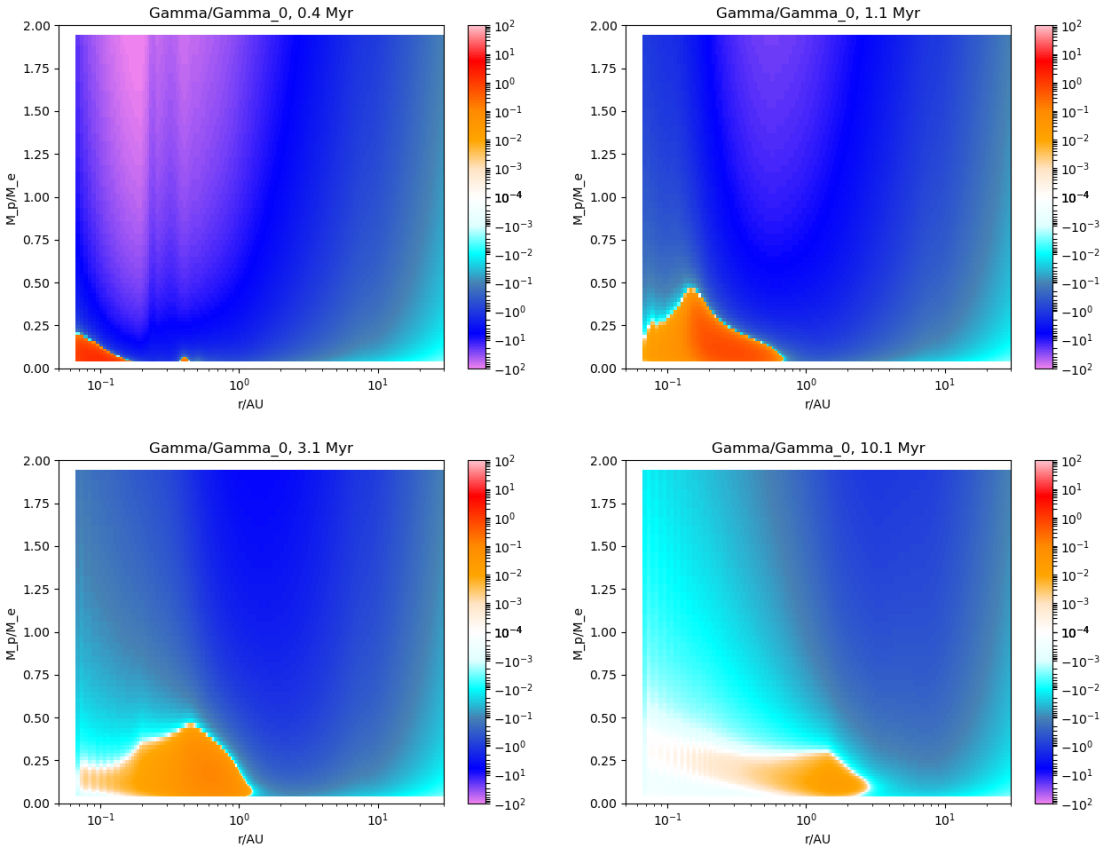

Figure 4.11: Migration maps for the strong wind model with low viscosity ($\overline{\alpha_{r\phi}} = 8 \cdot 10^{-6}$, $\overline{\alpha_{\phi z}} = 1 \cdot 10^{-6}(\Sigma/\Sigma_0)^{-0.66}$ and $C_{\mathrm{W}} = 1 \cdot 10^{-6}$). Same as Fig. 4.1

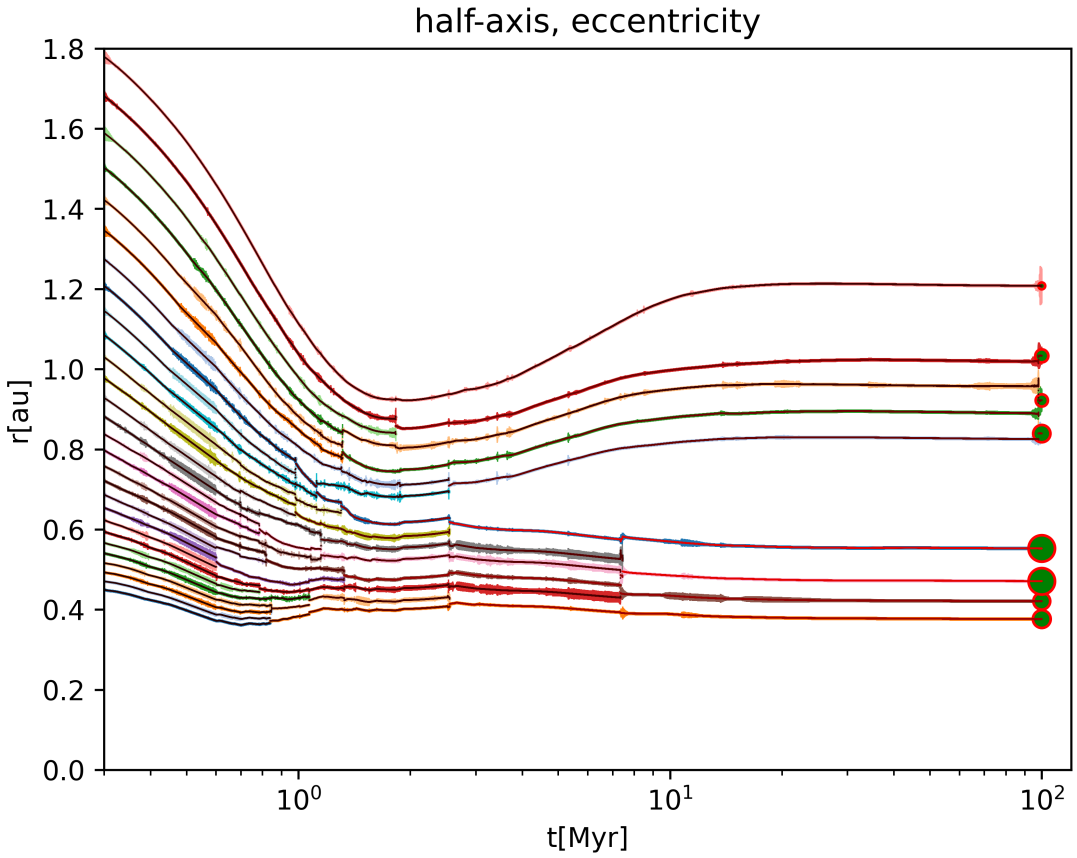

Figure 4.12: MRI inactive strong wind low viscosity model. This system has 8 planets of masses: 0.26, 0.25, 0.39, 0.39, 0.26, 0.18, 0.19, 0.10 M_{E}.

4.8 MRI inactive strong wind intermediate viscosity model ($2.4 \cdot 10^{-5}$, $3 \cdot 10^{-6} f(\Sigma)$, $3 \cdot 10^{-6}$)

Finally, let's investigate the intermediate viscosity case, with the parameters $\overline{\alpha_{r\phi}} = 2.4 \cdot 10^{-5}$, $\overline{\alpha_{\phi z}} = 3 \cdot 10^{-6}(\Sigma/\Sigma_0)^{-0.66}$ and $C_{\mathrm{W}} = 3 \cdot 10^{-6}$. The surface density profiles of the disk are the same and only the lifetime of the disk is 3 times shorter (around 30 Myr). However, after 5 Myr no significant migration of planets was apparent in our simulation (see Fig. 4.13). The migration maps for zero eccentricity contain a convergent zone even for higher masses (around 1.25 M_{E}), see Fig. 5.1.

The resulting system is composed of 8 planets, where 7 of them are low-mass (from 0.09 to 0.25 M_{E}) and one high-mass (0.73 M_{E}). This simulation seems to be successful in creating a high-mass planet around 1 au. Moreover, planets also ended in the correct range of semimajor axis and the migration was sufficient to destabilize the system and drive its evolution. Hence, this model could also be a good candidate for a statistics.

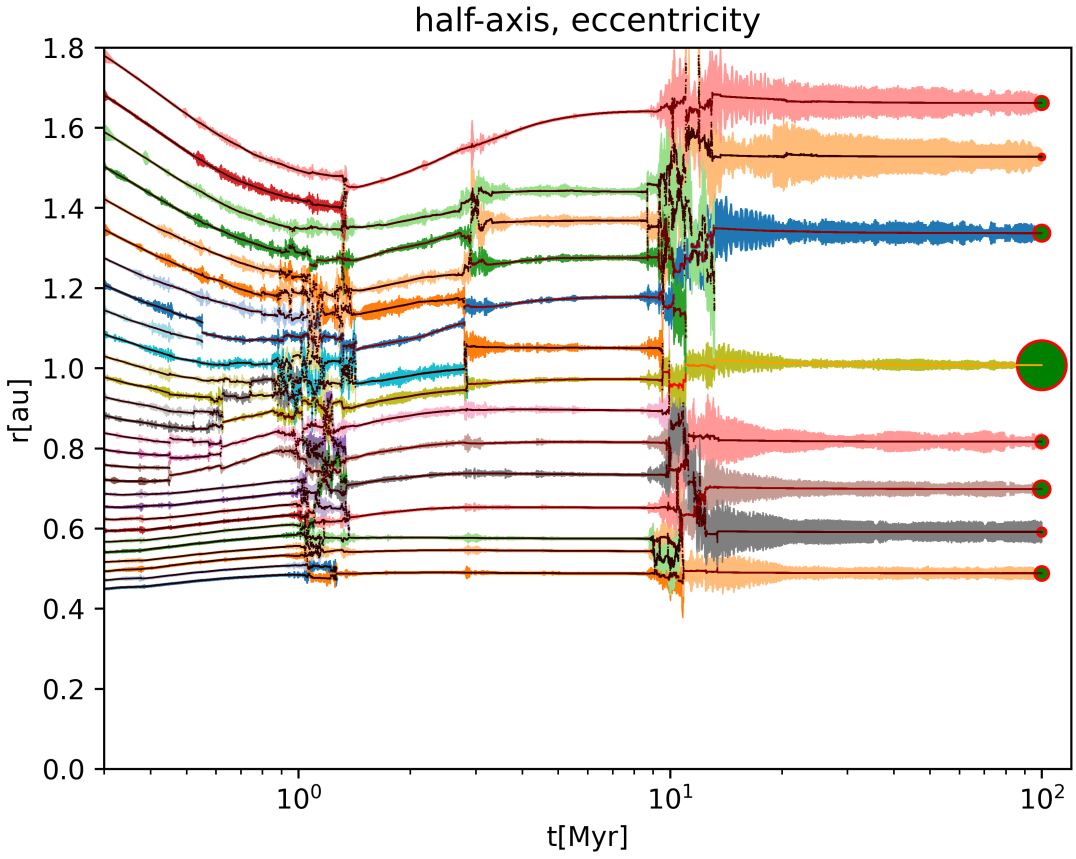

Figure 4.13: MRI inactive strong wind model intermediate viscosity model. This system has 8 planets of masses: 0.21, 0.13, 0.25, 0.18, 0.73, 0.24, 0.09, 0.20 M_{E}.

4.9 Summary and other models

Our analysis is based on the models described in Suzuki et al. (2016). Some of these models lead to an inverted profile, where the surface density increases with the distance from the star in some region. This is an interesting feature, which leads to higher positive corotation torque, and thus to a formation of convergent zone, preventing the migration of protoplanets too close to the star. Moreover, according to Brož et al. (2021), the convergent migration leads to an efficient formation of Solar system analogues. Hence, we examined the Suzuki's MRI inactive weak-wind and strong-wind models, which both lead to a significant inversion of the profile. We computed them for an initial density corresponding to the minimum mass solar nebula (Hayashi (1981)) and for 3 sets of parameters: 1. low ($\overline{\alpha_{r\phi}} = 8 \cdot 10^{-6}$, $\overline{\alpha_{\phi z}} = 1 \cdot 10^{-6}(\Sigma/\Sigma_0)^{-0.66}$, $C_\mathrm{W} = 1 \cdot 10^{-6}$), 2. high ($\overline{\alpha_{r\phi}} = 8 \cdot 10^{-5}$, $\overline{\alpha_{\phi z}} = 1 \cdot 10^{-5}(\Sigma/\Sigma_0)^{-0.66}$, $C_\mathrm{W} = 1 \cdot 10^{-5}$) and 3. intermediate ($\overline{\alpha_{r\phi}} = 2.4 \cdot 10^{-5}$, $\overline{\alpha_{\phi z}} = 3 \cdot 10^{-6}(\Sigma/\Sigma_0)^{-0.66}$, $C_\mathrm{W} = 3 \cdot 10^{-6}$) viscosity and wind. A summary of results is plotted in Fig. 4.14. Firstly, we discuss, how the selection of these parameters influenced the results of simulations.

1. Low viscosity and wind – This led to long-lived disks (up to 100 Myr). Since the viscosity determines saturation of the horseshoe drag (Eq. (2.25)), low viscosity leads to a convergent zone only for low-mass planets (less than 0.25 to 0.5 M_E). In the absence of a convergent zone, high-mass planets can migrate close to the star (well under 1 au) and deplete all the material around. This is mainly the case of weak wind simulation, because close to the star there is enough gas. For the case of strong wind simulation, a rapid dispersal of the disk close to the star can prevent migration under 0.1 au and sustain planets in the terrestrial zone. A possible solution of too rapid migration could be an enlargement of the initial range of protoplanets (extend the range to 3 or more au).

2. High viscosity and wind – This led to short-lived disks (around 10 Myr), often with negligible migration of protoplanets after 3 Myr. The convergent zone is substantially larger and exists even for masses greater than 1 M_E. However, because of too rapid dispersal of the disk, migration is too moderate and does not play a substantial role.

3. Intermediate viscosity and wind – This is a compromise model, which prevents too rapid migration and a loss of planets to the star, dispersal is sufficiently slow to allow for migration to influence enough the formation of the system.

   The weak wind alternative shows some features of the terrestrial zone like low-mass planets on the edges and more massive planets in the middle. However, the collision rate is too low and 9 planets still remain after dispersal of the disk. The planets are less massive than Venus or Earth. An attempt to increase collision rate by relaxing eccentricity damping was done, however, because of steep decrease of the corotation torque with eccentricity, the convergent zone was smaller and could not prevent migration of massive planets inwards. Thus, it led to a completely different result with accumulation of massive planets on the inner edge.

   On the other hand the strong wind led to origin of one high-mass planet in the middle (around 1 au) and other 8 low-mass planets around it. The high-mass planet was formed due to a global instability (at around 10 Myr) of the system accompanied by a significant increase of the eccentricities.

   We also tried a strong wind simulation with eccentricity damping to 0.02 (although it is not described in this chapter). Contrary to the weak wind simulation with damping to 0.02, it did not lead to a loss of massive planets. This is because of rapid dispersal of the disk close to the star. Hence, the model leads to a 'convergent-like zone', which is not caused by a positive torque, but by an absence of gas and slowed migration in regions close to the star.

   Other interesting feature distinguishing the strong- and weak-wind models, which can be seen in Figs. 4.5 and 4.11, is that the convergent zone in the weak wind model less rapidly moves to the right than in the strong wind model. This implies a longer period of migration of low-mass protoplanets and could possibly lead to a more favorable result of the weak wind simulations in case of larger initial range of protoplanets, i.e., the case of protoplanets migrating to the terrestrial zone from the regions of current asteroid belt. Rapid propagation of the convergent zone can complicate migration of low-mass bodies from such distances to the terrestrial zone (before dispersal of the disk).

As we have seen, the behaviour of individual models is really sensitive to the viscosity and wind parameters. Thus, only a relatively narrow range of parameters (within one order of magnitude) leads to sufficiently high migration to converge the protoplanets and low enough to not lose them. It is worth to note, however, that we did not examine other possibilities like greater or lower initial surface density, varying alphas and wind parameters independently or possible influence of additional forces like the thermal torque (Sec. 2.6).

An essential role of the eccentricity was demonstrated as it can help to destabilize the system. Moreover, it modifies migration maps in such a way that for high eccentricities (≥ 0.03) the convergent zone completely

disappears due to reduction of the corotation torque. Let's note that for even higher eccentricities (≥ 0.05), another convergent zone appears due to inversion of the Lindblad torque occurs. It is not dependent on the mass so much and does not move much with time (see Fig. 5.1). Instead it moves to greater distances with increasing eccentricity.

The strong wind model with intermediate viscosity and wind led to the most promising results. Hence, we decided to compute a statistics of multiple runs for it.

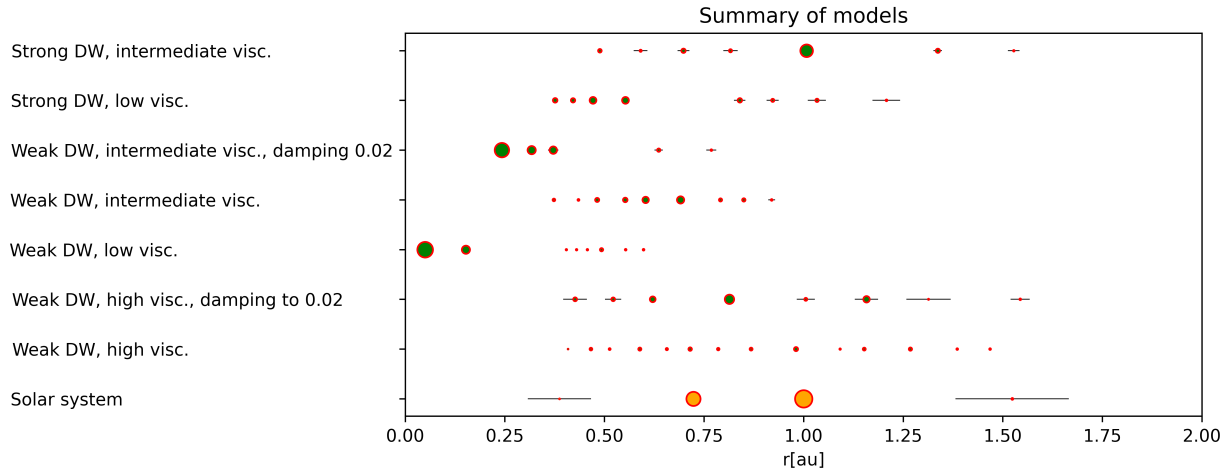

Figure 4.14: A summary of all individual simulations presented in Chap. 4. The final states (after 100 Myr) of simulations are plotted in the rows and the y-axis labels describe the individual simulations. Planets are represented by circles; its center represents the semimajor axis and its diameter the mass. Thin horizontal lines represent the range of pericentre to apocentre, due to the eccentricity. For reference, the Solar system is also plotted.

5. Simulations' statistics – variations of initial conditions

An N-body problem represents a chaotic system; its evolution is sometimes extremely sensitive to the initial conditions. This implies that one simulation is not fully representative and not sufficient to describe all the possibilities of evolutionary pathways.

In our context, it is necessary to replace fixed initial conditions for protoplanets by a set of varied initial conditions and compute a statistics of the results, to determine how sensitive they actually are.

The simulation chosen for computing statistics was the MRI inactive strong wind intermediate viscosity simulation (Chap. 4, Sec. 4.8), because these systematically led to reasonable match of the Solar system architecture, when only one run was computed.

Solar system analogues. We search for Solar system analogues, and hence for this purpose, we define an analogue as a system which ended with less than 7 planets and at least one planet more massive than $0.7\,M_E$ and the innermost and outermost planet less massive than $0.35\,M_E$.

5.1 Statistics of strong wind simulation with damping to zero

We performed a set of 25 runs, each with 28 protoplanets, but with slightly varied initial positions of the protoplanets, velocities or masses. This was done in several different ways: by inversion of positions of some protoplanets (a shift by 180° forward in its orbit), modification in some of the coordinates or velocities (small enough to not change their semimajor axis, eccentricity or inclination significantly), negligible perturbation in the masses of protoplanets. All changes were less than 1 % and no global changes of the distribution of the protoplanets were done (e.g., extending the range of semimajor axes of protoplanets or spacing between them, or their count) in order *not* to change the behaviour of the system in a systematic way. Moreover, the initial and boundary conditions of the 'hydro' were not modified. The same parameters as in the previous run of the MRI inactive strong wind intermediate viscosity model, however, the eccentricity and inclination damping to zero were used (see Sec. 4.8). Let's recall that respective parameters were $\alpha_{r\phi} = 2.4 \cdot 10^{-5}$, $\alpha_{\phi z} = 3 \cdot 10^{-6}$ and $C_{\mathrm{W}} = 3 \cdot 10^{-6}$. The migration maps are shown in Fig. 5.1, where for the low eccentricities (≤ 0.04) dominates a convergence zone due the Corotation torque and for high (≥ 0.04) a convergence zone due to inversal of the Lindblad torque.

The final states after 100 Myr are shown in Fig. 5.2. They are quite diverse in terms of number of planets (3 to 13) as well as their eccentricities. According to the number vs. the mean eccentricity of planets dependence (Fig. 5.3), the final states can be separated into two groups. This separation also can be seen in the semimajor axis vs. the mass dependence (Fig. 5.4).

The systems of the first group end with too many low-mass planets (9 to 13 planets less than $0.25\,M_{\mathrm{E}}$, the most massive $\approx 0.6\,M_{\mathrm{E}}$), and too low eccentricities (between 0.001 and 0.01). This group represents the systems, where only *early* instabilities occured, and planetary migration is still substantial (before dispersal of the disk at ≈ 10 Myr). In some runs, only local instabilities were present (run 14, Fig. 5.5), whereas in others large scale instabilities and significant transport of material occurred (run 8, Fig. 5.6). For example the 23-th protoplanet travels between 2.6 Myr and 4 Myr from 1.27 to 0.53 au. In this run, also an interesting co-orbital planet exists between 2 and 2.6 Myr around 1.15 au.

The systems of the second group end up with a low number of high-mass planets (3 to 6 planets of mass from 0.75 to $1.25\,M_{\mathrm{E}}$) and low-mass outer planets having relatively high eccentricity (some of them more than 0.1). This group represents the systems, where *late* instabilities occur (after 10 Myr), which are often global, involving the whole system. Some of the systems are still interacting and unstable after 100 Myr. For example, in run 23 in Fig. 5.7, there is large-scale instability occurring between ≈ 35 and 70 Myr, with a significant transport and mixing of material. These late global instabilities seem to be an important mechanism leading to high-mass planets comparable to the Earth or Venus. The mechanism causing these instabilities is mainly a 'repulsion', facilitated by close-to-zero inclinations, pushing two protoplanets away from each other and leading to a close encounter with another protoplanet, destabilizing whole compact system.

Only the runs of the second group are somewhat comparable to the Solar system in the number of planets and lead to growth of planets up to the mass comparable to Venus or the Earth. They are commonly located somewhere in the middle while outer planets end up with the mass comparable to Mars. However, the innermost planet is often too massive to be comparable to Mercury and also high-mass planets has often too

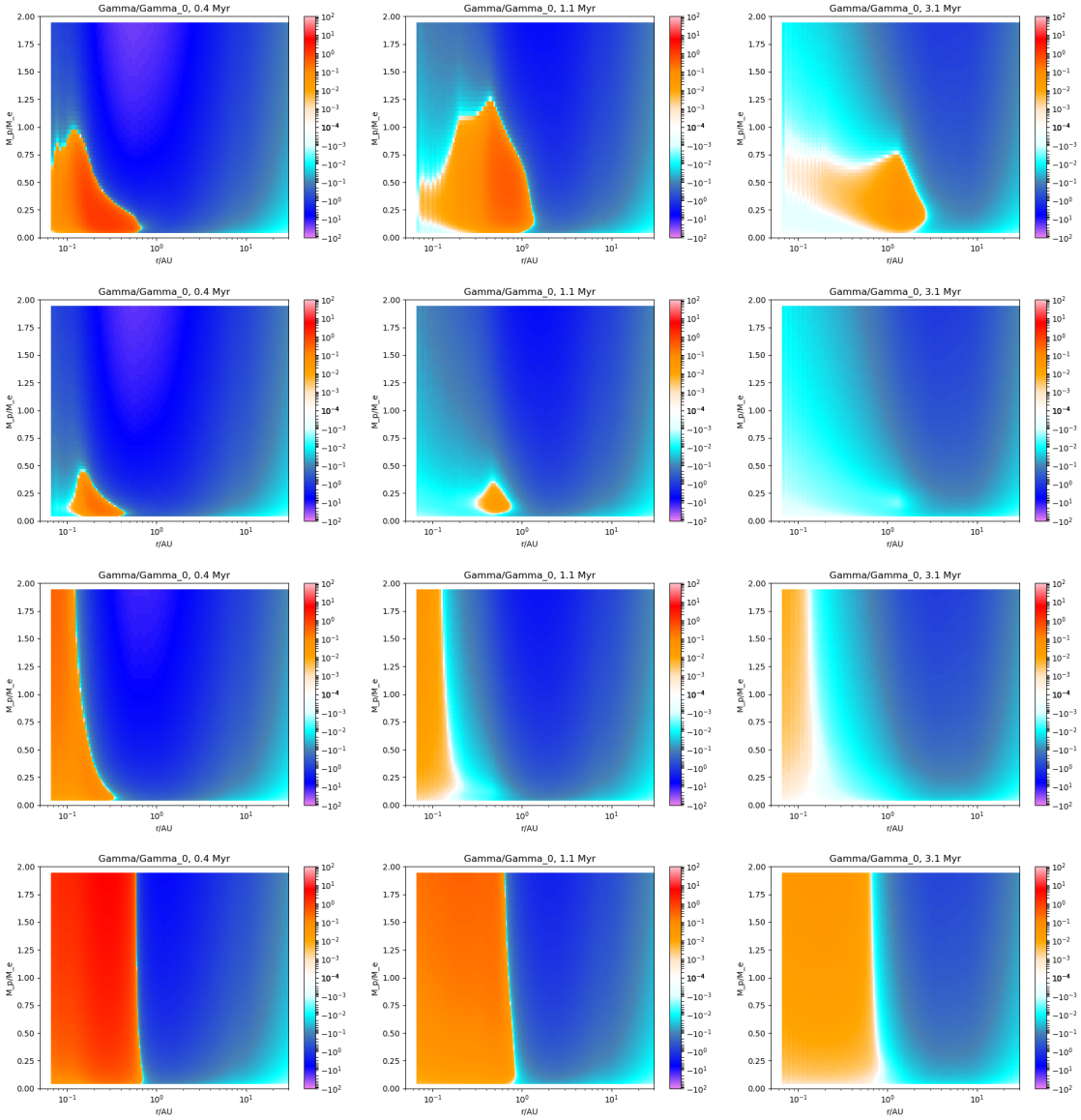

Figure 5.1: Migration maps for the MRI inactive strong wind intermediate viscosity simulation. The colour scale corresponds to the migration rate in units auMyr^{-1}, for various times (from left to right): 0.3, 1, 3 Myr. Together, the plots describe the migration in various stages of the disk evolution.

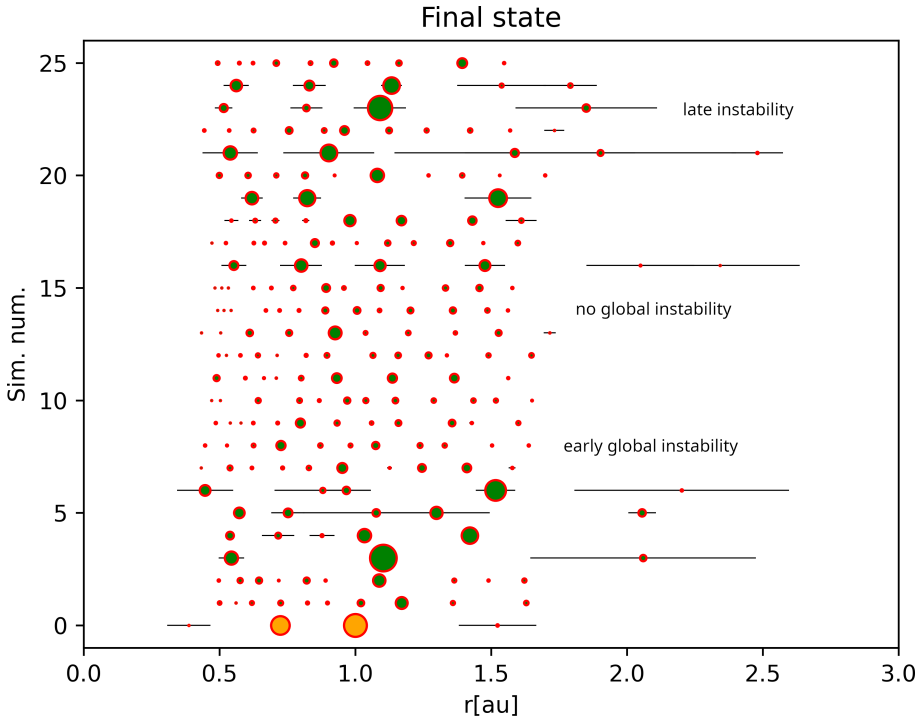

Figure 5.2: Statistics of strong wind simulation with damping to zero – the final states after 100 Myr. The runs are plotted in the rows and y-axis represents the number of the run. Planets are represented by circles; its center represents the semimajor axis and the diameter the mass. Thin horizontal lines represent the range of pericentre to apocentre, due to the eccentricity. For reference, 0 is the Solar system. The evolution of the marked systems (no global instability, early global instability, late instability) is plotted in Figs. 5.5,5.6 and 5.7

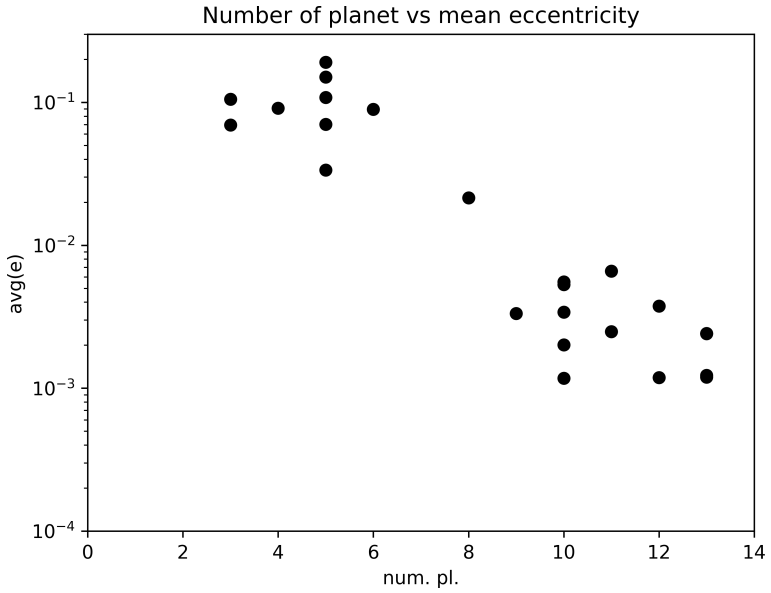

Figure 5.3: Systems from Fig. 5.2 – final number of planets vs. average eccentricity (arithmetic mean). Each point represents one run. A separation of the final states into two groups (one high number – low eccentricity, another low number – high eccentricity) can be clearly seen.

large separation compared to 0.28 au of Venus and the Earth. Overall, this simulation did not provided any good analogues of the Solar system (according to our definition).

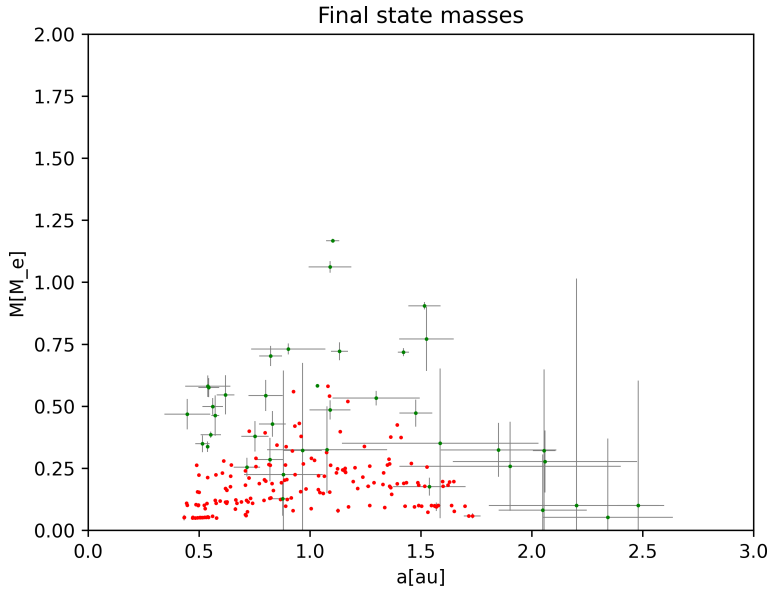

Figure 5.4: Final planets' masses and semimajor axes of all the systems from Fig. 5.2. The points represents planets. The horizontal bars represents the pericenter to apocenter range and the vertical bars represents the range between the highest point above and the lowest under the ecliptic plane; both with respect of the dimensions of the horizontal axis). The planets of the runs ending with high number or low number of planets are red or green respectively.

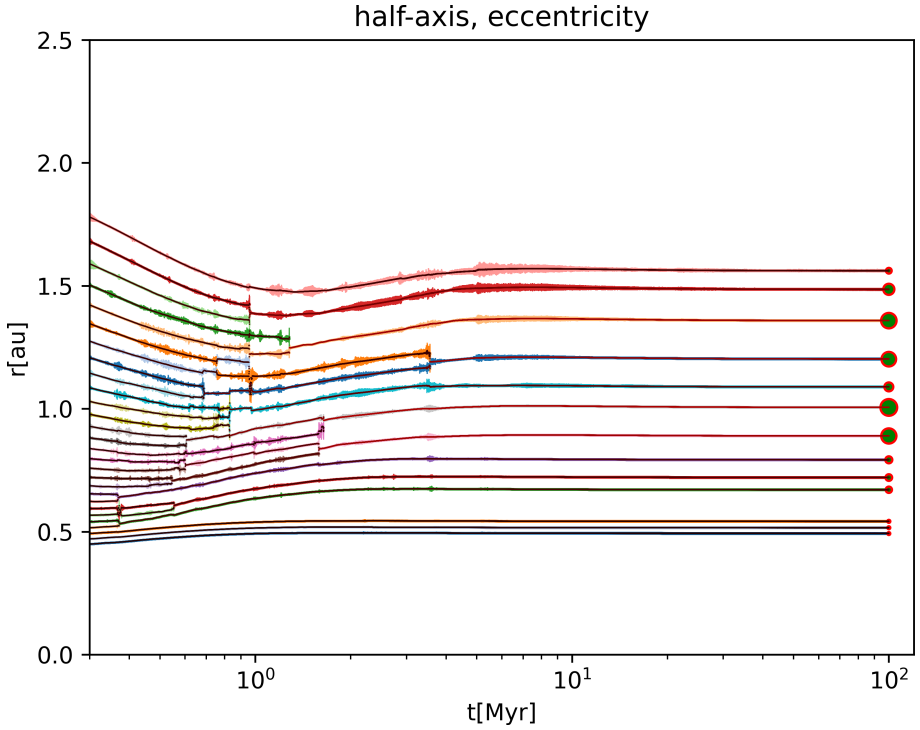

Figure 5.5: The run 14 of statistics – no global instability. This system has with 13 planets with masses between 0.05 and 0.29 M_{E} . The orbital evolution of the planets is plotted, with colored solid lines representing the semimajor axis dependence on the time. The range between the pericenter and apocenter of the planets is represented by vertical bars of different colors, used for an easy recognition of individual planets. The color of the line (black to yellow) is related to the planets' mass. The radius of circles on the right-hand side is proportional to the final mass.

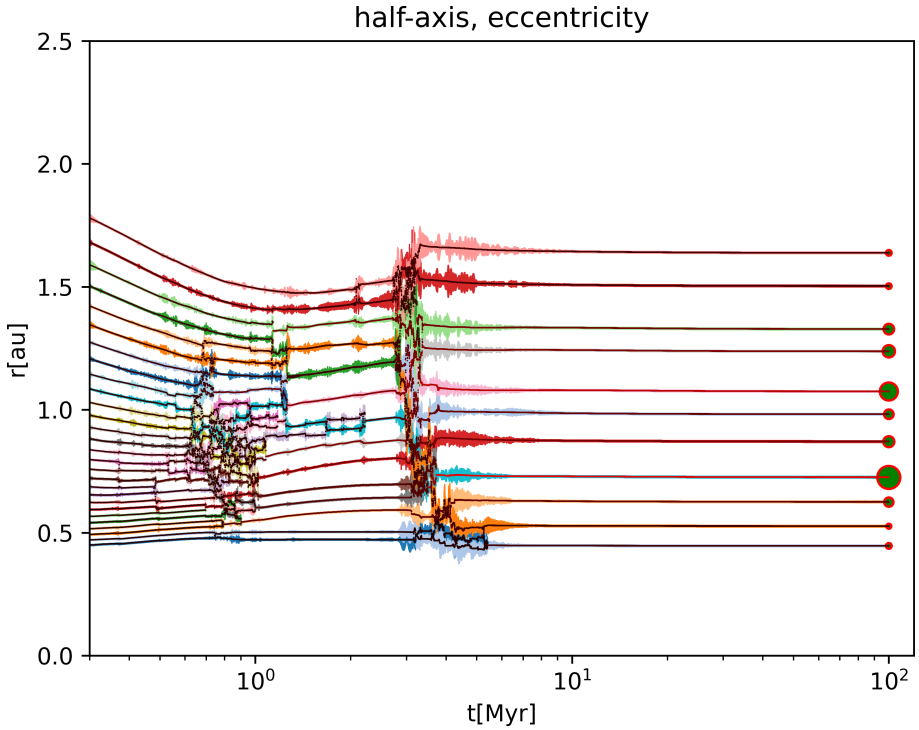

Figure 5.6: The run 8 of statistics – an early instability. Besides local instabilities, two global ones occur at around 0.8 and 3 Myr. This system has 11 planets with masses between 0.09 and 0.40 M_{E}.

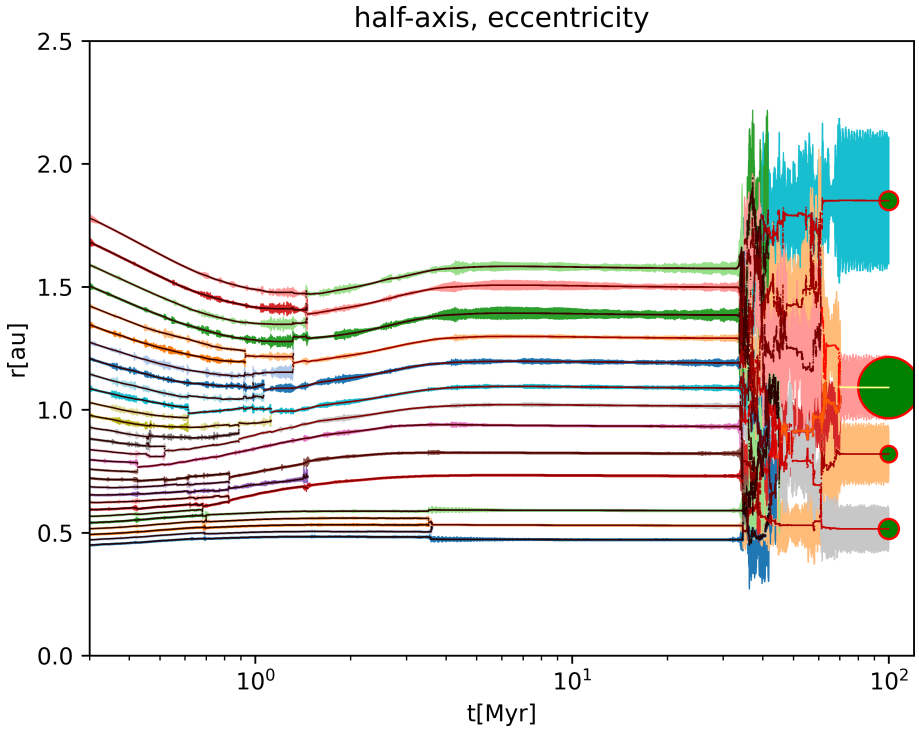

Figure 5.7: The run 23 of statistics – late instability. Besides early local instabilities one late global instability occurs at $\approx$ 35 Myr. This system has 4 planets with the masses 0.35, 0.29, 1.06, 0.32 M_{E}, the semimajor axes 0.52, 0.82, 1.09, 1.85 au, the eccentricities 0.063, 0.072, 0.088, 0.14 and the inclinations 3.7°, 6.1°, 1.2°, 3.4°.

5.2 Eccentricity damped to 0.04 (hot-trail effect)

This simulates the case, when something physically 'blocks' the damping to zero considered by Tanaka & Ward (2004) (see Sec. 2.1.2). This can be, for example, the heating force or the hot-trail effect (Chap. 2, Sec. 2.6).

Firstly, we decided to study the case, when the inclinations are left as before to be damped to zero, but the eccentricity is damped only to 0.04. The initial and boundary conditions for the 'hydro' as well as protoplanets are left same as in Sec. 5.1.

The final states after 100 Myr (Fig. 5.8) now cannot be separated clearly into two groups as before, the pattern distinguishing runs with low number of planets of high eccentricity and high number of planets of low eccentricity is still present, but it is less obvious. New feature apparent in this statistics, clearly visible in Fig. 5.9, is the absence of low-mass planets (of mass comparable to the initial distribution) around the middle (0.6 to 1.4 au).

Only the runs 9, 14, 20, 25 end up with a planet more massive than Venus. Similarly as in the simulation without damping, these 'successful' runs contain late global instabilities and also did not lead to a low-mass planet similar to Mercury on the inner edge of the terrestrial zone. In both simulations, in the region around 0.5 au there are planets of mass around $0.5 M_{\mathrm{E}}$. Nevertheless, both simulations lead to low-mass planets combarable to Mars on the outer edge. In Fig. 5.10, run 20 is shown, which ended with the architecture most similar to the Solar system.

Some runs ended with the largest planet of around Venus' mass , but they are still interesting and viable Solar system analogues; for example run 1, Fig. 5.11 and also runs 3, 4, 5, 10, 13. These compromise runs did not end with so massive Mercury. Late instabilities in these runs still occur but they are generally less violent and more local.

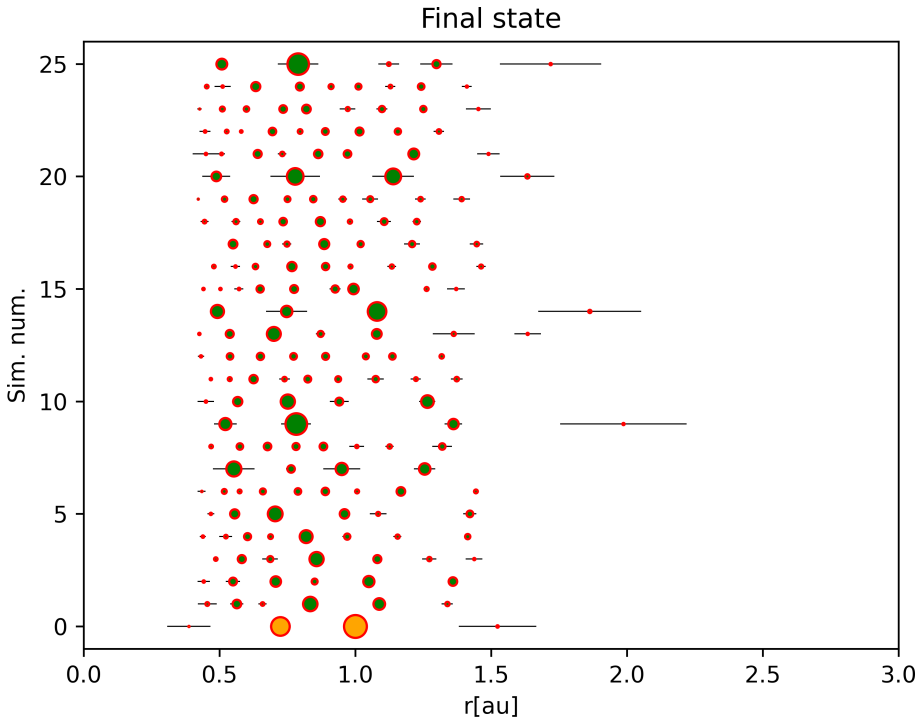

Figure 5.8: Final state of strong wind simulation with eccentricity damped to 0.04 at 100 Myr. Axes and other marks in the figure are same as in Fig. 5.2.

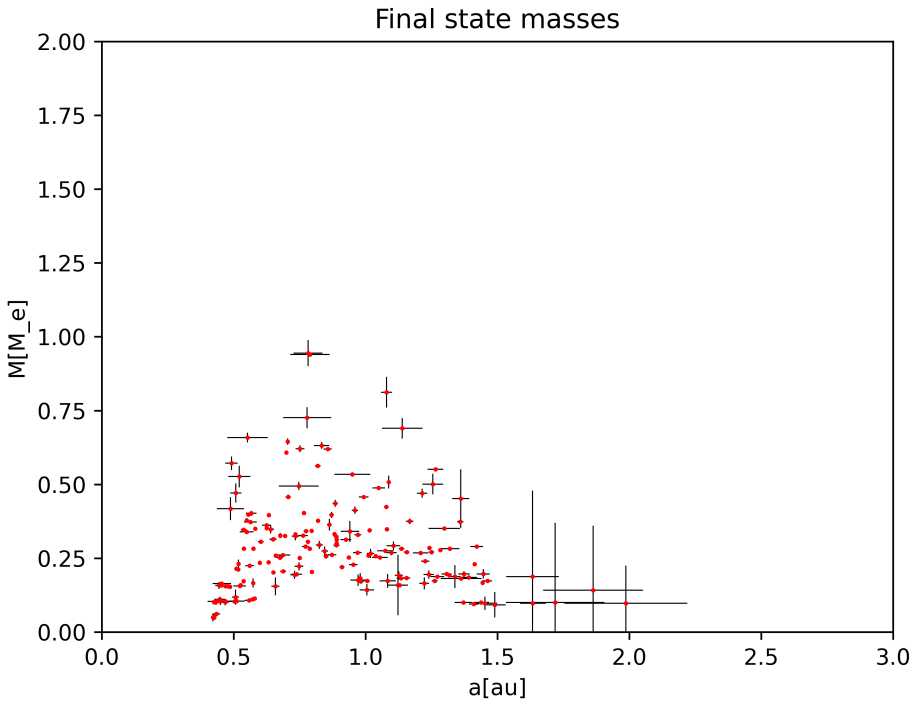

Figure 5.9: All final state planets' masses and semimajor axes. An absence of low mass planets in the middle (original protoplanets) is clearly visible.

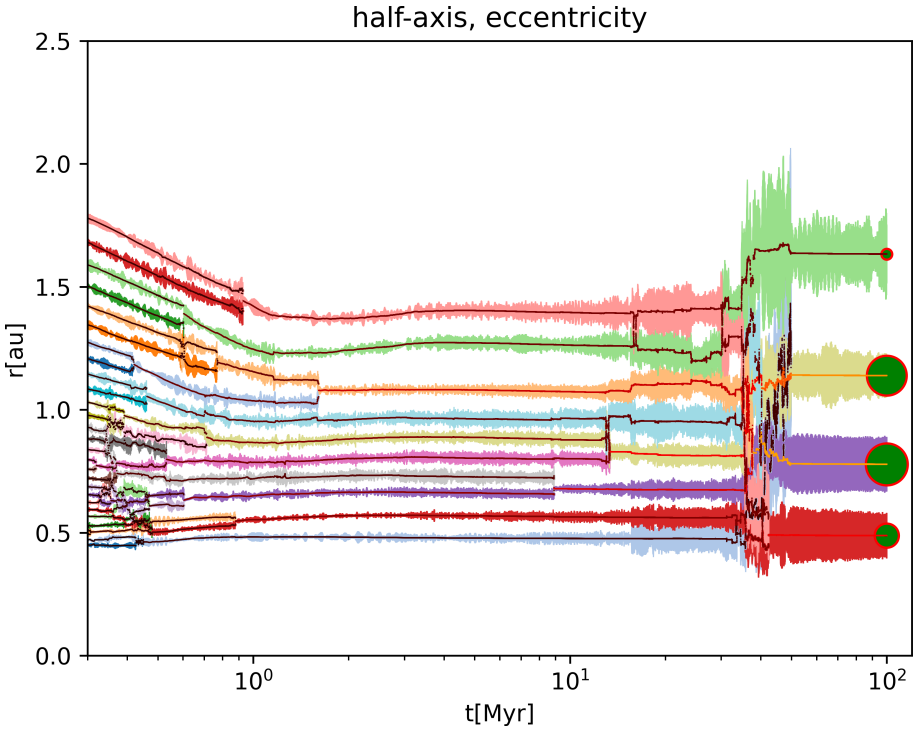

Figure 5.10: The run 20 of statistics – local early instabilities and one global instability, which occurs between $\approx$ 30 and 45 Myr. This system has 4 planets with masses 0.42, 0.73, 0.69, 0.19 M_E, the semimajor axes 0.49, 0.79, 1.14, 1.63 au, the eccentricities 0.11, 0.12, 0.067, 0.061, and the inclinations 4.6°, 2.6°, 1.8°, 10.3°.

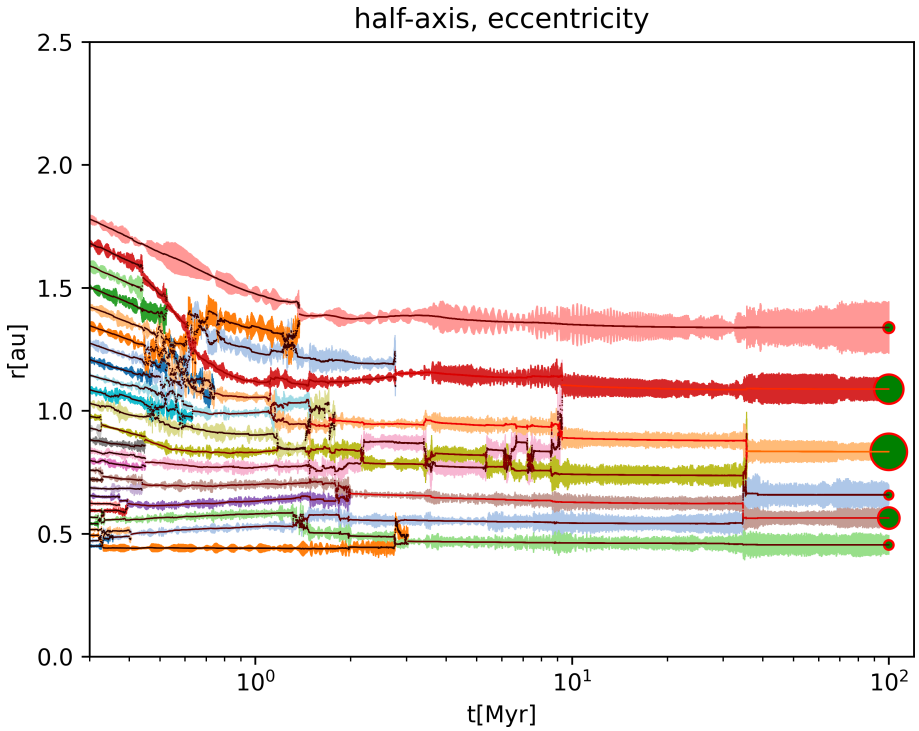

Figure 5.11: The run 1 of statistics – an early global instability and one late0 more local instability, which occurs around 33 Myr. This system has 6 planets with masses 0.16, 0.37, 0.16, 0.63, 0.51 M_{E}, the semimajor axes 0.45, 0.56, 0.66, 0.83, 1.09, 1.34 au, the eccentricities 0.077, 0.043, 0.023, 0.034, 0.003, 0.015, and the inclinations 0.7°, 0.5°, 2.6°, 0.8°, 1.2°, 1.7°.

5.3 Eccentricity damped and also forced to 0.04

We performed again the simulation with damping to 0.04, but hereinafter we also *forced* the eccentricity to that value. All initial and boundary conditions were left the same.

The final states (Fig. 5.12) now cannot be separated into 2 distinct groups. It seems that large-scale global instabilities were less frequent than in the simulation with damping to zero (Sec. 5.1) and this eventually led to generally less massive and less eccentric planets (only 2 planets in all runs together had the eccentricity greater than 0.1). The resulting systems were also more compact (almost all planets were located between 0.4 and 1.6 au, whereas in the previous simulations, there were many planets beyond 1.6 au and some of them reached even 2.5 au). In the middle, between 0.5 and 1.0 au, no low-mass planets or initial protoplanets were left (see Fig. 5.13), similarly as in the previous simulation.

The run 5 final state is similar to the Solar system because it has two massive planets of around Venus' size close together and they are even less separated than Venus and the Earth. However, another an instability with some collisions started after 90 Myr and we cannot be sure if the final system is stable or not. In order to determine this, a simulation up to to 1 Gyr long would be necessary.

Another possible analogue of the Solar system could be run 3, which exhibited a large global instability between 25 and 50 Myr and became stable after that. Another analogue could be run 23 which was globally unstable until around 12 Myr and then only local instabilities occurred between 45 and 60 Myr.

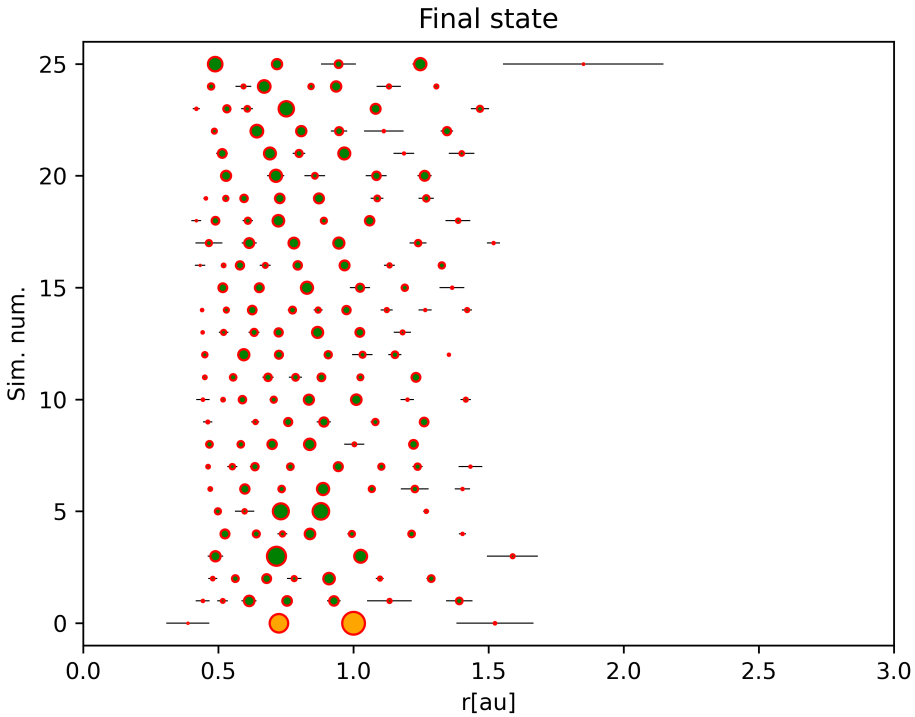

Figure 5.12: Final state at 100 Myr of strong wind simulation with eccentricity damped and also forced to 0.04. Axes and other marks in the figure are same as in Fig. 5.2

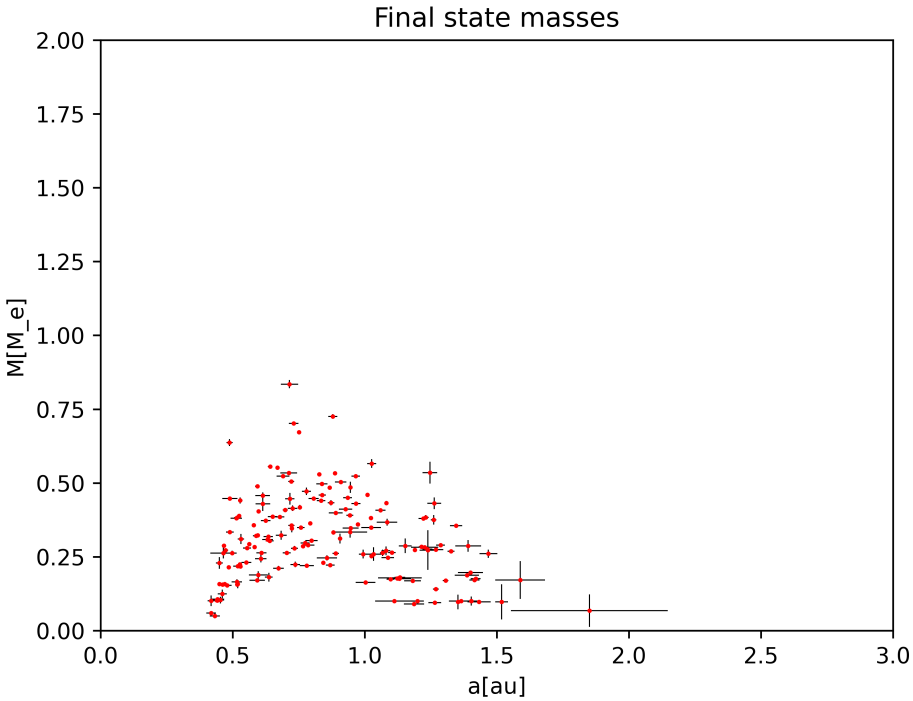

Figure 5.13: All final state planets' masses and semimajor axes. Absence of low mass planets in the middle (original protoplanets) is clearly visible.

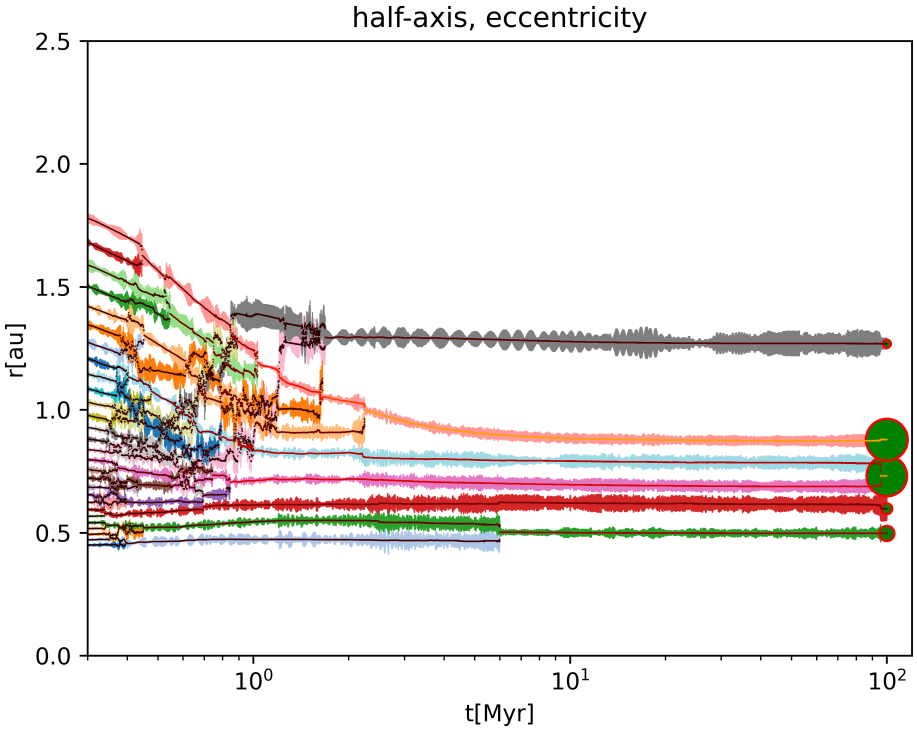

Figure 5.14: The run 5 of statistics – early instabilities and some late instability starting just before 100 Myr. This system has 5 planets with masses 0.26, 0.19, 0.70, 0.73, 0.14 M_{E}, the semimajor axes 0.50, 0.60, 0.73, 0.88, 1.27 au, the eccentricities 0.022, 0.06, 0.025, 0.02, 0.009, and the inclinations 0.9°, 1.2°, 0.4°, 0.5°, 0.2°.

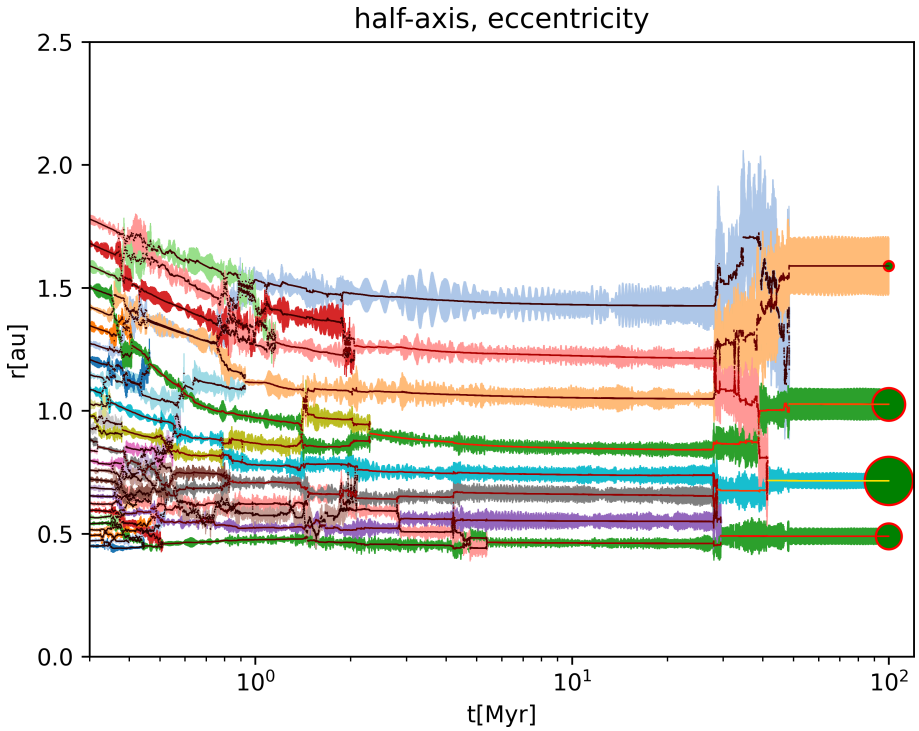

Figure 5.15: The run 3 of statistics – a late global instability between 25 and 50 Myr. This system has 4 planets with masses 0.45, 0.85, 0.57, 0.17 M_{E}, the semimajor axes 0.49, 0.71, 1.03, 1.59 au, the eccentricities 0.06, 0.05, 0.016, 0.06, and the inclinations 0.5°, 1.1°, 0.8°, 2.3°.

5.4 Eccentricity damped and also forced to 0.07

The convergent zone due to the corotation torque disappears for moderate eccentricities around 0.04. For high eccentricities (even more than 0.04), a convergent zone due to inversion of the Lindblad torque occurs (Eq. (2.38) and Fig. 5.1). Thus, an interesting idea is to damp and force even to higher eccentricities around 0.07 and see if such a convergent zone, which is more stable and independent of time and mass, will lead to more successful results in terms of the Solar system analogues. All the initial conditions were left same as before.

The results after 100 Myr are shown in Figs. 5.16 and 5.17. High-mass planets comparable to Venus and Earth occur in the middle of the terrestrial zone and also low-mass planets comparable to Mercury and Mars occur on the edges without any problems. The eccentricities of more massive planets seem to be generally lower than those of less massive planets. Similarly as in all preceding simulations, except that with damping to zero, no low-mass planets (less than $0.2M_{\mathrm{E}}$) or original protoplanets are left in the middle range (between 0.75 and 1.4 au). The most massive planets (more than Venus, $0.82M_{\mathrm{E}}$) occur between 0.6 and 1.2 au, while the remaining low-mass planets in the range 0.3 to 0.75 au and then also in the range 1.4 to 2.5 au.

The runs 2, 8, 18 (Fig. 5.20), 24 (Fig. 5.19) and 25 (Fig. 5.18) were the most analogous to the Solar system. The run 18 ended with substantially higher eccentricities and inclinations, between 0.04 to 0.28 and 1.0° to 19.8°, than runs 2, 24, 25, where eccentricities did not exceed 0.09 and inclinations are of the order of percents or even tenth of a percent. Similarly, run 8 ended with higher eccentricities and inclinations. In run 18, late instabilities occur between 20 and 40 Myr and then between 60 and 85 Myr, whereas in run 24, the system instabilities occur until 20 Myr and in run 25 until 25 Myr and system than seems stable. The systems in runs 18 and 25 can still be interacting and unstable because of large eccentricities of the outer two planets, crossing each others' orbits.

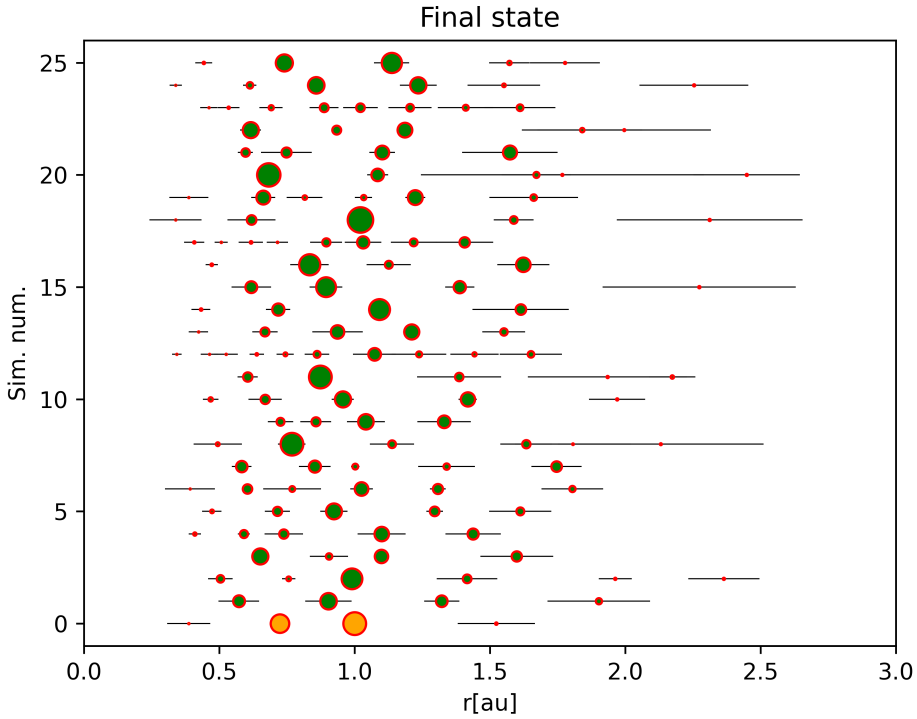

Figure 5.16: Final state at 100 Myr of strong wind simulation with eccentricity damped and also forced to 0.07. Axes and other marks in the figure are same as in Fig. 5.2.

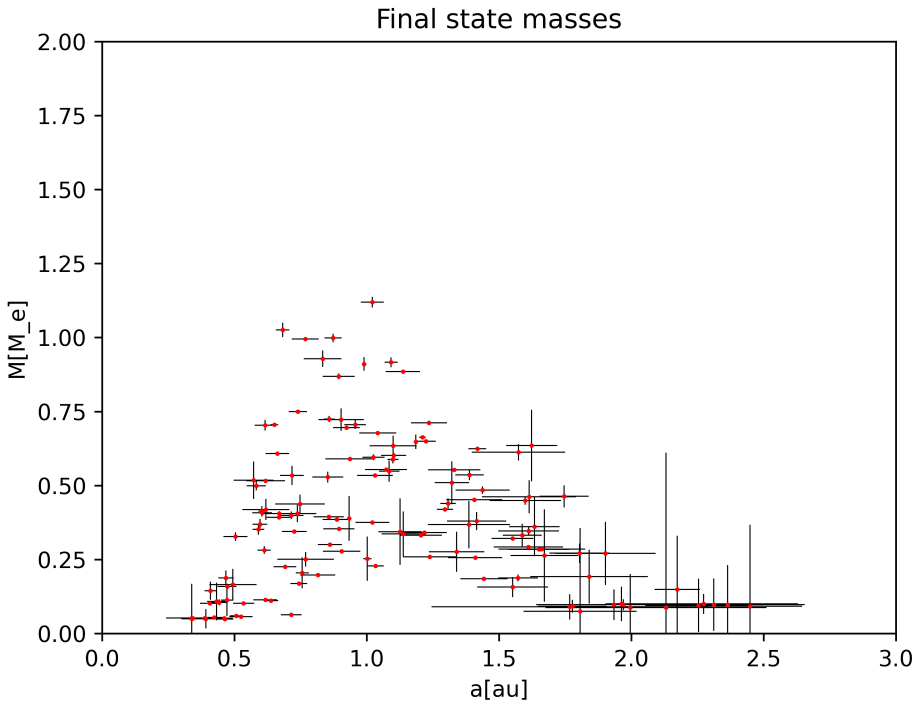

Figure 5.17: All final state planets' masses and semimajor axes. The eccentricities are generally higher than in the previous simulation with damping and forcing to 0.04 and similarly no low-mass planets (less than $0.25 M_{\mathrm{E}}$) occur in the middle (around 1 au).

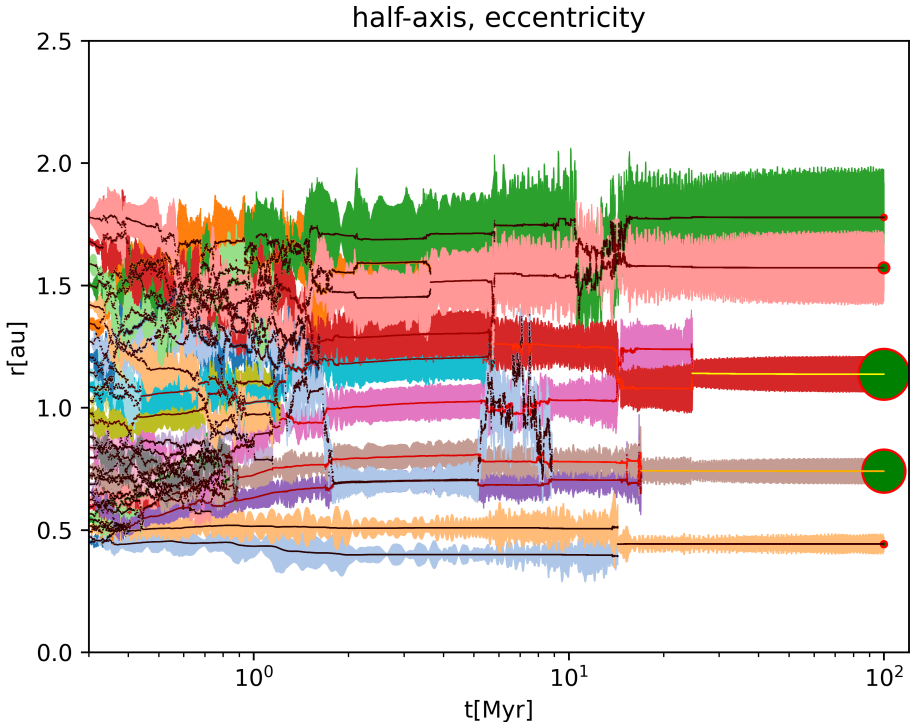

Figure 5.18: The run 25 of statistics – The latest instability occured around 25 Myr was local and led to formation of almost Earth's mass planet. System ended with 5 planets of masses 0.11, 0.75, 0.89, 0.19, 0.09 M_{E}, semimajor axes 0.44, 0.74, 1.14, 1.57, 1.78 au. eccentricities 0.07, 0.05, 0.06, 0.05, 0.07 and inclinations 1.4°, 0.25°, 0.2°, 0.4°, 0.7°.

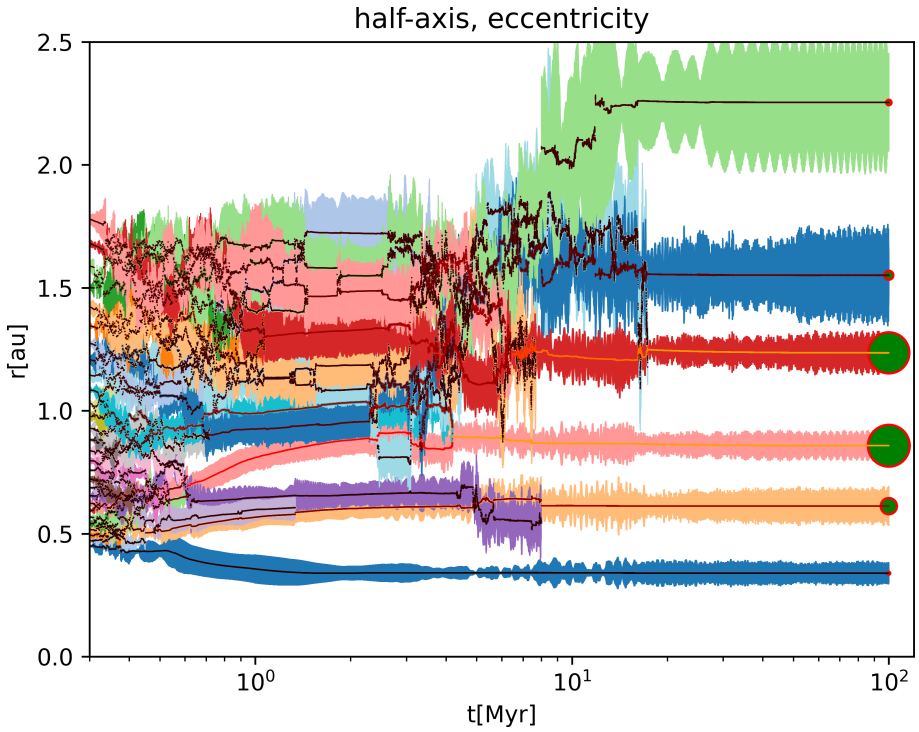

Figure 5.19: The run 24 of statistics – The latest instability occurred between 15 and 20 Myr, when low-mass planet collided with the more distant high-mass planet of almost Venus' size. System ended with 6 planets of masses 0.05, 0.28, 0.72, 0.71,0.16, 0.09 M_{E}, semimajor axes 0.34, 0.61, 0.86, 1.24, 1.55, 2.25 au. eccentricities 0.066, 0.040, 0.024, 0.055, 0.087, 0.089 and inclinations 3.6°, 1.2°, 0.7°, 0.3°, 1.2°, 2.3°.

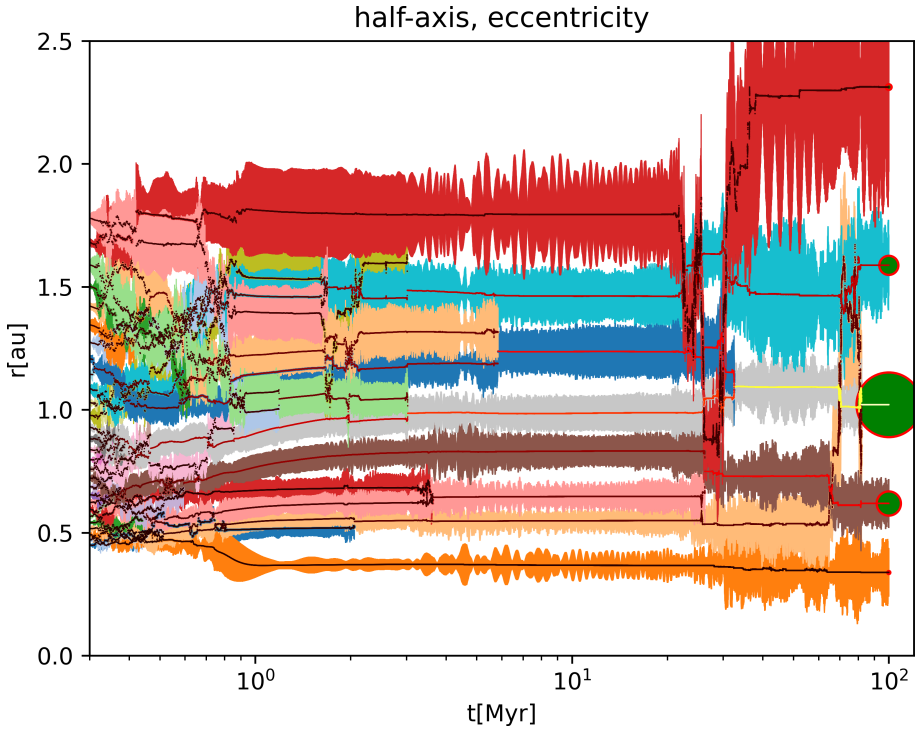

Figure 5.20: The run 18 of statistics – Instabilities and collisions occurred even at around 80 Myr. System ended with 5 planets of masses 0.05, 0.42, 1.12, 0.33, 0.10 M_{E}, semimajor axes 0.34, 0.62, 1.02, 1.59, 2.31 au. eccentricities 0.28, 0.14, 0.04, 0.05 0.15 and inclinations 19.8°, 3.3°, 1.0°, 1.4°, 2.2°.

Conclusions

In this work, we created a global model of early planetary systems and their formation from Mercury- to Mars-sized protoplanets. It combines a 1-dimensional hydrodynamical model of the protoplanetary disk (Suzuki et al. (2016)) with an N-body simulation (Duncan et al. (1998)) and uses semi-analytical prescriptions for migration (Paardekooper et al. (2011)). Our aim was to create systems analogous to the Solar system.

We computed models for a set of values of disk parameters and two different wind regimes (strong and weak); the wind was considered the primary mechanism of mass loss, transporting also angular momentum, together with accretion. Suitable values of parameters were $\overline{\alpha_{r\phi}} = 2.4 \cdot 10^{-5}$, the mid-plane turbulent and magnetic viscous parameter (Suzuki et al. (2016)), $C_{\mathrm{W}} = 3 \cdot 10^{-6}$, the wind mass loss parameter, and $\overline{\alpha_{\phi z}} = 3 \cdot 10^{-6}(\Sigma/\Sigma_0)^{-0.66}$, the viscosity in the region of disk atmosphere. If these parameters are varied proportionally by more than half order of magnitude, our model shows either to too rapid dispersal of the disk and negligible migration, or to too slow dispersal causing strong migration and loss of protoplanets by migrating towards the central star.

For that set of parameters we also calculated a statics of multiple runs and studied a dependence on eccentricity damping. Our best result (7 solar system analogues among 25 runs) was obtained when eccentricity forcing and damping was relatively high (up to the value 0.07). In this case, the corotation torque is reduced and the Lindblad torque creates a relatively stable convergent zone, which does not evolve much with time. These conditions seem to be similar to the model of Brož et al. (2021), however, they considered a stationary disk and limited damping of eccentricities (to around 0.02).

Nevertheless, even our two simulations with eccentricity damping to 0.04 both led to 2 analogues in 25. In our model these moderate eccentricities cause shrinking of the convergent zone, however, rapid dispersal of the inner regions of the disk prevents further migration inwards and this creates 'convergent-like zone', which shifts to higher semimajor axes with time. In these simulations, an interesting mechanism was observed, where a high-mass planet is created in the outer part of the terrestrial zone, migrates inwards and collides with protoplanets whose orbits it crosses. This can led to formation of two high-mass planets close to each other (even closer than Venus and the Earth). The frequent problem in our simulation was too massive Mercury but we started from protoplanets of Mercury too Mars mass and in order to reconstruct Mercury more protoplanets of lower mass could be convenient.

The planetary migrations seems to create mass distribution with more massive planets in the center but in our simulations it was not enough to create as massive planets as the Earth and not enough to reduce by collisions the count of the planets to be comparable to the solar system. Another important mechanism are late global instabilities, occurring after dispersal of the disk (at around 10 Myr). These help to reduce the count of planets, to create massive planets comparable to the Earth or Venus, and also often leaves a low mass planet comparable to Mars on the outer edge of the terrestrial zone. A possible weak point is that it often does not allow two massive planets to be close to each other (0.2-0.3 au) and that often involves interactions of low-mass planets on the inner edge, which eventually leads to formation of a planet more massive than Mercury.

If we compare our distributions of planets in terms of the semimajor axis vs mass, they are similar to distributions by Woo et al. (2024), who studied a completely different scenario — a formation of planets from a narrow ring of planetesimals, influenced by a giant-planet instability. they considered gas drag and simplified migration formulas from Tanaka et al. (2002). In our model, late instabilities occur often spontaneously, without the necessity of giant planet influence. In both models, no low-mass planets (less than $0.2\,M_{\mathrm{E}}$) occur in the middle of the terrestrial zone (around 1 au); they have a tendency to be on the edges.

Evolution of planetary systems seems to be really sensitive to mechanisms driving damping and/or excitation of the eccentricity. Excitation of the eccentricity is often induced by the thermal force (Masset (2017)). At the same time, it changes the migration rate and could possibly extend convergent zones, which were often small (or even nonexistent) for planets with moderate eccentricities (0.02 to 0.04). Consequently, this one of the most promising mechanism how to create Solar system analogues.

Additional mechanism may be also at play, for example, pebble accretion (Lambrechts & Johansen (2012)), pebble torque (Benítez-Llambay & Pessah (2018)), unstable disk fluctuations (Chambers (2024)), excitation of inclinations (Eklund & Masset (2017), Chrenko et al. (2018)), or migration from different radii (Brož et al. (2021); Clement et al. (2021)). All of them are worth to study in the future.

Bibliography

André, P., Di Francesco, J., Ward-Thompson, D., et al. 2014, in Protostars and Planets VI, ed. H. Beuther, R. S. Klessen, C. P. Dullemond, & T. Henning, 27–51

Andrews, S. M., Huang, J., Pérez, L. M., et al. 2018, Astrophys. J. Lett., 869, L41

Avenhaus, H., Quanz, S. P., Garufi, A., et al. 2018, Astrophys. J., 863, 44

Balbus, S. A. & Hawley, J. F. 1991, Astrophys. J., 376, 214

Bell, K. R. & Lin, D. N. C. 1994, Astrophys. J., 427, 987

Benítez-Llambay, P. & Masset, F. S. 2016, Astrophys. J. Suppl., 223, 11

Benítez-Llambay, P. & Pessah, M. E. 2018, Astrophys. J. Lett., 855, L28

Benítez-Llambay, P., Masset, F., Koenigsberger, G., & Szulágyi, J. 2015, Nature, 520, 63

Bitsch, B., Crida, A., Morbidelli, A., Kley, W., & Dobbs-Dixon, I. 2013, Astron. Astrophys., 549, A124

Bitsch, B., Johansen, A., Lambrechts, M., & Morbidelli, A. 2015, Astron. Astrophys., 575, A28

Brož, M., Chrenko, O., Nesvorný, D., & Dauphas, N. 2021, Nature Astronomy, 5, 898

Chambers, J. 2024, Astrophys. J., 966, 40

Chrenko, O., Brož, M., & Lambrechts, M. 2017, Astron. Astrophys., 606, A114

Chrenko, O., Brož, M., & Nesvorný, D. 2018, Astrophys. J., 868, 145

Clement, M. S., Raymond, S. N., & Chambers, J. E. 2021, Astrophys. J. Lett., 923, L16

Coleman, G. A. L. & Nelson, R. P. 2014, Mon. Not. R. Ast. Soc., 445, 479

Cornejo, S., Masset, F. S., Chametla, R. O., & Fromenteau, S. 2023, Mon. Not. R. Ast. Soc., 522, 678

Cresswell, P. & Nelson, R. P. 2008, Astron. Astrophys., 482, 677

Debras, F. & Chabrier, G. 2019, Astrophys. J., 872, 100

Drażkowska, J., Bitsch, B., Lambrechts, M., et al. 2022, arXiv e-prints, arXiv:2203.09759

Duncan, M. J., Levison, H. F., & Lee, M. H. 1998, Astron. J., 116, 2067

Durante, D., Parisi, M., Serra, D., et al. 2020, Geophys. Res. Lett., 47, e86572

Eklund, H. & Masset, F. S. 2017, Mon. Not. R. Ast. Soc., 469, 206

Fendyke, S. M. & Nelson, R. P. 2014, Mon. Not. R. Ast. Soc., 437, 96

Guillot, T. 1999, Planet. Space Sci., 47, 1183

Gysembergh, V., J. Williams, P., & Zingg, E. 2022, Journal for the History of Astronomy, 53, 383

Hayashi, C. 1981, Progress of Theoretical Physics Supplement, 70, 35

Izidoro, A., Ogihara, M., Raymond, S. N., et al. 2017, Mon. Not. R. Ast. Soc., 470, 1750

Jeans, J. H. 1902, Philosophical Transactions of the Royal Society of London Series A, 199, 1

Kant, I. 1755, Allgemeine Naturgeschichte und Theorie des Himmels

Lainey, V., Jacobson, R. A., Tajeddine, R., et al. 2017, Icarus, 281, 286

Lambrechts, M. & Johansen, A. 2012, Astron. Astrophys., 544, A32

Lambrechts, M. & Johansen, A. 2014, Astron. Astrophys., 572, A107

Laplace, P. S. d. 1796, Exposition du système du monde

Lega, E., Crida, A., Bitsch, B., & Morbidelli, A. 2014, Mon. Not. R. Ast. Soc., 440, 683

Masset, F. S. 2001, Astrophys. J., 558, 453

Masset, F. S. 2017, Mon. Not. R. Ast. Soc., 472, 4204

Mestel, L. 1968, Mon. Not. R. Ast. Soc., 138, 359

Oort, J. H. 1940, Astrophys. J., 91, 273

Paardekooper, S. J., Baruteau, C., Crida, A., & Kley, W. 2010, Mon. Not. R. Ast. Soc., 401, 1950

Paardekooper, S. J., Baruteau, C., & Kley, W. 2011, Mon. Not. R. Ast. Soc., 410, 293

Paardekooper, S. J. & Papaloizou, J. C. B. 2008, Astron. Astrophys., 485, 877

Paardekooper, S. J. & Papaloizou, J. C. B. 2009, Mon. Not. R. Ast. Soc., 394, 2297

Pierens, A. & Raymond, S. N. 2016, Mon. Not. R. Ast. Soc., 462, 4130

Raymond, S. N. 2024, arXiv e-prints, arXiv:2404.14982

Raymond, S. N. & Izidoro, A. 2017, Icarus, 297, 134

Shakura, N. I. & Sunyaev, R. A. 1973, Astron. Astrophys., 24, 337

Stix, M. 2002, The Sun: An introduction

Suzuki, T. K., Ogihara, M., Morbidelli, A., Crida, A., & Guillot, T. 2016, Astron. Astrophys., 596, A74

Tanaka, H., Takeuchi, T., & Ward, W. R. 2002, Astrophys. J., 565, 1257

Tanaka, H. & Ward, W. R. 2004, Astrophys. J., 602, 388

Toomer, G. J. 1984, Ptolemy's Almagest

Vázquez-Semadeni, E., Palau, A., Ballesteros-Paredes, J., Gómez, G. C., & Zamora-Avilés, M. 2019, Mon. Not. R. Ast. Soc., 490, 3061

Ward, W. R. 1991, in Lunar and Planetary Science Conference, Vol. 22, Lunar and Planetary Science Conference, 1463

Woo, J. M. Y., Nesvorný, D., Scora, J., & Morbidelli, A. 2024, Icarus, 417, 116109

Zhu, Z., Hartmann, L., Nelson, R. P., & Gammie, C. F. 2012, Astrophys. J., 746, 110